Laser Sources and Nonlinear Optics Based on Self-Assembled Quantum Dots

Alessio Tierno

Department of Physics and SUPA

University of Strathclyde

A thesis presented in the fulfilment of the requirement for the degree of

Doctor of Philosophy

2010

This thesis is the result of the author's original research. It has been composed by the author and has not been previously submitted for examination which has lead to the award of a degree.

The copyright of this thesis belongs to the author under the terms of the United Kingdom Copyright Acts as qualified by University of Strathclyde Regulation 3.50. Due acknowledgement must always be made of the use of any material contained in, or derived from, this thesis.

Signed: Date:

to my parents

Acknowledgements

Moving abroad to start a PhD in Physics has been a challenging and rewarding experience of my career in Physics. Challenging for all the differences between my previous work in physics and the new one and rewarding for the way all this has been affronted.

Dr. T. Ackemann give me the opportunity to work with him and I would like to acknowledgment first him for all the physics I have learned during this period and his careful and passionate guidance through all the step of my PhD.

Prof. M. Brambilla and Dr. T. Maggipinto help me in the theoretical part of my work sharing their knowledgment on numerical simulation. Thank you.

Dr. R. Kuszelewicz and Dr. S. Barbay give me the opportunity to work with them for a period of my thesis and it has been a very good experience to learn new topics and methodology of work. Thanks.

Most of cavity designs the need for complex mounts was essential. Without the technical expertise and design assistance of both Mr Ewan MacLagan and Mr Robert Wylie this would not have been possible.

A big thanks to Dr. Richard Martin for the help on computer programming.

A big thanks go to the fantastic team who I was part at Strathclyde: the photonics group. First of all I want to thanks N. Radwell for his clever and "smooth" way to help me on programming. Without any particular order I want to thanks all the previous and present members of the group: Matt, Griff, Wei, Kenneth, Stephanie, Aline,

Christopher, Yoann, Kyle, Yann, Pradeep, Mateuz, Umakanth and Aser.

During my stay in Glasgow I have the opportunity to meet a lot of people that made my stay remarkable.

A big thanks for their lovely presence and wonderful moment spent together go to Enrica P. and Giuseppe M.

Then I want to thanks the following people: Maria C., Susanna, Paolo 'er cecca', Daniele, Louis, Iorgo, Marjon, Lito, Maria F., Sam, Efrain, Cohrina, M. Pia, Fabiola and Basia.

Strathclyde Harries made my running experience very enjoyable and overall i want to acknowledgment the wonderful coach: A. M. Hughes.

Even wile so far away, my family and my brothers have played during these year a central role in always supporting me and for giving all the warmth that only parents can give.

Last but not least i want to give a big thanks to my friend in Italy that were so keen to visit me in Glasgow and also always up to meet when I was coming to Italy: Domenico, Gaetano, Luigi, Giangaetano, Piercarmine and Luigi I, S. Avino and Maria P.

Laser Sources and Nonlinear Optics Based on Self-Assembled Quantum Dots

Alessio Tierno

University of Strathclyde

Abstract

This thesis describes an extensive study on the optical properties of self-assembled quantum dots in lasers, amplifiers and passive devices.

Results on how to improve the coherence of broad area quantum dot laser diodes are reported as well spectroscopic applications enabled by tunable sources based on quantum dot material.

A new type of instability has been disclosed for some devices. The scenario is investigated in detail. The results led to the conclusion that pulsations in MHz range found can be interpreted as opto-thermal ones similar to that reported for quantum well lasers. The mechanism driving these pulsations is found to be changes in waveguiding properties due to thermal lens.

A theoretical analysis is developed to study the nonlinear optical response of self-assembled QD to cw driving via numerical simulations of a spatially resolved rate equation model. The saturation behavior is shown to follow a behavior in between the one for a dominantly homogeneously and inhomogeneously broadened medium. Self-lensing is also investigated. The minimum focal length, predicted by the numerical analysis, is of ± 1.7 mm for an input beam with 15 μm radius at a detuning of 1.1 inhomogeneous linewidths from gain center.

Then studies on the interaction strength between lasers and self-assembled quantum dots are reported. Saturation of gain and absorption is found for the first time with continuous wave driving in room temperature quantum dots and the correspective value are analyzed.

Contents

List of Figures

Chapter 1

Introduction

In this chapter, the background is introduced. This includes a brief introduction to the development of quantum dots and quantum dot lasers. Advantages and disadvantages of the latter are discussed as well as applications based on quantum dot materials. The organization of this thesis is then given. It contains the relevant results of each chapter.

1.1   Semiconductor laser

Laser emission was demonstrated in a semiconductor p-n junction for the first time in 1962 [1]. Nowadays semiconductor lasers are the type of lasers that are most commonly found outside scientific applications and research. They have proven to be efficient, low cost, small, and reliable sources of laser light, that are used in optical disc players (CD, DVD, Blue-ray), in optical data communication (fast Internet connections over fiber optic cables), for medical applications, and so on.

The semiconductor laser has several advantages over other light sources and lasers: it is highly efficient, the structure of the standard semiconductor laser allows it to be as small as a few micrometers; this type of laser is known to be highly reliable; only a small current source is necessary for the operation; and due to the boom of the microchip industry the growth and processing of semiconductor materials has become a standard technology that allows the production

of hundreds of semiconductor lasers on one wafer, making them comparatively cost-effective.

For a semiconductor diode the main component is the p-n junction, which is a combination of two semiconductor materials: acceptors (atoms providing holes, i.e. missing electrons, with increased mobility) are inserted into the p-doped material, donors (atoms providing electrons with increased mobility) into the n-doped material. Note that the doped materials are still electrically neutral. The electrons are at first found in the valence band. If voltage of the correct polarity is applied they are raised into the conduction band, leaving positively charged holes behind. Both can then move freely through the semiconductor. The p-n junction is responsible for the diode function, because it serves as a conductor when voltage is applied in forward-bias direction and as an insulator for reverse-bias direction.

As stated above the first working semiconductor laser consisted of nothing more than a p-n junction. At the junction itself the free electrons and holes recombine under the emission of photons when the voltage is applied in forward-bias direction. The recombination energy is of the order of the band gap of the semiconductor material. The p-n junction then serves as active medium of the laser. Due to the diode function of the p-n junction semiconductor lasers are also called laser diodes. A simple p-n junction does not form a very efficient laser. A more efficient design was found to be the double heterostructure [2]. For this type of structure two different semiconductor materials with different band gaps are combined. They form three layers on top of each other. The outer layers consist of the material with the larger band gap, the central area of the other semiconductor. The outer layers are p-, respectively n-doped, the center is undoped. This results in a so-called p-i-n structure. At the points where the materials meet energy discontinuities are formed which confine the free carriers to the central layer. Thus a two-dimensional potential well for the carriers is formed and the recombination only takes place in this layer. If the thickness of the central layer is of the order of the de Broglie wavelength of the carriers the energy states available for the carriers become discrete [3]. Such thin layers are called quantum wells. In modern semiconductor laser designs quantum wells are often used as active medium, because the reduction of the density of states

results in higher quantum efficiency (conversion efficiency of carriers to photons) and lower laser thresholds.

A typical double heterostructure laser diode design is shown in Fig. 1.1. The electrical voltage is applied to top and bottom of the structure. The black area in the center represents the active region. The left and right ends of the flat structure are polished and due to the index step from semiconductor to air they have a reflectivity of about 30%.
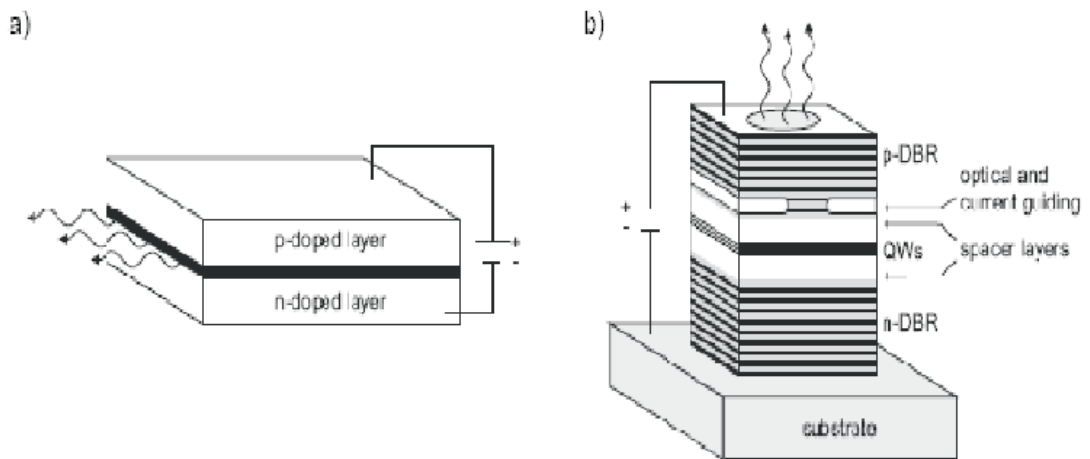
Figure 1.1: (a) Schematic drawing of an edge-emitting semiconductor laser (b) and a vertical- cavity surface-emitting laser.

Thus they serve as resonator mirrors. The wafer, on which the semiconductor materials are grown as thin layers, is cut into rectangles, typically between several hundred micrometers and some millimeters in size. Due to the thinness of the active layer the beam is elliptic and highly divergent in the vertical direction. The selection of the semiconductor materials for the active region (commonly combinations of elements from groups III and V, e.g. AlGaAs, InGaAs, GaN, GaAsP) and their relative concentration selects the emission wavelength of the diode. If the active medium consists of quantum wells the thickness of these also affects the wavelength.

The threshold gain (g_{th}) of a semiconductor laser is given by

$$g_{th} = \frac{1}{\Gamma}\left[\alpha_i + \frac{1}{L}\ln\left(\frac{1}{R}\right)\right] \qquad (1.1)$$

where Γ is the optical confinement factor, which represents the fractional overlap between the optical mode and the gain material; α_i is the internal loss of the structure due to photon scattering within the cavity and any absorption that does not return electrons and holes to the lasing transition; L is the cavity length and R is the reflectivity of the facets.

1.1.1 Low dimensional semiconductors

It is possible to increase the kinetic energy of a particle in a direction via confinement of carrier motion along that direction by an amount inversely proportional to the length scale of the confinement. When this energy becomes similar to the carrier thermal energy ($= 1/2k_b\text{T}$ per degree of freedom), the effects of quantum confinement can be observed. Typical values of electron effective mass and working temperatures reveal that quantum confinement effects are observed when the carriers are restricted to regions of a few nanometers. Semiconductor heterostructure that contain a few nanometers of a narrow bandgap (Eg) semiconductor placed within a wider bandgap semiconductor provide ideal means of investigating such effects.

The advent of epitaxial growth techniques as Molecular Beam Epitaxy (MBE) [4] has opened a way to realize thin films of material required for these studies. Also, the quantum confinement results in a strong modification to the electronic density of states (DOS). The density of states, defined as the number of available electronics states per unit volume per unit energy at an energy E, control the electronic and optical performance of a device. The DOS can be modified by restricting the carrier motion in additional directions. Systems with confinement in one, two and three directions are referred to as quantum wells, wires and dots respectively. The evolution of the DOS is shown schematically in Fig. 1.2. As the dimensionality of the structure reduces, the DOS continuum in the bulk material breaks down in to sub-bands, for quantum well (QW) and quantum wire structures.
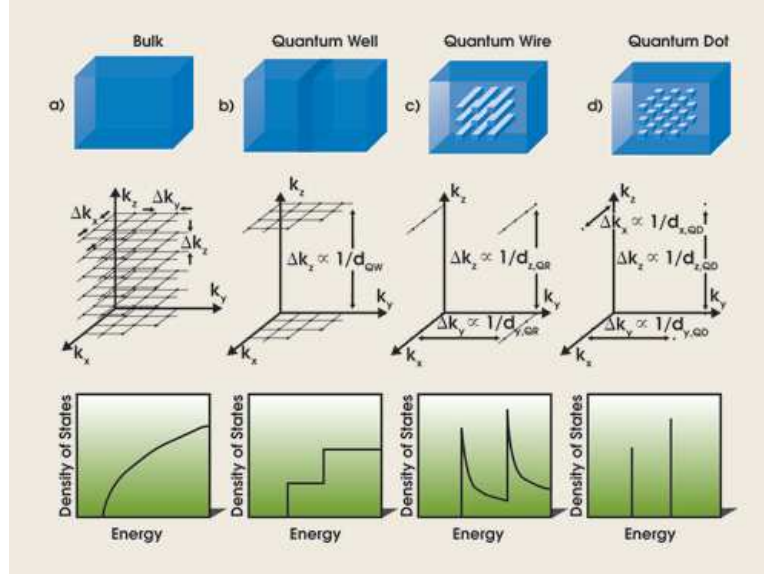
Figure 1.2: Evolution of the density of electronic states (DOS) as the dimensionality of the confinement (system) is increased (reduced). In 2D and 1D systems, the DOS breaks down into sub-bands. Free carrier motion is still possible in the unconfined directions. In a quantum dot, discrete electronic states are formed with no free carrier motion.

Since the onset of the first sub-band in a QW occurs at a higher energy than the bulk Eg, injected carriers are not wasted filling up lower energy states in order to reach the required DOS for lasing to occur. Therefore the threshold gain in QW devices is able to be obtained at a lower carrier injection level than in bulk, resulting in reduced threshold current densities.

In addition, as the dimensionality is decreased, the relative DOS at higher energies decreases with respect to that at the sub-band edge. Hence the number of available states into which carriers can be thermally excited decreases and this should result in a greater thermal stability for laser devices.

Furthermore, the enhancement of the DOS at the band edge in structures of reduced dimensionality is predicted to provide an increase in the available differential gain. Since the modulation bandwidth of a device is proportional to the differential gain, devices containing low dimensional active regions are therefore very attractive candidates for optical communication applications operating at high modulation speeds.

The ultimate case of quantum confinement corresponds to the formation of a quantum dot (QD) [5; 6]. Here the carrier motion is confined in all three dimensions such that the sub-band structure of QWs and quantum wires is lost and an atomic-like series of discrete states is produced. Before their physical realization, it was predicted [7] that if an ensemble of identical QDs could be incorporated into the active region of a laser diode, the temperature dependence of the threshold current density (I_{th}) would be eliminated. This insight relies on the QD states being well described by a delta function-like DOS, with separations that significantly exceed the thermal energy. In principle, an infinitely narrow DOS results in all of the injected carriers recombining with an identical transition energy. The absence of a sub-band continuum, into which carriers may be excited as the temperature increases, eliminates higher energy parasitic recombination and decreases the transparency current density at non-zero temperature. In 1982, Arakawa and Sakaki [8] produced the first experimental evidence that 3D carrier confinement, provided in this case by a magnetic field applied perpendicular to a QW laser, could reduce the temperature sensitivity of I_{th}. Furthermore, the complete localization of the excitons within the QDs should, in theory, reduce or eliminate their transfer to non-radiative centers in the surrounding matrix material, thereby reducing the non-radiative component of I_{th}.

The threshold current, $I_{th}(T)$ is given by the relation:

$$I_{th}(T) = I_{th}(T_{ref})[\exp(T - T_{ref})/(T_0)] \qquad (1.2)$$

where T is the active region temperature, T_{ref} is the reference temperature, and T_0 is the characteristic temperature, which is itself a function of temperature and device length. In QDL T_0 can be high, because one can effectively decouple electron-phonon interaction by increasing the intersubband separation. This leads to undiminished room-temperature performance without external thermal stabilization. Also study of the T_0 of quantum-dot (QD) laser diodes shows that inhomogeneous broadening and p-doping influence the QD lasers temperature dependence of threshold [9].

1.1.2 Self-assembled growth

The idea of producing semiconductor structures to provide three dimensional confinement was initially thought to require lithography and etching of a planar structure. This was until the self-assembly of small crystal islands was found: InAs has a 7% strain mismatch with GaAs which means that $In_xGa_{1-x}As$ alloys grown on a GaAs substrate accumulate strain as they are deposited. Under the correct growth conditions, InAs initially deposited on the growth surface will form a compressively strained pseudomorphic wetting layer (WL). Further deposition of InAs then increases the strain mismatch until coherent three dimensional islands spontaneously form when the cost in energy for deforming the surface becomes lower than continuing to form the next planar layer. This is called the Stranski-Krastanow [10; 11] growth mode.

Importantly, once the islands have been grown they must then be buried into the host crystal; partly so that the islands can be integrated into bulk-crystal heterostructure devices and also to isolate them from the deleterious effects of surface states. Both the formation and burying (or capping) processes must be controlled so as to keep the islands coherent with the host crystal and to control the size, composition and strain state of the QD. When the island material grown in the Stranski-Krastanow mode has a lower energy gap that its host matrix, a potential well in all three spatial dimensions can be created in the band structure. These islands are then called quantum dots (QDs) and can confine electrons and/or holes, leading to localized states with well defined energies within the energy gap of the host matrix. The energies of these states are controlled by the size, shape, composition and strain-state of the QD. To decrease the energy of the lowest state (the ground-state or GS) the QD must either be larger in size, have a higher In composition or be under less compressive-strain from the host crystal.

The resultant QDs are roughly lens or pyramidal-shaped and have sizes on the order of a 20-30 nm per side square base and 5-10 nm height [12]. The shape and composition of self-assembled quantum dots are properties quite demanding to determine and often only available by indirect means. Precise knowledge of these

parameters, [13; 14; 15; 16] on which optical and electrical properties depend, is of major interest.

1.1.3 Inhomogeneous broadening

The self-assembly process discussed before is driven by random fluctuations during growth and therefore unavoidably causes the positions of the QDs to be random and gives a statistical spread in the size-distribution. The random positioning of the QDs is not important for laser devices, as the dimensions of the device enclose enough QDs as to always be dealing with a representative ensemble. However the latter effect causes inhomogeneous broadening (IB) of the ensemble's optical properties.
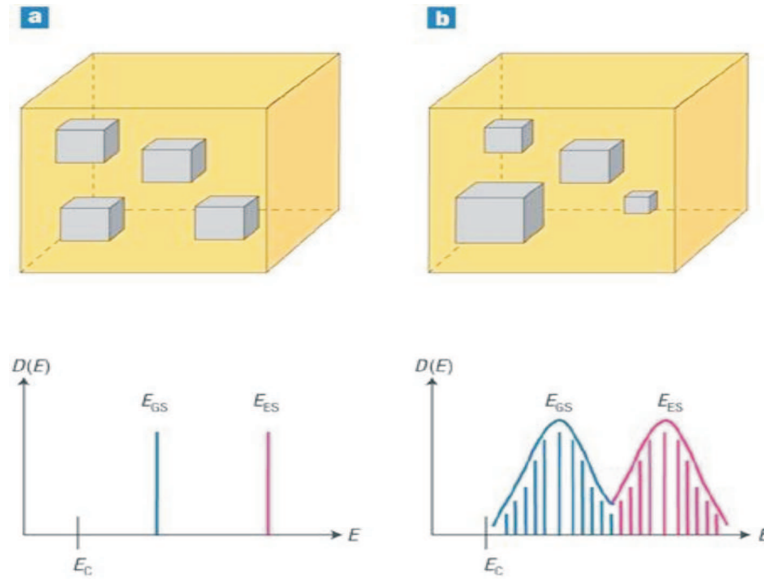
Figure 1.3: (a) A schematic of an ideal QD system and, (b), a real QD system, where inhomogeneous broadening is illustrated. (EGS: ground-state energy; EES: excited-state energy; EC: the bottom of the conduction band).

Because of the way QDs are grown, there is a Gaussian distribution of sizes with a corresponding Gaussian distribution of emission frequencies, Fig. 1.3. These effects lead to inhomogeneous broadening. At cryogenic temperatures, IB is several orders of magnitude wider than the transition linewidth [17; 18].

Assuming that each QD is isolated from the rest, only QDs whose peak emission energy is separated from a laser mode by less than their homogeneous linewidth (in the region of 5-10 meV at room-temperature and increases for higher carrier densities [19]) are able to contribute to its oscillation having an inhomogeneous line-width that is greater than the homogeneous broadening will limit the laser's efficiency. Therefore growth recipes that result in lower inhomogeneous broadening are desirable.

For quantum dots, typical value of homogeneous broadening of few μeVs are normally reported in the literature for low temperature [20].

Increasing the temperature the value of homogeneous broadening increases. At room temperature the rate between homogeneous and inhomogeneous broadening is around 4, typical value of homogeneous broadening is on the order of 10-20 meV [21; 22] and inhomogeneous broadening around 40-60 meV.

1.1.4 Linewidth enhancement factor for quantum dot

Essentially due to noise from spontaneous emission into the resonator modes, a free-running (not stabilized) single-frequency laser has a certain finite linewidth. For simple cases, this fundamental limit for the linewidth was calculated by Schawlow and Townes even before the first laser was experimentally demonstrated. Whereas this limit was later shown to be closely approached by a number of solid-state lasers, significantly higher linewidth values were measured for semiconductor lasers (laser diodes) even when the influence of technical noise was very low. It was then later found by [23] that the increased linewidths result from a coupling between intensity and phase noise, caused by a dependence of the refractive index on the carrier density in the semiconductor. Henry introduced the linewidth enhancement factor or α-factor to quantify this amplitude-phase coupling mechanism; essentially, α is a proportionality factor relating phase changes to changes of the amplitude gain. He then found that the linewidth should be increased by a factor of $(1 + \alpha^2)$, which turned out to be in reasonable agreement with experimental data.

Apart from increasing the laser linewidth in continuous-wave operation, a non-zero linewidth enhancement factor also causes a chirp when e.g. a laser is

power modulated, or when an intense optical pulse passes an amplifier which it saturates. Curiously, the amplitude-phase coupling related to the linewidth enhancement factor can under certain circumstances (with frequency-dependent loss) be used to reduce the linewidth even below the Schawlow-Townes limit.

This can be understood by taking into account the carriers not only of the quantum dots themselves, but also in the wetting layer. There are also various other subtle effects [24]. In general, the values reported for QD are between $\alpha \approx 1 \div 2$ [25; 26], although zero-factor has been reported [27] and also large value of it are reported in literature [9].

There are different methods for the measurement of the linewidth enhancement factor. Most common are those based on recording the spectrum of Amplified Spontaneous Emission(ASE) for different excitation levels, on measuring amplitude and phase modulation caused by a modulated drive current, pump-probe measurements, and linewidth measurements. We consider the linewidth enhancement factor defined as [28]

$$\alpha \approx -\frac{2\pi}{\lambda} \frac{dn/dN}{dg/dN} \tag{1.3}$$

where n is the refractive index and g is the gain per unit length and N is the carrier density.

1.2 Quantum Dot Lasers

A quantum dot laser (QDL) is a semiconductor laser that uses quantum dots as the active laser medium. Quantum dot lasers acquired more importance after significant progress in nanostructure growth in the 1990 such as the self-assembling growth technique for InAs QDs. The first demonstration of a quantum dot laser with low threshold density was reported in 1994 [29]. Room temperature QD edge-emitting lasers, were demonstrated later on [30; 31; 32] and now match or surpass quantum-well performance.

In the following paragraphs a review of advantages and disadvantages of QDL laser is presented.

1.2.1 Advantages of quantum dot lasers

The advantages in using quantum dot lasers compared to quantum well lasers are several. A quantum dot laser emits at wavelengths determined by the energy levels of the dots, rather than the band gap energy. Thus, they offer the possibility of improved device performance and increased flexibility to adjust the wavelength. They have the maximum material and differential gain, at least 2-3 orders higher than QW lasers [33].

Quantum-dot lasers (QDL) are expected to show a broader modulation bandwidth [34], higher temperature stability and lower power consumption than quantum-well counterparts, primarily due to the discrete energy states of electrons and holes under three-dimensional quantum confinement by quantum dots [8; 35].

They show superior temperature stability of the threshold current [36]. QD lasers suppress the diffusion of non-equilibrium carriers, resulting in reduced leakage from the active region. Quantum-dot lasers operable at high pulse-repetition rates are capable of reaching pulse energies that will allow modifying living cells, e.g., making accurately controlled incisions in cell structures, while minimizing the attendant effects on cellular environments.

Also forming high-density indium-arsenide (InAs) quantum dots on the surface of a gallium-arsenide (GaAs) substrate, improves the laser's operation speed and enabling a significant improvement over previous technologies. This new technology is expected to be employed next-generation high-speed data communications at 100 Gbps [37].

1.2.2 Limiting factors in quantum dot laser

Initial calculations of the expected performance of QD lasers assumed idealized dots containing only one electron and one hole level and that all QDs in the laser were identical. Real QDs contain multiple states, there are states external to the QDs, there may be defect related and Auger non-radiative recombination and the dots within an ensemble exhibit a significant distribution in size, shape and composition. Hence an important question is how far from the ideal behavior a QD laser will deviate.

In order for QD lasers to compete with QW lasers, two major issues have to be addressed: a large array of QDs has to be used because their active volume is very small. An array of QDs with a narrow size distribution has to be produced to reduce inhomogeneous broadening. Furthermore, that array has to be without defects that degrade the optical emission by providing alternate non radiative defect channels.

An other potential disadvantage of the highly localized nature of the states of QDs is the phonon bottleneck [38; 39; 40]. Due to the fully quantized carrier confinement in a QD, there is no wavevector (k) dispersion in any direction. In higher dimensionality systems, carrier relaxation to the bottom of the respective band can proceed via the emission of a series of single optical phonon, which occurs very efficiently on a time scale of 100 fs per phonon, followed by slower but still efficient acoustic phonon scattering. These processes are able to conserve both energy and momentum. The lack of continuum states within QDs inhibits such a process, it being very unlikely that the spacing between the discrete levels exactly matches the LO phonon energy. Therefore it was predicted that the carriers would remain trapped for several nanosecond in the higher energy states and this mechanism was cited as an intrinsic reason for poor optical efficiency in original studies of QDs.

Although a gain medium containing QDs has the potential to offer simultaneously high differential gain and low transparency current density (J_o), a combination which can provide the lowest (J_{th}) at any cavity length, the full extent of this advantage can never be realized in practice. The material gain (g_{mat}) obtainable from the ground state (GS) transition of a single QD is inversely proportional to the homogeneous broadening of the transition. However the gain produced by a single QD is very small and hence in order to produce a total (g_{mat}) able to overcome the losses of a typical laser cavity a high density array of QDs must be produced.

The self-assembly technique, which was discussed in paragraph 1.1.3, is able to produce a high density ensemble of QDs, with densities as high as $5-10^{10}\text{cm}^{-2}$ possible, but suffers from the fact that there are intrinsic fluctuations in the QD size, shape and composition, which results in an inhomogeneous broadening of the optical transitions (typically of the order of 40-60 meV). This inhomogeneous

broadening smears out the DOS intrinsic to a single QD and is the dominant contribution to the emission linewidth, even in highly uniform ensembles of QDs [41]. In such an in homogeneously broadened system, the peak DOS and therefore the lasing energy, corresponds to the most probable size of QD in the array. For a QD ensemble of fixed in-plane QD density, any inhomogeneous broadening leads to a reduction in the peak DOS, resulting in lower saturated and differential gain. Although careful optimization of the growth conditions may reduce the degree of inhomogeneous broadening it appears difficult to reduce it below 15 meV [42].

The existence and population of excited QD states is also detrimental to device performance. Any population of excited states reflects wasted carriers which results directly in an increased threshold current density. In addition, since the saturated and differential gain is proportional to the degeneracy of the state involved in the lasing, any thermal occupation of these states may result in a switch from GS lasing to ES1 lasing or even the second excited state (ES2) lasing with increasing injection current or temperature. The population of excited states has also been correlated with an increase in the non-radiative current density, due to the greater number of non radiative channels being accessible via these states [43].

Another factor that affects the performance of a QD laser is that, particularly at low temperatures, there may not be a thermal distribution of carriers within the QD ensemble. For example, the transition from a non-thermal to a thermal distribution is believed to cause the widely reported decrease of J_{th} with increasing temperature between 6 K and 200 K, observed in nearly all QD lasers [44].

At low temperatures electrons and holes recombine within the QD into which they are initially captured and hence the whole ensemble contributes to the emission, carriers in different QDs are effectively isolated from each other. As the temperature is raised the thermally induced transfer of carriers from QDs with shallower confinement to more deeply confining QDs is able to narrow the gain spectrum and consequently reduce J_{th}.

The spectral form of the lasing emission is also determined by the carrier distribution within the inhomogeneously broadened QD states, i.e. the temperature. At low temperatures, when carrier transfer between QDs is effectively suppressed, the lasing emission consists of a broad, multimode lasing spectrum [45].

On increasing the injection further above J_{th} additional lasing modes appear. This behavior results because there is no global clamping of the carrier density and QDs that initially are not lasing at threshold are able to continue to increase their carrier density until they reach lasing. At higher temperatures this process is suppressed once thermal distribution within the ensembles is achieved.

Above 200 K, J_{th} is typically observed to increase slowly with temperature until an onset temperature is reached, between 250 and 300 K, above which J_{th} increases relatively rapidly. In general, the temperature at which this onset occurs decreases with increasing threshold gain (increasing cavity loss). It has therefore been suggested that the degradation of J_{th} at high temperature originates mostly from the thermal population of the excited states, since the Fermi level increases with increasing threshold gain.

The predicted advantages of incorporating QDs as the active region in optoelectronic devices and the promising aspects of self-assembled quantum dots have stimulated intense activity. Devices incorporating quantum dots have been demonstrated and some improvements over QW devices have been achieved.

Threshold currents as low as 25 Acm^2 have been reported for QD lasers [46] but the characteristic temperature T_0 are found to vary from 50-100 K.

There is a consensus that the full potential of zero-dimensionality is yet to be realized in real devices due to the broad inhomogeneous line-widths and rather low dot densities ($\sim 10^{10}$ cm^2). In a laser, for example, a sufficient number of dots is required to emit at the operating wavelength to prevent gain saturation. This could in principle be achieved by an improvement in the uniformity of the quantum dot distribution for a narrow emission range, an increase in the dot density or by utilizing multiple stacked QD layers. Alternatively, a micro-cavity structure can be designed to enhance the emission at the desired wavelength whilst suppressing unwanted emission.

1.3   Typical structure

A typical state-of-the art quantum dot layer structure is show in Fig. 1.4. The quantum-dot material, normally used, consists of 10 layers of $In_{(x)}Ga_{(1-x)}As$ on GaAs substrate. This material is grown by molecular beam epitaxy.

Layer Structure Specification

Product:						DO957					

Layer	Material	Group	Repeat	Mole fraction (x)		Thickness	Doping profile		Type	Dopant
				start	finish	(nm)	start	finish		
14	GaAs					200	1e20		P	C
13	Al(x)Ga(1−x)As			0.35	0	20	3e18		P	C
12	Al(x)Ga(1−x)As			0.35		1000	1e18		P	C
11	Al(x)Ga(1−x)As			0.35		500	5e17		P	C
8	GaAs	1	10			33			U/D	None
7	In(x)Ga(1−x)As	1	10	0.15		5			U/D	None
6	InAs	1	10			0.8			U/D	None
5	GaAs					33			U/D	None
4	Al(x)Ga(1−x)As			0.35		500	5e17		N	Si
3	Al(x)Ga(1−x)As			0.35		1000	1e18		N	Si
2	Al(x)Ga(1−x)As			0	0.35	20	3e18		N	Si
1	GaAs					500	3e18		N	Si
0	GaAs substrate					N+ GaAs 3 inch				

Figure 1.4: Layer structure specification

The exact layer composition of typical material is shown in Fig. 1.4.

1.4   Applications of quantum dots

InGaAs quantum dot (QD) lasers are an important material especially because they are filling the gap between 1100 nm and 1300 nm over the InGaAsP, opening new perspectives for a variety of applications, see Fig 1.5. The quest for QD devices with uncooled operation over a large temperature range, high efficiency and temperature stability still continues. An additional advantage offered by InAs/GaAs QDs is the possibility of achieving longer wavelength emission than that possible from strained InGaAs/GaAs Quantum Wells.

It is also, important to notice that the wavelength range covered by their second-harmonic radiation lies in the yellow. Coherent light sources from grating-coupled external cavity lasers are important for laser spectroscopy [47], interferometry [48] and so on. The light sources are also important for optical coherence tomography measurement [49; 50] and in wavelength division multiplexing systems. Quantum dot external cavity can be used for absorption spectroscopy as well.
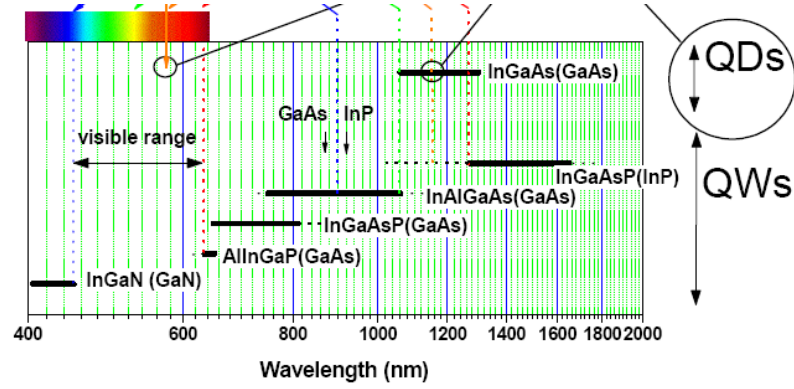
Figure 1.5: Wavelength coverage of laser diodes of different types and materials. QD: quantum dot lasers, QW: quantum well lasers
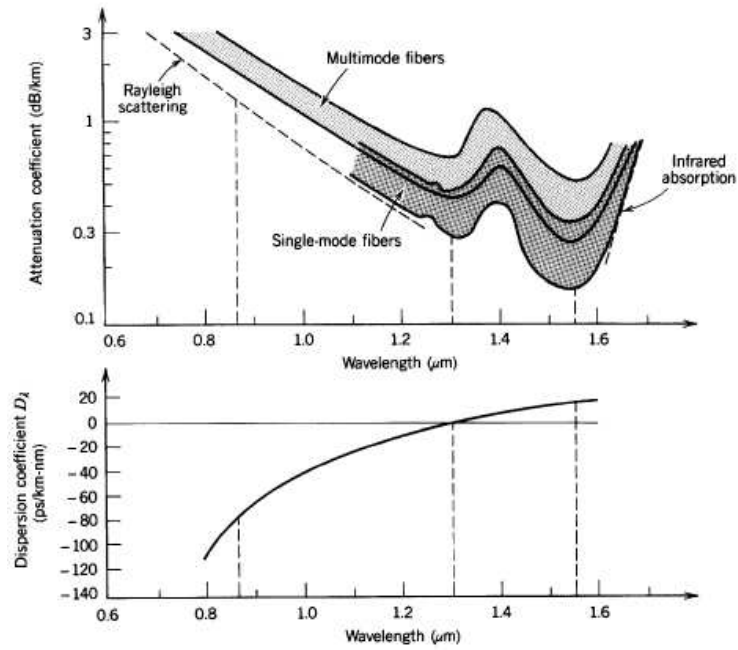
Figure 1.6: Wavelength dependence of the attenuation and material dispersion coefficient of silica-glass fibers, indicating three wavelengths at which fiber-optics communication systems typically operate: 0.87, 1,3 and 1.5 μm.

In 1994 it was shown that emission wavelengths up to 1.3 μm could be attained from InAs/GaAs QDs [51]. At 1.3 μm there is a local minimum in absorption and

zero dispersion in standard silica optical fibers used for high speed data transfer, as shown in Fig. 1.6. A minimum of absorption is also located at 1.55 μm. Devices operating at these wavelengths are currently fabricated on InP substrates to serve both metro and long haul telecommunication applications.

However, there is an increasing demand for the manufacture of devices on GaAs substrates operating over the 1.2-1.6 μm telecoms window.

A 1.3 μm QD laser [8] was realized in 1998 and pulsed operation of a 1.3 μm QD VCSEL has been also demonstrated [52]. It has also been demonstrated that the properties unique to QDs may prove useful for many other applications. The broad inhomogeneous emission line-widths associated with self assembly may be utilized in broadband semiconductor optical amplifiers (SOAs) and in tunable lasers [53]. The polarization insensitivity of QDs may also be an advantage in photodectors [54]. In addition, the discrete electronic structure of QDs may provide a convenient single-photon source desired for quantum computation applications [55].

An individual quantum dot has the capability of trapping individual electrons or holes and it might be possible to exploit this as a memory element with a bit represented by a single electron in a single quantum dot. For this to succeed, it is necessary that the storage time is long enough to be practical.

There is a pressing need in quantum cryptography for a single photon source. Quantum cryptography uses either the phase or the polarization of single photons as the means of communication and can achieve almost totally secure transmission [56]. The basic idea is that the sender rotates his basis randomly, making it impossible for an eavesdropper to detect a photon and accurately to recreate it. For this technology to become viable, a single photon emitter is required. In prototype systems, a highly attenuated laser pulse is used as the source, but this is both inefficient as the majority of pulses are empty, and insecure, as a fraction of the pulses contain two photons. A source consisting of a single quantum dot can in principle overcome these limitations. The advantage of quantum dots over single molecules for these applications is that quantum dots, unlike single molecules, do not suffer from photo-bleaching, although progress has recently been made in the preparation of single molecules by embedding terrylene molecules in a p-terphenyl molecular crystal.

Also the efficiency of solar cells could be increased to more than 60% from the current limit of just 30%, capturing higher-energy sunlight that is normally lost as heat in conventional devices using semiconductor nanocrystals, or quantum dots [57]. This is because in typical devices, photons with energies above the semiconductor's bandgap generate "hot" charge carriers (electrons and holes) that quickly cool to the band edges in a matter of just picoseconds, releasing phonons. If the energy of these hot electrons could be captured before it is converted into wasted heat, solar-to-electric power-conversion efficiencies could be increased to as high as 66%.

1.5 Thesis Outline

This thesis is organized in the following way.

Chapter two introduces how quantum dot lasers can be used as tunable sources. Following a characterization of broad-area laser devices the chapter describes first study on the improvement of the coherence of a broad area laser based on quantum dots [58]. After that the characterization of small area QDL diode is given. The tunable source is used in a spectroscopic setup for photocurrent measurement in low dimensional samples for Terahertz application [59].

Chapter three report study on self-sustained pulsations in the output of an InAs quantum dot laser diode in the MHz range. A novel type of instability is disclosed. The characteristics (shape, range and frequency) are presented for the free running laser and when optical feedback in the Littrow configuration is applied [60; 61; 62]. The frequency resolved optical spectra reveal different envelope shifts between the two cases related to a change of phase-amplitude coupling across the gain maximum in agreement with the expectation for a two level system. The time scale and bifurcation scenario suggest that these are opto-thermal pulsation similar to those reported in quantum well amplifiers [63]. Bistability in the light-current characteristics is observed for wavelengths smaller than the gain peak ($\lambda = 1225$ nm), but it is not present for wavelength above the gain peak and for the free running lasers. The pulses in the beam wings are square-like where the ones in the center have a characteristic initial overshoot. This indicates that initially emission is more concentrated in the center and that

a thermal change in waveguiding properties induces these oscillation. A novel mechanism for opto-thermal pulsations is given [60].

Chapter four is a theoretically investigation and numerical modeling on saturation behavior and self-lensing in self-assembled quantum dot under continuous wave driving (cw) [64]. In this chapter, starting from a previous model [28] we exploit the nonlinear optical response of QD to cw driving via numerical simulations of a spatially resolved rate equation model. Self-lensing is suggested to probe the refractive index nonlinearities and to open a complementary way of characterizing phase-amplitude coupling (α-factor) in QD samples. For conservative assumptions on current samples the minimum focal length is predicted to be ± 1.7 mm for an input beam with 15 μm radius at a detuning of 1.1 inhomogeneous linewidths from gain center.

Chapter five report study on the interaction strength information between laser and self assembled quantum dot, as a function of power in the form of the absorption coefficient and gain. Our analysis is concentrated on continuous wave (cw) beam interacting on quantum dot structure. Several setups have been arranged and relevant result are presented regarding saturation of absorption and gain [65]. Also a possibly nonlinear index shift is discussed in InAs and InAlAs quantum dot experimentally.

A final conclusion of the presented work in this thesis is drawn in Chapter six. Major results are summarized.

Chapter 2

Tunable Source based on Quantum Dots

2.1   Introduction

Lasers and amplifiers based on semiconductor quantum dots (QD) have developed tremendously over the last years [66; 67]. InAs QD not only bridge the gap between highly strained InGaAs quantum well material (reaching about 1100-1200 nm) and the well established InP technology for telecommunication lasers (starting roughly with the O-band at 1260 nm), but extend well into the telecommunication regime thus providing an alternative to InP lasers based on the beneficial GaAs material systems [27; 36; 68; 69; 70].

In this chapter an investigation on coherence improvement, and the application of a tunable source based on quantum dots is reported.

2.2   Temperature behavior of QDL

2.2.1   Background information

For laser performance is important to asset how QDL behave as function of temperature.

Quantum well lasers, based on InGaAs(P)/InP over the wavelength range 1.3-1.6 μm, suffer from poor temperature stability [71] and there is a demand for a new generation of low-threshold, fast, and temperature insensitive semiconductor lasers emitting at 1.3-1.55 μm for optical telecommunication systems.

Quantum dot (QD) lasers appeared as ideal candidates for temperature (T) insensitive operation after Arakawa suggested that their threshold currents would be temperature insensitive, or in other words have an infinite T_0 [8].

In reality QD lasers are not as temperature stable as originally anticipated. Current state-of-the-art 1.3 μm quantum dot lasers reported in the literature shows that even when low threshold current densities can be achieved in quantum dot lasers, it is at the expense of a low T_0. A high T_0 can only be achieved at the expense of high threshold current densities. For that reason it was proposed [72] that p-doping would greatly enhance the properties of 1.3 μm InAs/GaAs quantum dot lasers. Results have been published since then [35; 73; 74; 75] showing that p-doped quantum dot lasers can indeed exhibit temperature insensitive I_{th} but this is usually at the expense of comparatively high threshold current densities. Furthermore, at high temperatures (typically 330 K) the T_0 of p-doped devices drops to values similar to that of undoped devices [35; 73].

In conclusion, temperature insensitive threshold current can be achieved in 1.3 μm InAs/GaAs QD lasers by using p-doping. However this is only possible over a limited temperature range and at the expense of relatively large threshold currents [76].

2.2.2 Spontaneous emission spectra

The spontaneous emission is the dominat process below the laser threshold. Photoluminescence spectroscopy has perhaps been the most extensively used characterization tool for self assembled quantum dots for the ease of the measurement, the information it yields about the extent of quantum confinement and inhomogeneous broadening of the density of states, and its very direct relevance in assessing the use of these structures in QD lasers.

This motivates the study how the diode behave as function of temperature for the spontaneous emission and the lasing operation.

The QDL used is from Innolume GmbH, has a length of L = 1.5 mm and a stripe width of w = 100 μm. The facets are not coated. The layer structure is similar to Fig. 1.4. It contains 10 layer of InAs QD in a GaAs matrix substrate.

The temperature is controlled by a Peltier element. The laser diode is mounted asymmetrically on a 4 mm long C-mount. The QDL can emit in both direction of propagation along the emission axis.
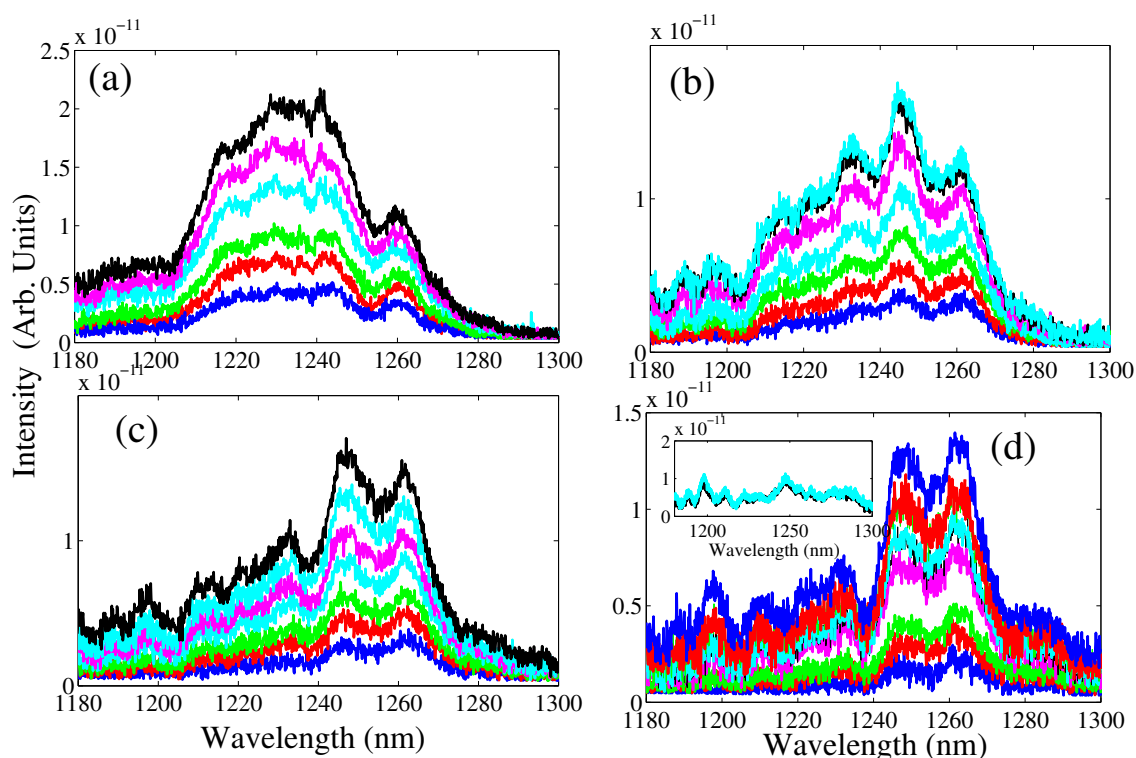
Figure 2.1: Spontaneous emission spectra at: (a) T = 10 °C, (b) T = 24 °C, (c) T = 39 °C, (d) T = 53 °C, inset of (d) T = 73 °C for increasing current.

The spontaneous emission spectrum has been taken, for five different temperature, as function of wavelength for different current level, Fig. 2.1(a-d). The spontaneous emission spectra are broadband and appear peaks more pronounced increasing current. From the same set of temperature there is no shift of the whole photoluminescence spectra increasing the current.

Increasing the temperature a shift toward higher wavelength is evident, Fig. 2.1(a-d). At 10 °C the spontaneous emission is centered around $\lambda = 1240$ nm, Fig. 2.1(a),

to increase up to $\lambda = 1260$ nm at T= 53 °C, Fig. 2.1(d). At even higher temperature, inset of Fig. 2.1(d), no detectable spontaneous emission appears. At higher temperature (T= 53 °C and at T= 73 °C) some spike at low wavelength ($\lambda = 1200$ nm) appear more pronounced. Increasing the temperature the spontaneous emission spectra become more noisy, Fig. 2.1(a-d).

The peaks present in the spontaneous emission spectra are probably the emission mode of the diode but maybe they are also due to the small single mode fiber used for the recording and hence the low light present inside the optical spectrum analyzer.

The area below the curve has been calculated for different temperatures as function of the current, Fig. 2.2. The area is related to the energy hence it is an important information to have. The area has a linear dependence with current, as expected. Increasing the temperature the area of the spontaneous emission spectra becomes smaller.
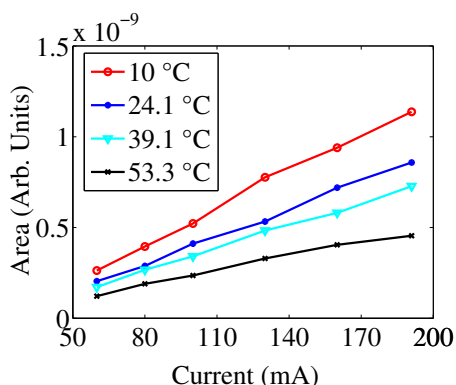
Figure 2.2: Area below the photoluminescence intensity curve as function of the current for different temperatures.

Fig. 2.3 shows, for several temperatures and fixed current, in that case I $= 160$ mA, the spontaneous emission spectra as function of wavelength.

The peak of the spontaneous emission spectra has been isolated, see inset of Fig. 2.3. The inset of Fig. 2.3 shows that from T $= 20$ °C until T $= 40$ °C there is no shift with temperature of the PL. Then there is this an abrupt shift increasing temperature to a wavelength of $\lambda = 1255$ nm. The linear fit of temperature as
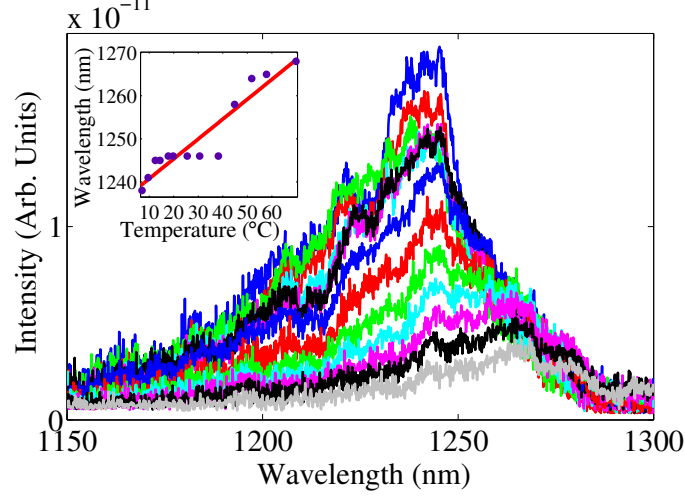
Figure 2.3: Variation of the spectra as function of the temperature for fixed current I= 160 mA , inset linear fit of the variation in wavelength as function of temperature.

function of wavelength shows a shift of 0.5 nm/°C about two times the normal value given for quantum well of 0.2-0.3 nm/°C.

2.2.3 Lasing spectra

Once having analyzed the behavior of the laser below threshold it is important to characterize the lasing emission spectra.

Fig. 2.4(a) gives an indication of the behavior in power, detected with a power meter, as function of current for several temperature. Increasing the temperature we see that the threshold of the laser increases, inset of Fig. 2.4 (b). The minimum threshold is I = 190 mA at T = 7°C and increases to I = 500 mA at T = 57°C. The graph of Fig. 2.4 (b) and the inset show how the threshold current density and threshold varies as function of temperature. From the the graph of Fig. 2.4 is possible to infer the characteristic temperature T_0 of our devices.

The characteristic temperature T_0 is defined by $I_{th} = I_0 \times \exp(T/T_0)$ where T is the temperature and I_0 is the threshold current as T approaches 0 K. From the coefficient of the fit T_0 has been calculated. We have $T_0 = 50 \ K$ in our case in agreement with the previous cited literature on quantum well lasers [40].
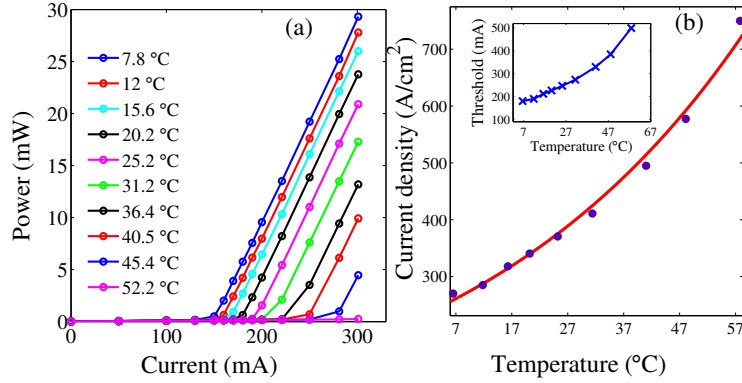
Figure 2.4: a) Power detected as function of current injected for increasing temperature (b) QDL threshold current density as function of the temperature, inset threshold as function of current.
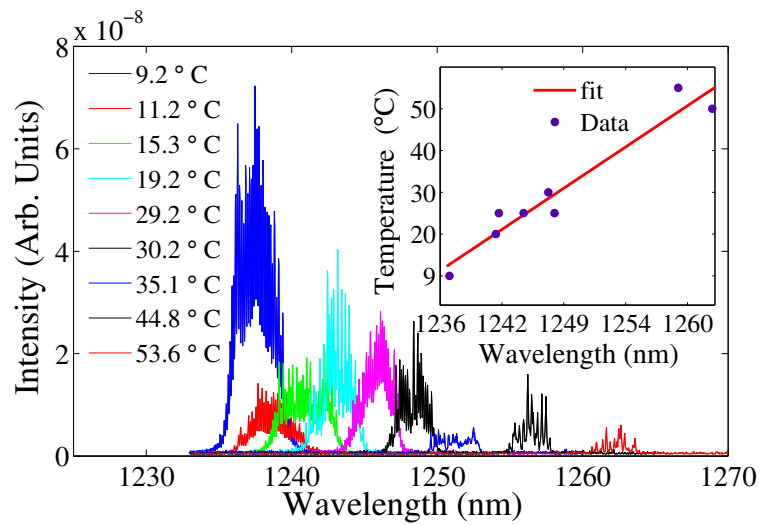
Figure 2.5: Lasing emission spectra as function of wavelength for different temperature, inset data and linear fit of the variation in wavelength as function of temperature.

Fig. 2.5 shows how the lasing spectra develop as function of temperature. The laser spectra is composed of several peaks with a separation between peaks below the resolution of our optical spectrum analyzer (OSA) of 0.07 nm.

Fig. 2.5 shows a red-shift of the emission wavelength increasing the tempera-

ture. Starting from $\lambda = 1237$ nm at T $= 9.2°$C the spectra constantly red shift increasing the temperature. At T $= 53°$C the central emission is $\lambda = 1262$ nm. A linear fit on the center of the spectra has been made to see how this shifts as function of the temperature (inset of Fig. 2.5). The data give a red-shift of 0.53 nm/$°$C. This is in agreement with value reported in literature [40].

2.2.4 Divergence behavior

The measurement of the beam divergence of a quantum dot laser (QDL) diode is important because from that is possible to infer indirectly the size of the active area of the laser. Also is important to have this information to estimate the coupling efficiency and the beam parameter for applications in external cavity.
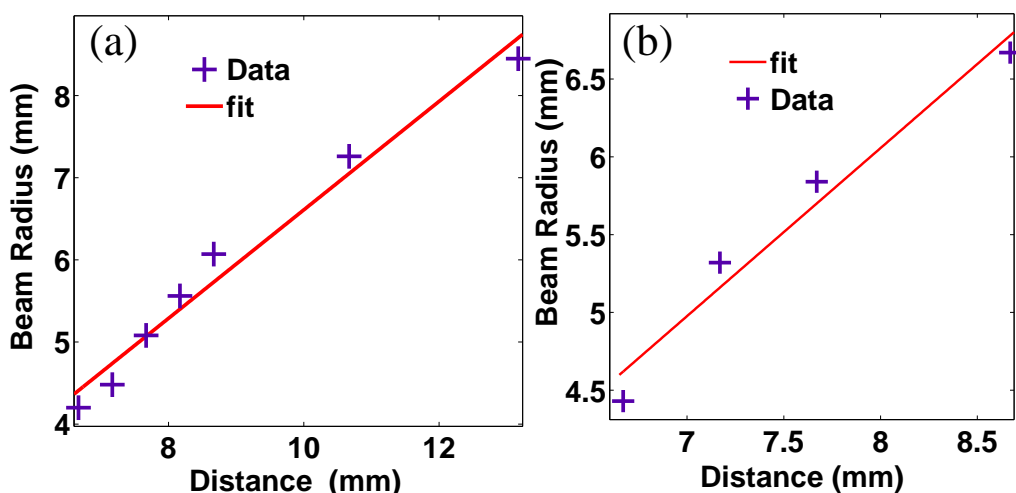
Figure 2.6: (a) Measured beam radius in slow (horizontal) on a linear fit (straight line) (b) Measured beam radius vertical (points) on a linear fit (straight line).

The measurement are made by putting an InGaAs Camera at various distances from the laser. The camera (Hamamatsu C 8061-01) is an image sensor with an active area of (12.8×0.25) mm. It is made of 512 pixel and each pixel is 25 μm wide. Due to the fact that the camera saturates easily we put a filter to prevent saturation. The filter not only attenuates the beam but changes also the beam

path due to the refractive index. The data presented in Fig. 2.6 are corrected for this.

The divergence angle of the beam can be determined increasing the distance between camera and QDL and taking a picture for each distance setting. Fig. 2.6 shows how the beam radius changes as function of the distance from the laser facet. Once the beam profile is taken we fit to a Gaussian to obtain the beam radius at $1/e^2$ intensity. The data of Fig. 2.6 show a linear dependence, as expected since the distance from the camera to the laser is much bigger than the Rayleigh length of the beam, Fig. 2.7. In this case a linear fit gives the divergence of the beam and the beam waist can be obtained from the formula: $w_0 = \lambda/(\pi\theta)$, ref. Fig. 2.7.

From the fit the coefficient for the fast axis can be obtained $\theta = 66.9°$ and so $w_0 = 0.68$ μm.
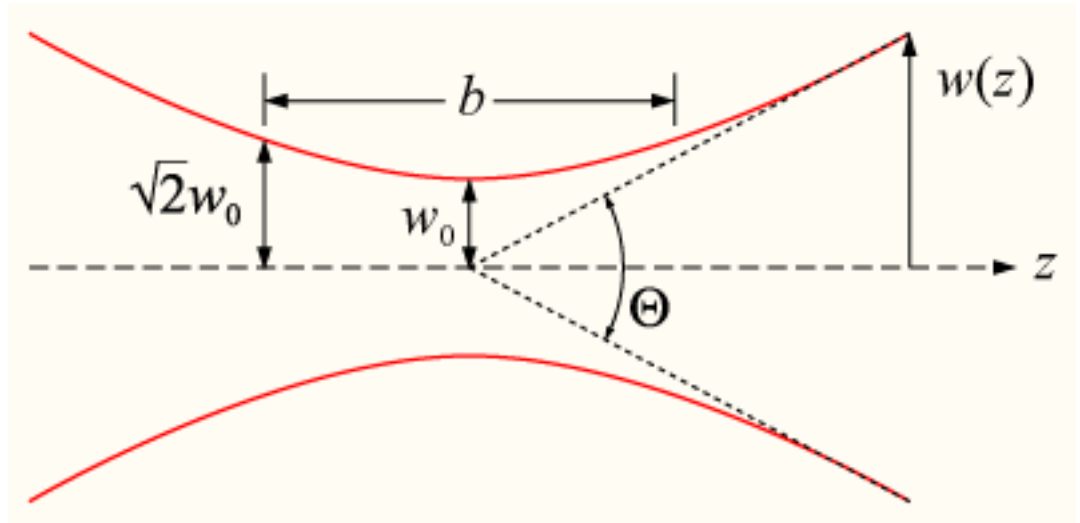
Figure 2.7: Gaussian beam width w(z) as a function of the axial distance z. w_0: beam waist; b: depth of focus; z_R: Rayleigh range; θ: total angular spread

The same measurement were taken for the slow axis direction of the beam tilting the camera of an angle of 90°. From the fit in Fig. 2.6(b), we find the relevant parameter for the measurement of the beam divergence in the vertical direction to be: $\theta = 12.3°$ and $w_0 = 3.67$ μm.

2.3 Narrow band light source based on QDL

Due to the inhomogeneous broadening and the coexistence of ground state and excited state emission, quantum dot lasers have a good potential for widely tunable laser [77] and/or for mode-locking [78; 79] providing some advantage over the alternative approach to approach this spectral region using InGaNAs quantum well material [80; 81].

Indeed tuning in excess of 80 and 160 nm was demonstrated in the 1.1 μm [82] and 1.5 μm range [83; 84] though in the latter case under pulsed conditions and with a rather low output power. The record result seems to be a tuning range of 201 nm extending from 1033 to 1234 nm [53] but the emission linewidth seems to be rather large. More detailed investigations concentrating on the 1230 nm range also do not report data on emission linewidths in the grating controlled regime [85]. Single-frequency, narrow-linewidth operation of quantum dot lasers with reasonable power levels (about 10 mW) is achieved using the distributed-feedback approach (e.g., [86; 87]). Tunability is limited, however.

A lot of research on device optimization in the 1200-1300 nm regime concentrated on high-power broad-area lasers [27; 36; 68; 70] having however a rather low temporal and spatial coherence. Motivated by the success in improving the coherence of broad-area diodes in the near infrared range of the spectrum (670-980 nm) [88; 89; 90], it appears naturally to investigate the performance of QDL in external cavities. We present here first studies on using these lasers for producing tunable, fairly high power emission laser emission below and at the edge of the O-band where no well established commercial lasers are offered. Applications for low bandwidth – though not necessarily single-frequency – sources include medical applications, sensors, second-harmonic generation to bright red wavelengths in the wavelength range of the HeNe laser and – actually our current interest – nonlinear optics of quantum dot materials.

2.3.1 Littrow and Littman configuration

Two common configurations are used to realize frequency-selective feedback, as shown in Fig 2.8. The first possible is the Littrow configuration [91], Fig 2.8 (a).

Here the first order of the beam reflected from the grating is directed back into the laser diode.

The other one is the Littmann-Metcalf configuration [92], Fig 2.8 b) it consists of the grating and an additional mirror. The beam coming from the QD is reflected by the grating onto the mirror and back to the laser via the grating.
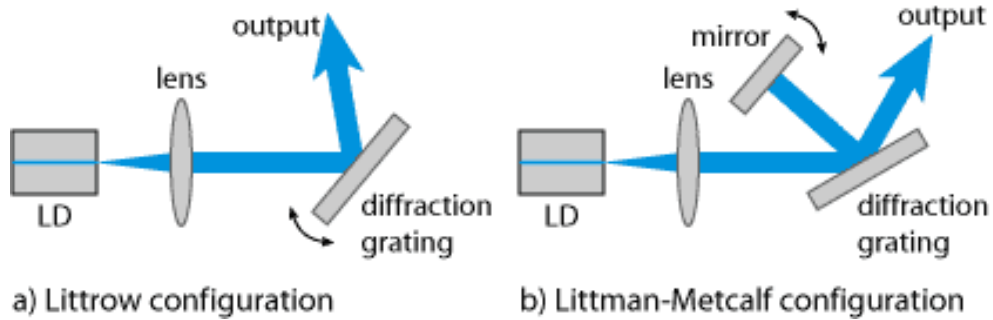
Figure 2.8: (a) Littrow configuration, (b) Littmann-Metcalf configuration

The double-pass increases the frequency-resolution of the feedback. Tilting the mirror changes the feedback frequency. These feedback configurations are commonly used to tune edge emitting laser diodes over a wide wavelength range [93; 94], e.g. for spectroscopic applications [95]. Tunable semiconductor lasers with high output power using one of these configurations are commercially available nowadays.

2.3.2 Experimental Setup

The experimental setup is illustrated in Fig. 2.9. Feedback is provided to the facet which is positioned at the edge of the C-mount (apposite mounting for the diode). The design of the external cavity follows the scheme proposed in [88; 89] though we are using a Littman configuration. A Littrow scheme was tested also yielding higher threshold reduction, which is in accordance with expectation, but the frequency selectivity was found to be insufficient. The emission in the fast axis is nearly collimated using an aspherical lens (FAC) of 0.9 mm focal length and numerical aperture NA = 0.8. Since its alignment is critical, the FAC is mounted on a translation stage that can control all five alignment degrees of freedom of

the lens. After this, there is a telescope-like system made by two lenses with focal
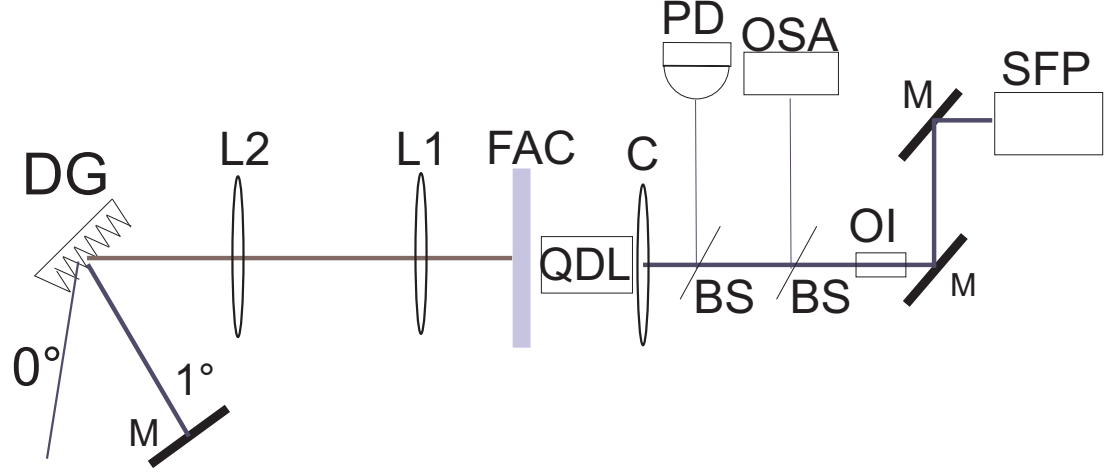
Figure 2.9:   Experimental Setup: M mirror, DG diffraction grating, lenses: L1 ($f = 35$ mm), L2 ($f = 200$ mm) lenses, FAC fast axis collimator (cylindrical, aspherical lens with $f = 0.9$ mm), C aspherical collimator ($f = 8$ mm), QDL quantum dot laser, BS beam sampler, PD photo diode, OSA optical spectrum analyzer, OI optical isolator, SF scanning Fabry Perot interferometer.

lengths of $f = 35$ mm and $f = 200$ mm, respectively. Their exact distance is adjusted such that the frequency selectivity of the setup is optimized. A plane ruled diffraction grating with 1200 lines/mm is arranged at an angle $\Theta = 70°$ with respect to the incoming beam. The diffraction efficiency of the grating in the first order is 93%. The beam from the first diffraction order is retro-reflected by a highly reflective mirror. The distance between the two lenses L1 and L2 is approximately equal to the distance between the last lens L2 and the mirror. The latter distance is found to be a critical parameter in order to achieve low bandwidth operation. The total cavity length is about 270 mm.

For detection, the other facet of the laser diode is used. Since it is recessed from the edge of the C-mount by 2.5 mm, the mounting blocks some part of the output (actually it reflects it upwards). Due to the fact that the mode structure in the vertical (fast) direction is given by the waveguide of the diode, it is expected that the properties of the upper and the lower part of the beam are the same and that the results obtained by detecting only half of it are meaningful. A photodiode is used to monitor a signal proportional to the total output power.

The optical spectrum is measured by a commercial fiber coupled optical spectrum analyzer (Agilent 86140) with a nominal resolution of 0.07 nm. The main beam is sent to a plane-plane scanning Fabry-Perot interferometer (SFP) with a free spectral range of 125 GHz and a resolution of 2 GHz (Finesse $F = 63$; mirror reflectivity 95%). An optical isolator is put in the path of the beam to prevent back reflection from the SFP.

2.3.3 Results and Discussion

The absolute output power is measured with a calibrated power meter after the collimator C. Fig. 2.10 shows light-current (LI) characteristics of the diode with and without feedback.
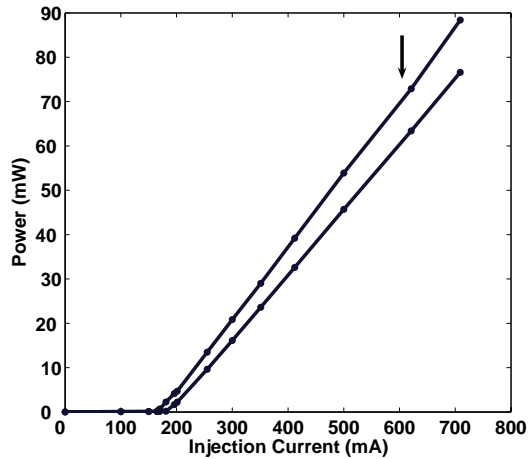
Figure 2.10: Output power as function of the injection current. The upper line corresponds to the laser with feedback, the lower line to the free-running laser. The arrow indicates the limit in which the spectrum of the laser with feedback remains single-humped.

The upper line indicates the power in the feedback configuration whereas the lower one is that of the free running laser. Due to the partial blocking of the

output beam by the mount, the real power level is roughly double the measured one.

In both cases the LI-characteristic is linear in a good approximation. The threshold current($I_{th,1}$) of the laser with feedback is reduced to I = 170 mA compared to I = 195 mA for the free-running diode. The increase of slope of the LI-curve with feedback is due to the reduced losses at the other facet. The arrow indicates where the spectra show a transition from a single hump to multiple ones. This means that we can achieve a fairly high power (about 140 mW) with low-bandwidth (see below).
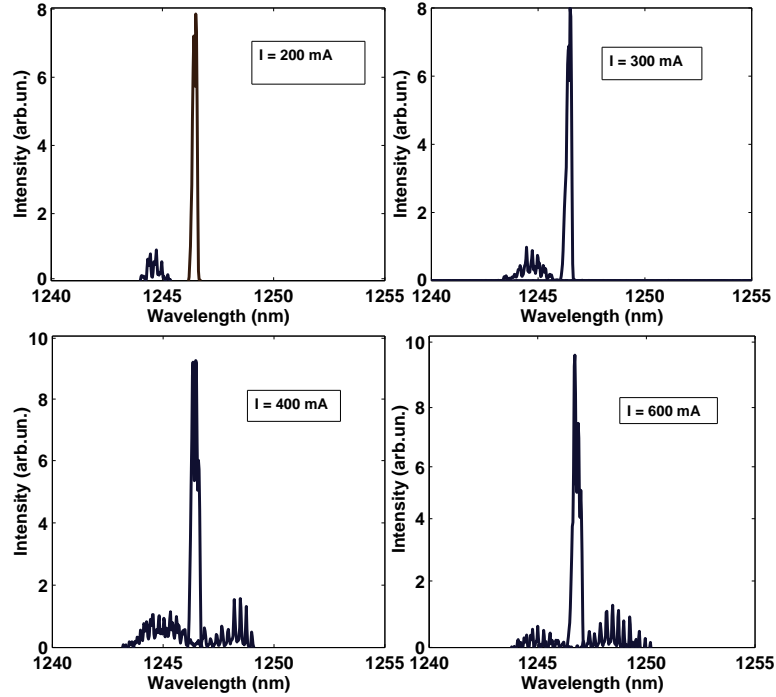
Figure 2.11: Spectra obtained with the OSA for 200, 300, 400, 600 mA injection current. The narrow peak corresponds to the laser with feedback, the broad spectrum to the free-running laser.

Careful transverse and longitudinal alignment of the FAC and of L1 and L2 lead to the narrow linewidth emission results shown in Fig. 2.11. Fig. 2.11 compares the spectra of the free-running laser and of the laser with feedback at

different current levels. The free-running laser has a spectral width of $\delta\lambda = 3$ nm at I $= 200$ mA, increasing to $\delta\lambda = 4$ nm at I $= 300$ mA and to 7 nm at I $= 600$ mA. The spikes within the envelope are separated by either 0.15 nm or by 0.3 nm which correspond to one or two free spectral ranges of the diode (being 0.15 nm), i.e. they represent longitudinal modes. Below I $= 350$ mA, the envelope is single-humped but it becomes double-humped above.

Instead, for the laser with feedback, we have, according to Fig. 2.11, narrow bandwidth emission with a linewidth (FWHM) that varies from 0.07 nm (the resolution of the spectrometer) for I $= 200$ mA to 0.5 nm for I $= 600$ mA. This means that at low currents essentially only one longitudinal mode of the diode is excited though the laser is operating on multiple longitudinal modes of the external cavity, of course. Due to the broad-area gain region, also multiple transverse modes are still active. In order to get a better frequency resolution,
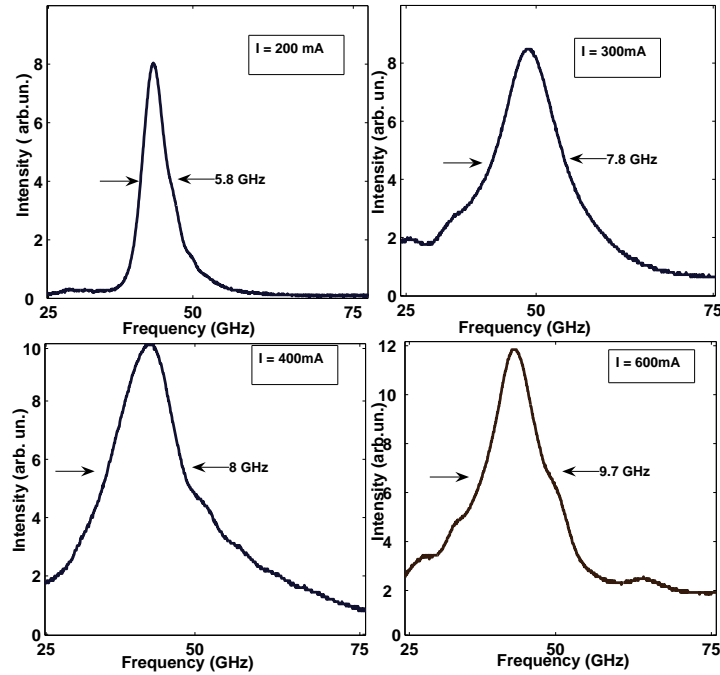
Figure 2.12: Spectra obtained with SFP for 200, 300, 400, 600 mA injection current.

the scanning Fabry-Perot interferometer was used to analyze spectral bandwidth of the laser. Figure 2.12 shows four spectra for injection currents of 200, 300, 400,

600 mA. This spectra were taken at a different time than the ones in Fig. 2.11. For I = 200 mA we have a spectrum with a width of 5.8 GHz or $\delta\lambda = 0.03$ nm which corresponds to an improvement with respect to the free-running laser of more than one hundred times at that current. Increasing the current, the spectra tend to broaden and acquire some background. For I = 600 mA the measured width is 9.7 GHz. The overall spectral behavior does not change qualitatively up to an injection current of 600 mA. Beyond this current, additional peaks appear in the spectrum.
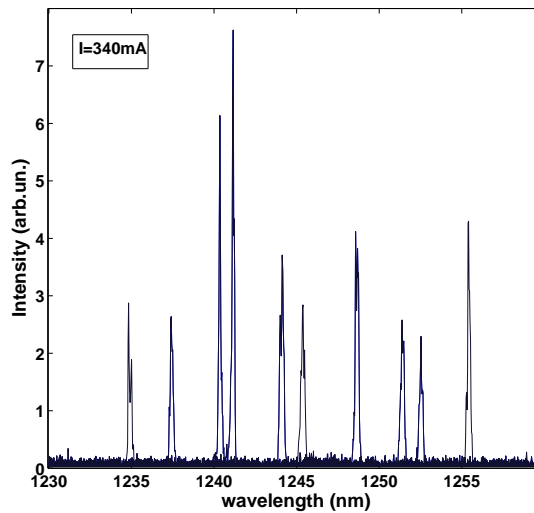
Figure 2.13: Tuning range of the laser with feedback starting at 1235 nm and ending at 1255 nm. The spectra are taken with the OSA at $I = 340$ mA by manually tuning the rotation of the grating.

Turning the grating we obtain a tuning range of 20 nm (Fig. 2.13) at a current of 340 mA ($2 \times I_{th}$) which corresponds to an extracted power of 25 mW. The central wavelength of the tuning correspond to a wavelength of $\lambda = 1240$ nm and the range extends from to 1235 nm to 1255 nm.

Interestingly, this tuning range and the location of maximum output power with feedback are blue-shifted by about 5 nm to the wavelength of the free-running laser (see Fig. 2.13). The spectral width varies between $\delta\lambda = 0.07$ nm (resolution of the spectrometer) and 0.1 nm.

2.4 Characterization of small area QDL diode

So far results on the improvement the coherence of broad-area quantum dot laser have been presented, but the QDL diode analyzed still at higher current is multimode and hence present difficulty for coupling the beam in single mode fiber for applications. Hence we turn our attention to a small-area diode with anti-reflection coating. The performance of commercially available state-of-the art external cavity lasers are on the order of 100khz.

2.4.1 Sample and characterization

The QDL, from Innolume GmbH, has a length of L = 3.5 mm and a stripe width of $w = 5$ μm. One facet of the QDL diode is AR coated while the other is HR coated. The semiconductor structure for the gain chip was grown by molecular-beam epitaxy. The gain region consists of 10 QD planes [96; 97], Fig. 2.14 for layer structure specification. The temperature is controlled by a Peltier element.

Layer	Material	Group	Repeat	Mole fraction (x)		Thickness (nm)	Doping profile		Type	Dopant
				start	finish		start	finish		
14	GaAs					200	1e20		P	C
13	Al(x)Ga(1-x)As			0.15	0	20	1e19		P	C
12	Al(x)Ga(1-x)As			0.15		1800	5e17		P	C
11	Al(x)Ga(1-x)As			0.15		700	2.5e17		P	C
10	GaAs					100			U/D	None
9	GaAs	1	10			35			U/D	None
8	In(x)Ga(1-x)As	1	10	0.15		5			U/D	None
7	InAs*	1	10			0.8			U/D	None
6	GaAs					35			U/D	None
5	GaAs					100			U/D	None
4	Al(x)Ga(1-x)As			0.15		1000	5e17		N	Si
3	Al(x)Ga(1-x)As			0.15		1500	1e18		N	Si
2	Al(x)Ga(1-x)As			0	0.15	15	3e18		N	Si
1	GaAs					500	3e18		N	Si
0	GaAs substrate			N+ GaAs 3 inch						

Figure 2.14: Layer structure specification.

Fig. 2.15 (a) show the typical spontaneous emission spectra (PL) of this QDL laser. It is centered at 1235 nm with a width of around 30 nm and a FWHM of 10 nm. The laser threshold is about 400 mA. The power at 1 A is 232 mW at room temperature, inset of Fig. 2.15 (a).
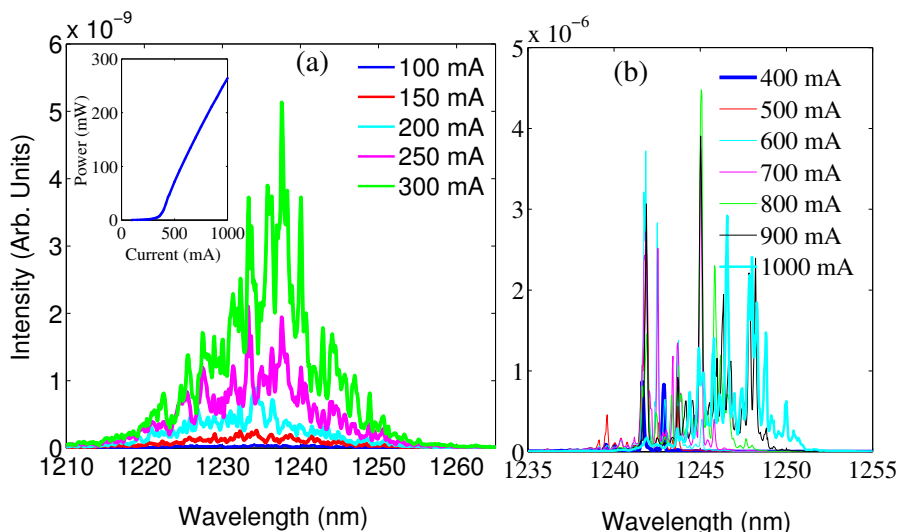
Figure 2.15: (a) Spontaneous emission spectra for increasing current, inset LI curve at room temperature. (b) Lasing spectra for increasing current.
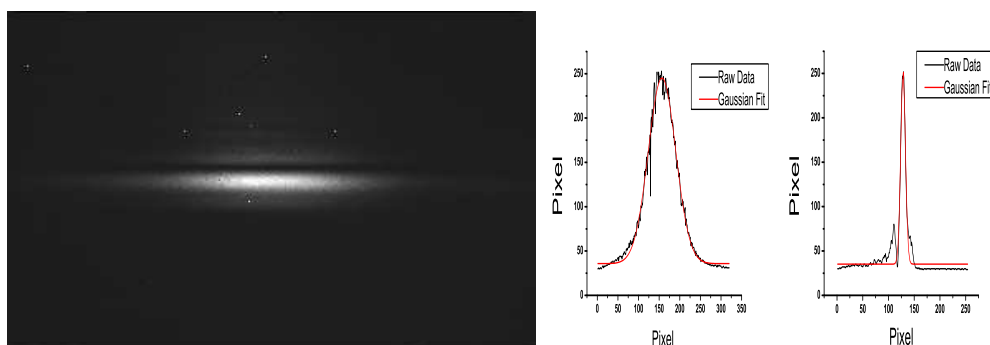
Figure 2.16: Left: Imaging of the beam at d = 930 mm, (M = 316.7), Right horizontal and vertical cut along the image with fit.

Fig. 2.15 (b) shows the lasing spectra of the diode. It possible to see that increasing the current several peaks appear at higher wavelength. The position of the peak is random and the average width is about 0.5 nm.

Fig. 2.16 show a typical emission profile from the QDL taken with a InGaAs camera (NIR-300/F) at a distance of d = 950 mm. Calculating the magnification given by the distance from the lens to the camera and the effective focal length of the lens is possible to infer the beam size in both direction of the beam. From

36

the fit of the profile in the horizontal and vertical direction turn out that the vertical size is 0.62 μm, limited by the numerical aperture (NA) of the lenses and the horizontal one is 3.62 μm.

2.4.2 Littrow and Littman configuration

The threshold reduction in the Littrow configuration is shows in Fig 2.17 (a) as function of the wavelength. The error bar is given by the size of the data points. The maximum threshold reduction is around the gain peak, $\lambda = 1230$ nm and is about I = 62 mA and then the threshold increases towards lower and higher wavelengths. Compared to the threshold of the free running laser this is a threshold reduction of 35 %.
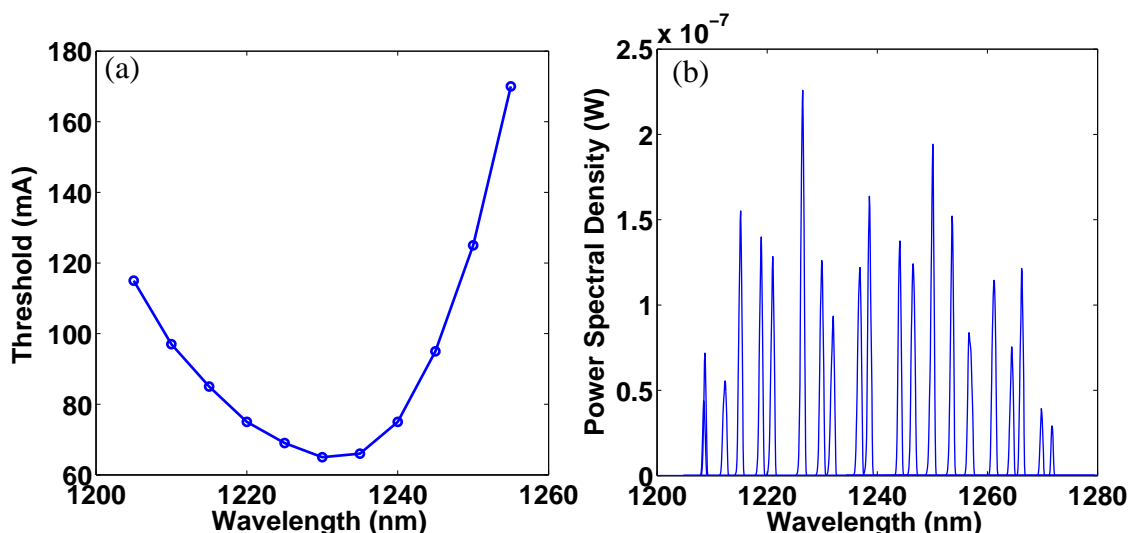
Figure 2.17: (a) Threshold in Littrow setup, (b) tuning range in Littrow setup.

Fig 2.17 (b) shows the tunability of the diode tilting the grating. A tuning range from $\lambda = 1205$ nm to $\lambda = 1270$ nm is achieved.

Instead, in the Littman case we have a threshold of I = 80 mA at $\lambda = 1230$ nm, Fig 2.18(a), and a tuning tuning range from $\lambda = 1205$ nm to $\lambda = 1270$ nm.

Fig 2.19 shows the power available with both configurations. In the Littrow configuration a maximum output power of 100 mW is achievable at $\lambda = 1230$ nm,
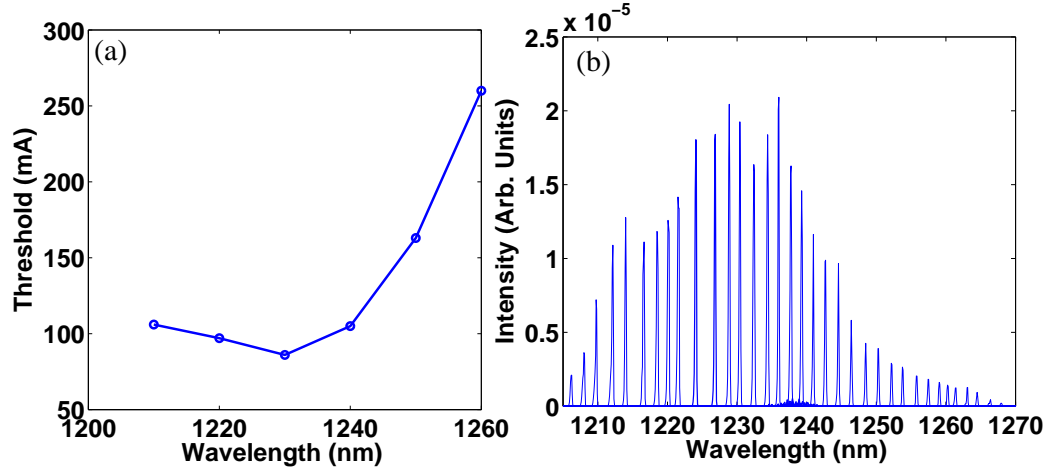
Figure 2.18: (a) Threshold as function of wavelength in Littmann configuration (b) tunability.

decreasing to 75 mW at $\lambda = 1260$ nm. Fig 2.19 (b) shows instead that in Littmann configuration only half of the power is available.
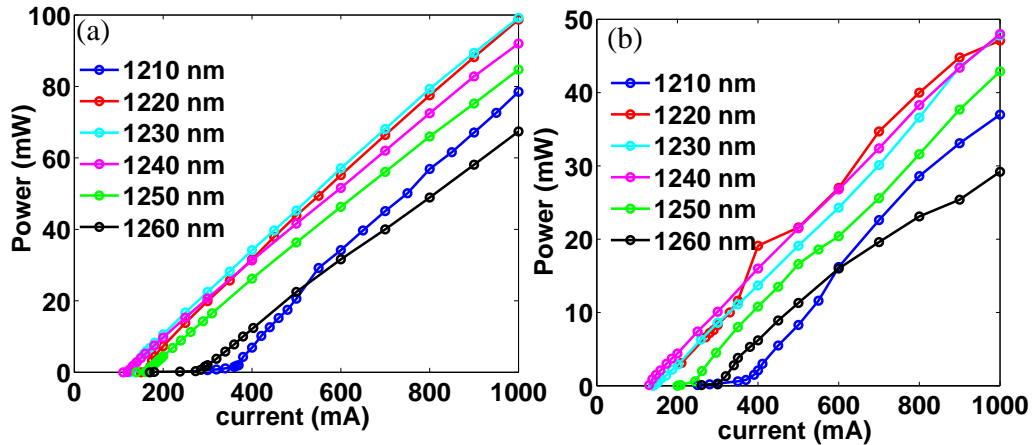
Figure 2.19: (a) Power versus current in Littrow configuration, (b) Power versus current in Littmann configuration.

Fig 2.20 shows the FWHM of emission achievable in Littmann configuration showing that is almost constant around 0.16 nm and also that it stays constant
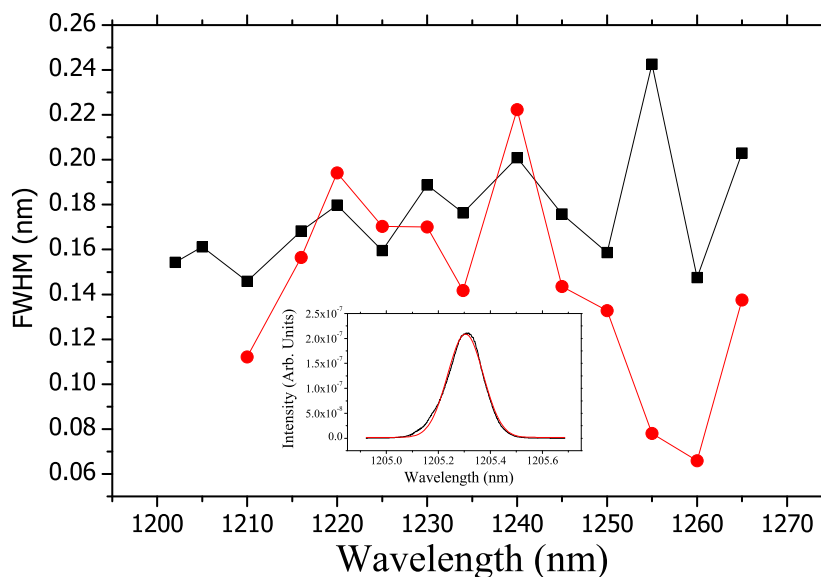
Figure 2.20: FWHM as function of wavelength, in Littmann configuration, for two currents, red curve threshold current, black curve I = 1000 mA, inset spectral profile and fit.

at hight current (black curve) showing a very good feedback level achievable for currents up to 1 A. The FWHM of emission achievable in Littrow configuration is 0.16 nm also.

2.4.3 Discussion

So far the performance and reliability of two kinds of quantum dot laser diodes have been analyzed. In section 2.3 we analyze broad area (100 μm) laser diode. A remarkable bandwidth of 5-10 GHz at power levels of 10-140 mW was demonstrated [58] sufficient for many applications as investigating the nonlinear optics of QD. Nevertheless, due to the broad area of the laser diode, it is normal that the laser emit a number of transversal modes adding to the complexity of the laser chip mode spectrum so the output spectrum is a mix of the transversal mode spectrum and the modes of the EC. Indeed, this is more visible at hight current, where the laser became strongly multimode as discussed in section 2.3.2.

Expected significant improvement of performance come by anti-reflection (AR)

coating of the facet [96] on which the feedback is done. Indeed this was the case when we analyze the small area laser diode (5 μm) with anti-reflection coating, of section 2.4.

In that case we achieve in Littmann and Littrow configuration a bandwidth of 0.20 nm for all the wavelength achievable turning the grating and especially for all the current available. The beam stays single mode even at higher current compared to the previous case, where at higher current the beam is no more single mode.

Normal external cavity commercial lasers have a linewidth of 100 kHz but we observe few GHz due to the grating involved and the stripe width of the lasers.

Nevsky et al. [96] reached a tuning range exceeding 200 nm as well as an output power of more than 500 mW at a central wavelength of about 1180 nm using a 5 μm wide bent ridge with a normal output facet and 5° tilted rear facet. Nevertheless the linewith reduction is still in the order of several kHz. They are using sample not currently commercially available.

An important application of the diode will be analyzed in the next section.

2.5   Stacked binary InAs-GaAs quantum dot structures

Quantum dot based optoelectronic devices open a new pathway to realize laser and other photonic devices in the 1.3 μm region of the electromagnetic spectrum, where a mature and well developed fiber technology exists due to its relevance to telecommunications. We concentrated on lasers and amplifiers.

Terahertz radiation is non-ionizing submillimeter microwave radiation and shares with microwaves the capability to penetrate a wide variety of non-conducting materials. Terahertz radiation can pass through clothing, paper, cardboard, wood, masonry, plastic and ceramics. It can also penetrate fog and clouds, but cannot penetrate metal or water [98].

One important option for THz generation is photomixing of two cw beams or photoconductive switching with a mode-locked laser in semiconductors with an

antenna structure. Most efforts so far have concentrated on LT(Low Temperature)–GaAs or LT–InGaAs excited by lasers in the 780-1060 nm range [99; 100; 101; 102].

Many applications in astronomy or sensing would highly benefit from a coherent distribution of the laser radiation over larger distance based on fibers, i.e. demand wavelengths in the 1.3 or 1.5 μm bands.

We present result on two stacked binary InAs/GaAs QD structures (no. 1949) grown under surfactant-mediated growth conditions at two different temperatures and a superlattice structure (no. 1753). The growth technique will be illustrated in the following section followed by a discussion of some of the structural, optical and electrical properties of these samples and some applications in which they can be involved

These samples can be used as ultrafast photoconductive PC materials for generating and detecting terahertz radiation using photomixing or broadband pulsed techniques [103]. Both techniques require PC materials with an ultrashort carrier lifetime for fast response and a very high resistance to minimize the dark current in the THz emitters and detectors. LT GaAs is one of the well known materials that are used for this purpose; however, its band gap prevents the use of telecom lasers for excitation. The two samples studied in this work can be used as alternatives due to the narrower bandgap material embedded in the structure, i.e. InAs.

2.5.1   Sample and experimental setup

The sample (no. 1949) is made of 10 layer of InAs-GaAs quantum dots (QDs) structure, grown by molecular beam epitaxy (MBE) at T = 450 °C growth temperature [104]. The InAs layers (3ML) were grown under surfactant growth conditions where only the In beam impinged upon the growth surface. The group V uptake was provided by the residual arsenic in the growth chamber. This growth mode results in the formation of quantum dots with dot sizes that much smaller than those for normal growth (NG) of 3ML InAs-GaAs QD structures, and a good growth quality as determined by double crystal x-ray diffraction (DCXRD) measurements.

Device No.	Total Length (μm)	Gap Length (μm)	Bow Angle (deg)
1A	416	3	60
1B	416	3	90
1C	416	5	60
1D	416	5	90
2A	416	10	60
2B	416	10	90
2C	416	20	60
2D	416	20	90
3A	500	5	60
3B	500	5	90
3C	500	20	60
3D	500	20	90
4A	333	5	60
4B	333	5	90
4C	333	20	60
4D	333	20	90
5A	Square pads(side_200 μm) (separation_50 μm)		
5B	Square pads(side_200 μm) (separation_100 μm)		
5C	Square pads(side_200 μm) (separation_50 μm)		
5D	Square pads(side_200 μm) (separation_100 μm)		
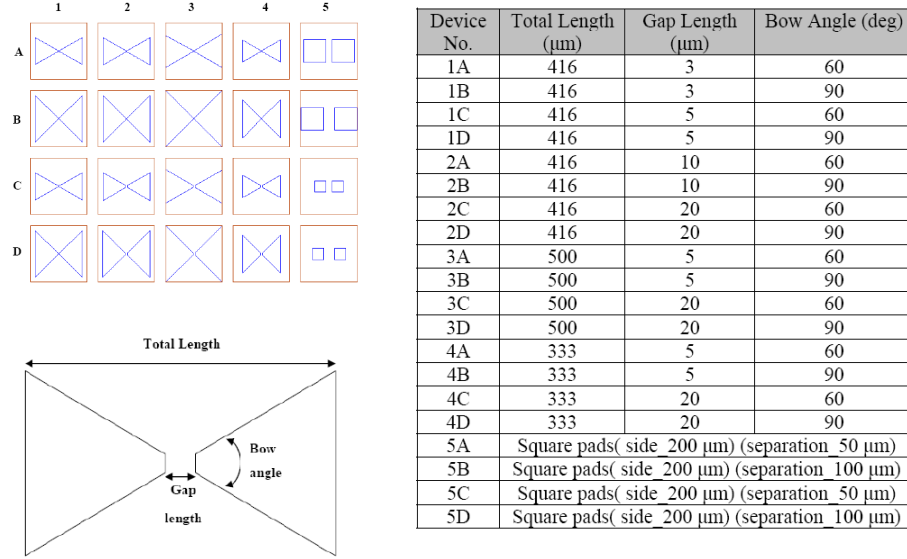
Figure 2.21: Several sets of Bow-tie antennas. Each set contains 20 devices and the following figures and table show the dimensions of these antennas.

At low substrate temperature (LT), T = 250 °C, and under the same Arsenic free growth condition, a very high quality InAs-GaAs structure was grown with up to 3MLs of InAs as demonstrated by TEM and the very well defined DCXRD spectra. Thus the critical thickness of InAs can be extended well beyond the 1.7ML limit seen at higher growth temperatures.

In order to measure the resistance and the responsivity of the samples to the 1.3 μm excitation, PC devices have been fabricated by depositing bow-tie shape metal contacts with a gap length of 5 μm. Fig. 2.21 shows the structure of the Bow-tie antennas. Each set contains 20 devices and the following figures and table show the dimensions of these antennas. The side of antenna are biased at 20-30 V by connecting with probe tips with 6 μm radius. If two lasers with frequency differences in THz region are directed into the gap, they create an oscillating carrier-density and due to the bias an oscillating photocurrent, which emits a THz wave.

The experimental setup is shown in Fig. 2.22. Two different devices are used as laser source. The first one is a commercial tunable laser from Santec (TSL-210V).

It has a tuning range of 100 nm from $\lambda = 1260$ nm to $\lambda = 1360$ nm with FWHM less than 0.07 nm. The output is coupled to a single mode fiber. The power reachable span from 14 mW at $\lambda = 1260$ nm up to 35 mW at $\lambda = 1340-1360$ nm.

The second one is the tunable source made from the QDL configured in Littman configuration. We use littmann configuration because the beam position doesn't move in space like in the Littrow configuration. The wavelength range is as reported in Fig. 2.18(b) at power levels like Fig. 2.19(b). We couple the laser diode to a single mode fiber using an anamorphic prism plus an aspheric lens. The coupling efficiency reached is about 30% at all the available wavelengths.
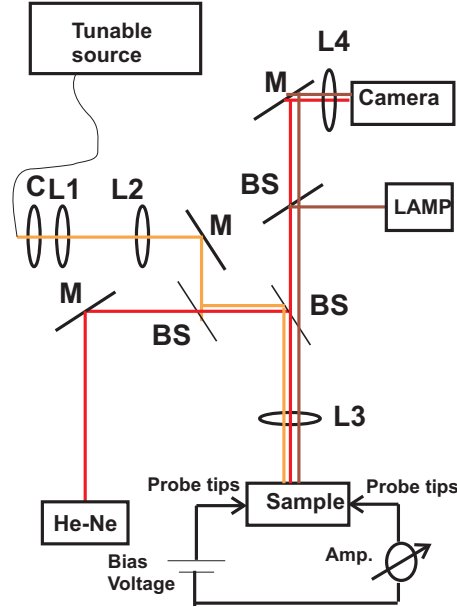
Figure 2.22: Experimental setup: C collimator (f = 3.1 mm), L1 (f = 50 mm), L2 (f = 150 mm), L3 (f = 50 mm), L4 (f = 200 mm), M mirror, BS beam splitter, He-Ne Helium-Neon laser.

The emission of the laser is collimated using an aspherical lens (C) of 3.1 mm focal length and numerical aperture NA = 0.68. After that two lenses L1 and L2 are used for beam shaping. We focus onto the sample with a lens L3 of focal length of f = 50 mm. The beam radius, as came out from imaging the beam on the camera, are $w_x = 4.5$ μm and $w_y = 6.3$ μm.

A second system is used for imaging the sample. A commercial lamp illuminates the surface of the sample so it is possible to see the area of the antenna with the camera, sensible to visible radiation.

A He-Neon (He-Ne) laser also is sent to the surface of the sample and the reflected beam is spotted by the camera. We use in addition the He-Neon laser due to the fact that the camera used is not sensible to the infrared region. The He-Neon and the infrared beam are carefully superimposed.

Fig. 2.23 shows the dark resistance of the sample as a function of the annealing temperature. Sample no 1949 shows high resistance caused by the QDs acting as traps for the carriers. Annealing showed no significant effect.
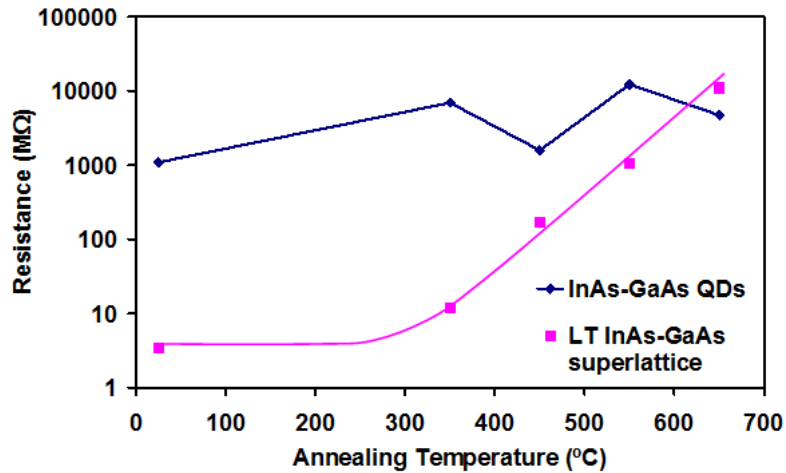
Figure 2.23: Dark resistance as a function of the annealing temperature.

In contrast, the resistance of sample no. 1753 is very low for an unannealed sample due to the conduction via hopping between midgap states created by As point defects. The reduction in the point defects density after annealing, in addition to the formation of As clusters which form depletion regions around themselves acting as buried Schottky barriers, leads to a dramatic increase in the resistance.

It is worth to notice that a photoluminescence is present from the quantum dot sample (no. 1949) but no PL comes out of the superlattice (no. 1753).

2.5.2   Results

Photocurrent measurements were performed with the tunable sources and fairly high photocurrent peaks around the ground state transition peak were observed.
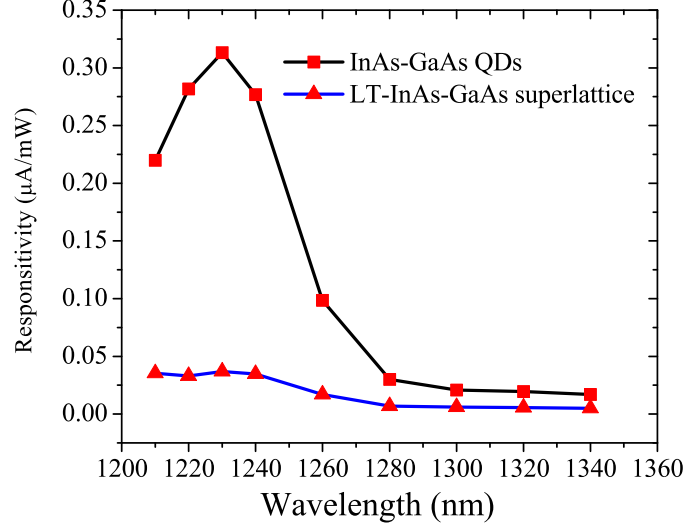
Figure 2.24: Current responsivity as a function of the excitation wavelength, both samples are unannealed, gap length 5 μm, bias 20 V.

Fig. 2.24 shows the current responsivity as a function of the excitation wavelength at 20 V bias for the two samples: the InAsGaAs quantum dot and the LT superlattice. There is a strong photocurrent from the QD sample, with a peak reached at $\lambda = 1230$ nm, after the photocurrent decreases to reach a constant value from $\lambda = 1280$ nm to $\lambda = 1340$ nm. Instead the superlattice shows less pronounced photocurrent that stay constant from $\lambda = 1210$ nm to $\lambda = 1240$ nm to drops after.

Our group report also photocurrent of 0.24 μA/mW for LT-GaAS bow tie with 10 μm gap, taken with a Ti:Sapphire laser at 780 nm [105]. This value is 10 times bigger than the LT-InAs-GaAs superlattice reported in Fig. 2.24 probably due to the sample thickness. The LT-GaAs is normally one micron of bulk material which absorbs the impinging radiation completely whereas the absorption is low, in the some % range for the superlattice.
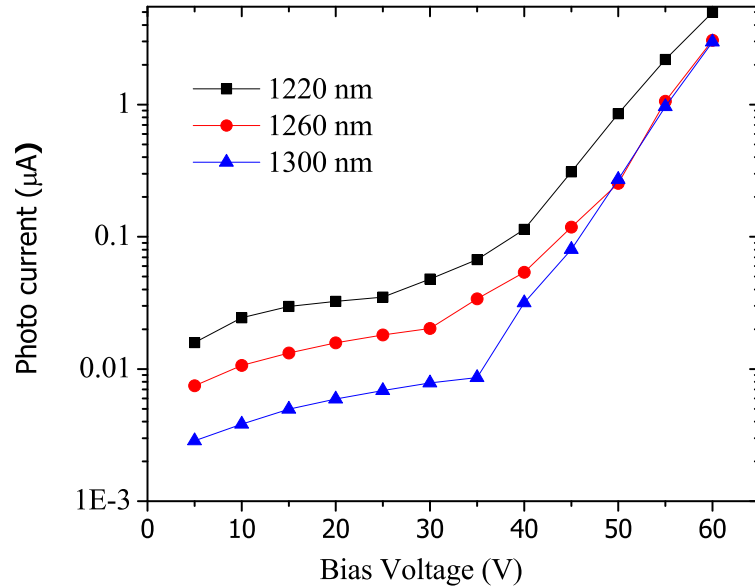
Figure 2.25: Photocurrent vs. voltage for QD samples excited with 5 mW.

Fig. 2.25 shows how the photocurrent changes as function of bias voltage applied to the antenna (ref. Fig. 2.22), with fixed input power, in this case set to 5 mW. It is possible to see that the photocurrent is low until a bias voltage of 35 V is applied. After that there is an exponential increase of the photo-current is observed. At low wavelength $\lambda = 1220$ nm there is more photocurrent than at high one.

Fairly hight photocurrent has been found also from sample, superlattice were doesn't appear a PL. These are, to our knowledge first results on photocurrent in InGaAs quantum dot and superlattice for THz applications. Photocurrent is hight for QD than for superlattice probably due to different lifetime. Indeed the lifetime of the superlattice is low (some hundreds of fs) compared to the QD.

Chapter 3

Opto-thermal pulsations in a quantum dot edge-emitting laser diode

3.1 Introduction

One subject of interest in quantum dot lasers are self-pulsing lasers where self-Q-switching due to saturable absorption was observed in many devices [106; 107; 108; 109]. Pulsations are in the GHz region as can be expected for passive Q-switching with the lifetime of the excited state in the nanosecond range. In VCSELs, self-pulsations observed were at a somewhat lower frequency but still in the several hundreds of MHz range and were related to saturable absorption in lateral unpumped regions of the device [110]. Self-pulsations in edge-emitting QD lasers without an intentionally introduced absorber section were also observed and explained in terms of the inhomogeneous nature of the QD gain, the existence of several confined QD states and the resulting saturable absorption by energy states lower than the laser photon energy [111]. Nevertheless, these oscillations are still in the GHz range.

It is reported here on self-pulsations in QD edge-emitting lasers without a saturable absorber section taking place on the MHz scale. The oscillation frequency hint to a thermal origin of the dynamics. Indeed, opto-thermal pulsations with a

47

very similar phenomenology were studied in quantum well amplifiers [63; 112] and are typical for a variety of other nonlinear optical systems [113; 114; 115; 116]. It was shown in [63] that the self-oscillations follow van der Pol-Fitzhugh-Nagumo dynamics [117; 118], a fairly general scenario of relaxation oscillations, which are characterized by the competition of very different time scales (in [107; 112] for example carrier dynamics and thermal relaxation).

Interestingly, the self-pulsing dynamics are found to persist if frequency-selective feedback is applied. By the feedback, the operation frequency of the laser can be tuned above, below and around gain maximum and time-resolved optical spectra show characteristic differences, which are argued to give some indication of a difference in phase-amplitude coupling above and below the gain maximum.

Bistability in the light-current characteristics is observed for wavelengths smaller than the gain peak ($\lambda = 1225$ nm), but it is not present for wavelength above the gain peak and for the free running lasers.

3.2 Opto-thermal pulsations

3.2.1 Experimental setup

The setup utilized for the characterization is shows in Fig. 3.1. The laser is a quantum dot edge-emitting diode from Innolume GmbH with a length of L = 3.5 mm and a stripe width of $w = 4.5$ μm. It contains InAs QD in a GaAs matrix. It is designed to be single spatial mode with only a shallow edged waveguide. One facet of the QDL diode is anti-reflection (AR) coated while the other is hight-reflection (HR) coated. The laser is mounted on a C-mount and the temperature is controlled by a Peltier. The output power is specified to be 300 mW at 1 A.

The emission in the fast axis is nearly collimated using an aspherical lens (C1) of 3.1 mm focal length and numerical aperture NA = 0.68. Feedback is provided in a Littrow scheme with a diffraction grating with 1450 lines/mm arranged at an angle $\Theta = 75°$ with respect to the incoming beam. The collimator is positioned in a way to optimize threshold reduction by focusing on the grating (external cavity
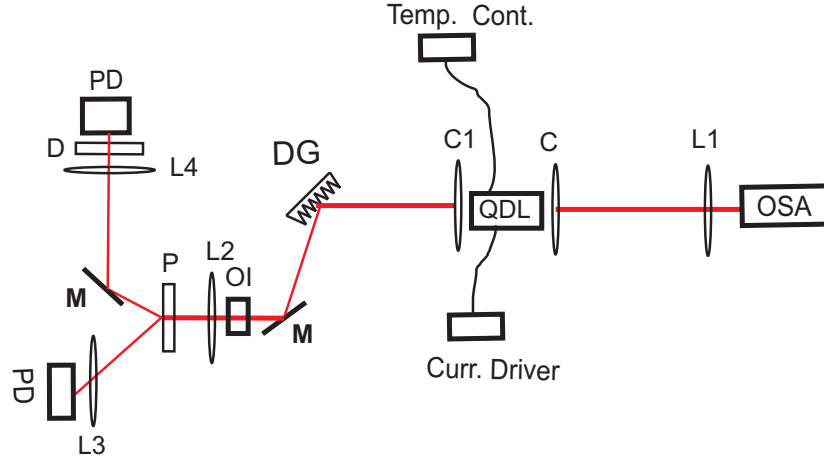
Figure 3.1: Experimental setup: mirror (M), diffraction grating (DG), aspherical collimator (C1) (f = 3 mm), aspherical collimator (C) (f = 8 mm), L1 (f = 50 mm), L2 (f = 200 mm), L3 (f = 50 mm), L4 (f = 35 mm), Wollaston polarizer (P), filter (D), Photodiode (PD).

length 123 mm). After the external cavity, there is a lens, L2, for beam shaping and an optical isolator (OI) to prevent feedback from the detection part. A Wollaston polarizer (P) splits the beam in the two polarization components, horizontal and vertical, and sends them to two InGaAs detector (Thorlabs PDA255, bandwidth of 50 MHz) to monitor the dynamics. The optical spectrum is also monitored from the HR facet of the diode by a fiber coupled optical spectrum analyzer with a nominal resolution of 0.07 nm. For the characterization of the free running laser the diffraction grating has been replaced with a mirror and the detector is placed before the Wollaston polarizer.

Fig. 3.2(a) displays the spontaneous emission spectra for increasing current (blue curve) and the lasing spectra (red color). It is possible to recognize two peaks corresponding to the ground state (GS) and the first excited state (ES1) of the emission. The first excited state is localized at $\lambda = 1120$ nm, 100 nm away from the ground state at $\lambda = 1220$ nm. Both, GS and ES1 peaks, increase with increasing current until lasing emission takes place from the GS and the ES1 emission remains constant.

Fig. 3.2(b) shows the LI-curve, for the free running lasers. The inset of Fig. 3.2(b) shows instead how the threshold of the diode changes with tempera-
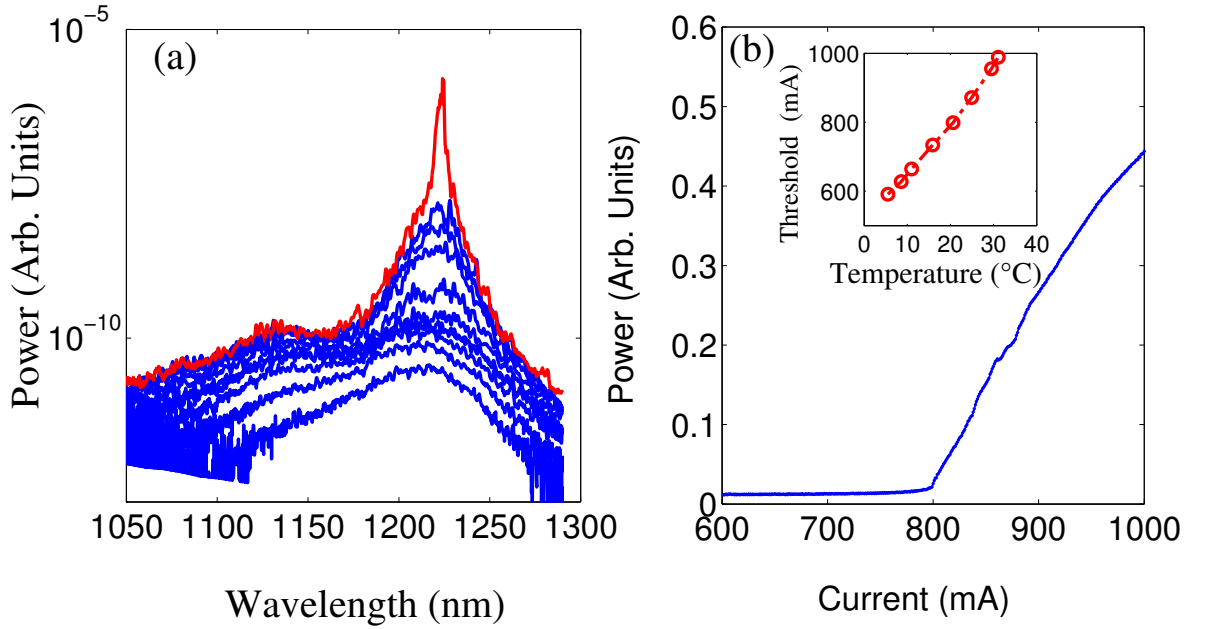
Figure 3.2: (a) Blue curves: spontaneous emission spectra for increasing current, red curve: lasing spectra. (b) LI curve for the free running laser, inset: Laser threshold for different temperature.

ture. The diode has a threshold of I = 590 mA at 5 °C that rises up to 1 A at 32 °C. Fig. 3.3 shows the optical spectra of the free running laser at I = 950 mA. There are several emission peaks in the laser. The peaks have an average distance of 0.36-0.4 nm. This would correspond to a length of 0.51-0.56 mm. This is very difficult to interpret due to the fact that the length of the diode is 3.5 mm and the longitudinal mode of the QDL are not resolved.

The tuning range of the setup is displayed in Fig. 3.4. Turning the grating, it is possible to obtain a tuning range of 70 nm from 1190 nm to 1260 nm. The central wavelength of the tuning correspond to a wavelength of $\lambda = 1225$ nm. The spectral width varies between $\delta\lambda = 0.1$ nm and 0.2 nm.
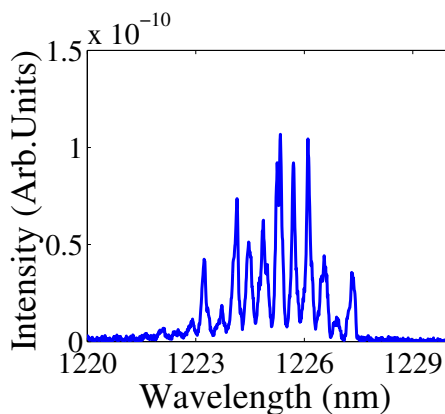
Figure 3.3: Lasing emission spectra at I = 950 mA.
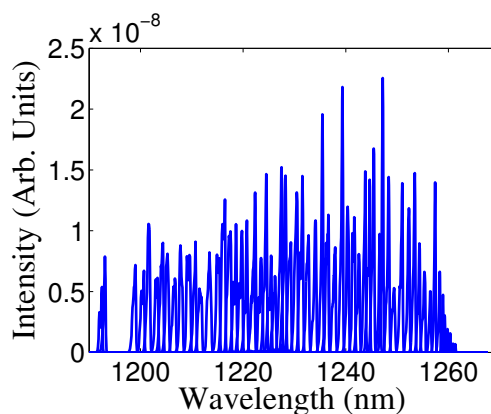
Figure 3.4: Tuning range of the laser with feedback starting at 1190 nm and ending at 1260 nm. The spectra are taken with the OSA at different current levels by manually turning the grating.

3.2.2 Dynamics of the free running laser

The QDL shows pronounced intensity pulsations (Fig. 3.5) starting at the threshold of the laser (Fig. 3.5(a)). They are large amplitude pulses on a small background. With increasing drive current their frequency increases and reaches a maximum characterized by approximately 50% duty cycle (Fig. 3.5(b)). At higher currents, the on-state dominates (Fig. 3.5(c)) until the pulses are better described as short drop-outs from a high-amplitude state (Fig. 3.5(d), (e)). The

pulsations disappear after I = 910 mA and the laser emission is stable afterwards (Fig. 3.5(f)). It is evident from the figures, that there is some variation in pulse duration (e.g. (Fig. 3.5(c-d)), i.e. there is a jitter in the width of the pulses present at all drive currents.
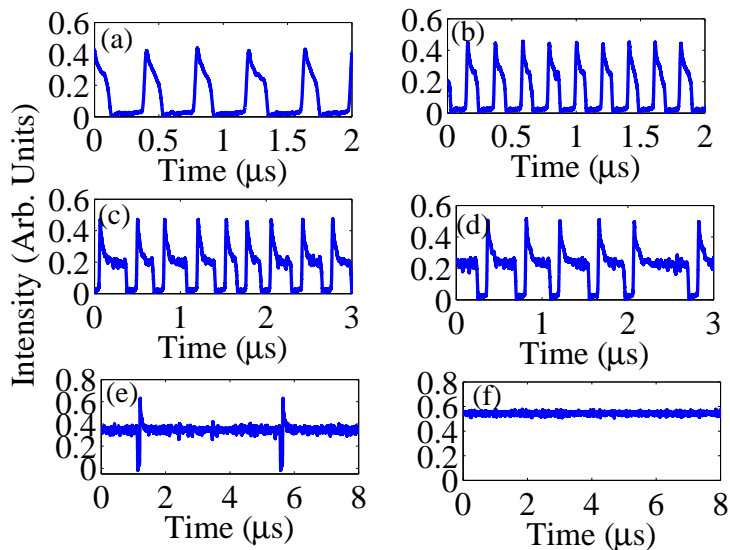
Figure 3.5: Behaviour of the oscillation for the free running laser for increasing current: (a) 803 mA, (b) 827 mA, (c) 832 mA, (d) 840 mA. (e) 872 mA (f) 910 mA.

It is possible to give a quantitative account of the frequency of this pulsations vs. drive current. The frequency of the pulsations around the threshold current of 803 mA, (Fig. 3.5(a)) is about 2.5 MHz, increases up to 5 MHz (Fig. 3.5(b)) for I = 827 mA to decreases again about 2 MHz at 840 mA (Fig. 3.5(d)) and less than 0.5 MHz for I = 872 mA (Fig. 3.5(e)).

The characteristics of the dynamics can be also illustrated by histograms of the intensity amplitudes for different current levels (Fig. 3.6). Fig. 3.6(a) is obtained at I = 803 mA and demonstrates that the distribution of amplitudes is more concentrated around the base of the pulse, reflecting a spike-like behavior of the pulses. The fact that the distribution at high amplitude is broader than at low amplitudes is due to the overshoot at the start of the pulse. Fig. 3.6(d),
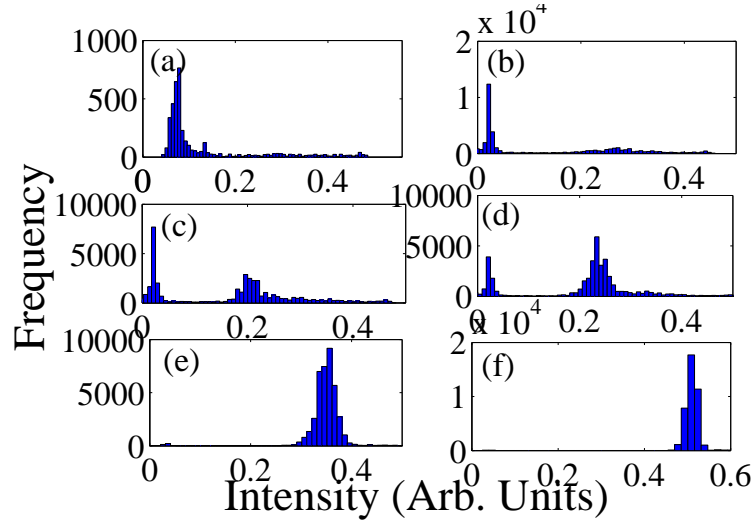
Figure 3.6: Istogram of amplitudes of the pulse for increasing current at: (a) 803 mA, (b) 827 mA, (c) 832 mA, (d) 840 mA, (e) 872 mA, (f) 910 mA.

obtained at I = 840 mA, shows a nearly evenly distributed frequency of occurrence of higher and lower intensity reflecting the approximately 50% duty cycle. For higher current, Fig. 3.6(e-f), there is a strong prevalence for the high amplitude state with only some drops in power.

The characteristics of the dynamics can be also illustrated by histograms of the time between pulses for different current levels (Fig. 3.7(e-f)). Fig. 3.7(a) is obtained at the laser threshold, I = 760 mA, and demonstrates a symmetric distribution of interpulse times with a mean around 0.35 μs. The width of the distribution is about 0.03 μs (HWHM) and corresponds to a jitter of the pulses. Increasing the current, the mean moves to 0.2 μs (Fig. 3.7(b), I = 790 mA) and the distribution narrows. For even higher current, the distributions become not only broader again, but also asymmetric (Fig. 3.7(c)-(f)). This means that the dynamics is most regular in the vicinity of the 50% duty cycle region and acquires more stochastic components afterwards. The resulting variation in pulse duration is clearly visible. Fig. 3.7(d) extends to 20 μs, i.e., there can be very rare events.
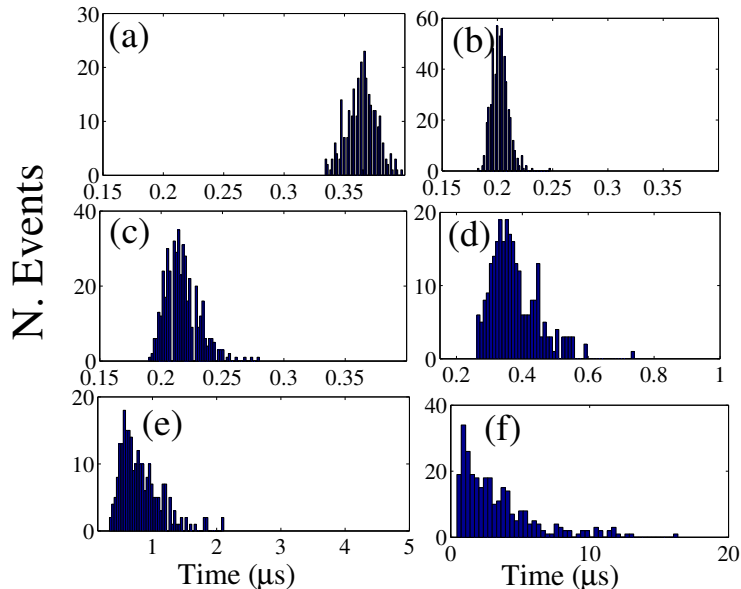
Figure 3.7: Interpulse time histogram of the pulse for increasing current at: (a) 803 mA, (b) 827 mA, (c) 832 mA, (d) 840 mA, (e) 872 mA, (f) 870 mA.

3.2.3 Pulsations in feedback operation

The laser with feedback also shows pulsations and therefore measurement have been taken to characterize the range, the shape and the frequency behavior of these oscillations following the setup of Fig. 3.1.

Fig. 3.8 show the LI-curve for the horizontal polarization component at different wavelength, from $\lambda = 1195$ nm to $\lambda = 1255$ nm. Tuning the wavelength from $\lambda = 1195$ nm to $\lambda = 1230$ nm, the threshold current decreases from $I = 780$ mA to $I = 550$ mA. Then it increases from $I = 550$ mA to $I = 720$ mA from $\lambda = 1230$ nm to $\lambda = 1255$ nm.

The shape of the LI curves varies strongly with emission wavelength. From $\lambda = 1195$ nm to $\lambda = 1220$ nm there is an abrupt switch-on of the laser at threshold that continue increasing the wavelength until around the gain peak. This switch-on decreases in amplitude with increasing wavelength. After that, Fig. 3.8, there is a continuous switch-on similar as in the free running laser. All the curve change slope, both the continuous and the abrupt ones, and a kink indicates when the laser becomes stable. Fig. 3.9 shows instead the LI-curve
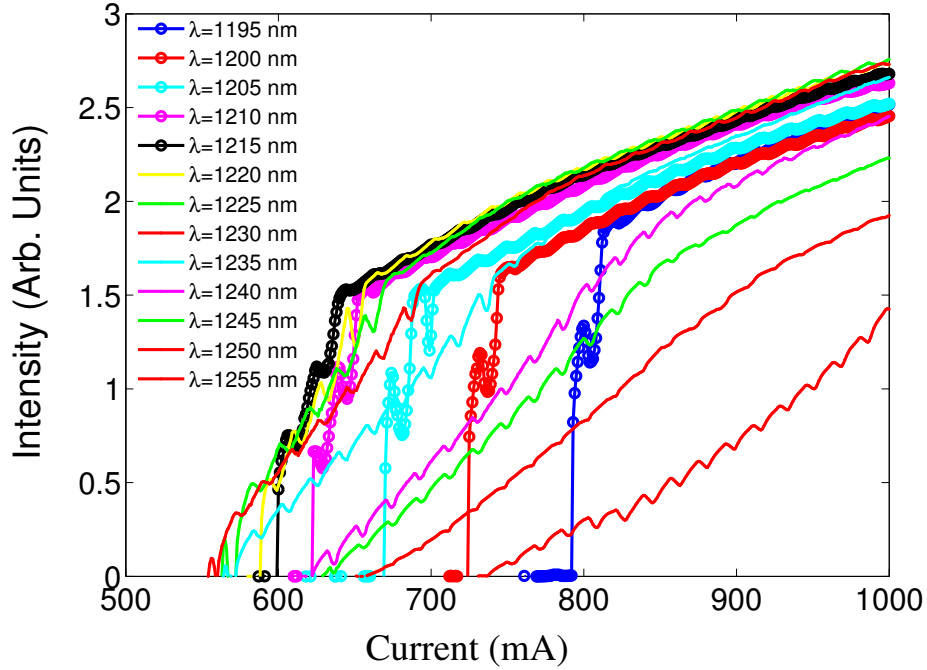
Figure 3.8: LI-curves for horizontal polarization component different wavelengths.

for the vertical polarization taken in the other arm of the setup, Fig. 3.1. The vertical component of the polarization is 10 times lower than the horizontal one. The ripple in the LI-curves are due to the Wollaston polarized present in the setup. Indeed the repetition of these ripple corresponds to the length of th Wollaston polarizer.

The behavior in threshold is the same as the horizontal one, but differently to the other curve there is a shoulder where the amplitude decreases for certain current to increase again at higher current.

The shape of the pulsations is similar to the free running laser, Fig. 3.5: short pulses from an off-state evolve towards a 50% duty cycle, then the on-phases become longer until the laser is stable at high currents. The frequency behavior of the laser with feedback has been analyzed at different temperatures. Fig. 3.10(a) shows how the frequency of the lasers in feedback changes for increasing current at different temperature.

The behavior in shape is similar to the free running lasers, in a sense that the frequency increases with current, reach a Plateau, in this case more wide
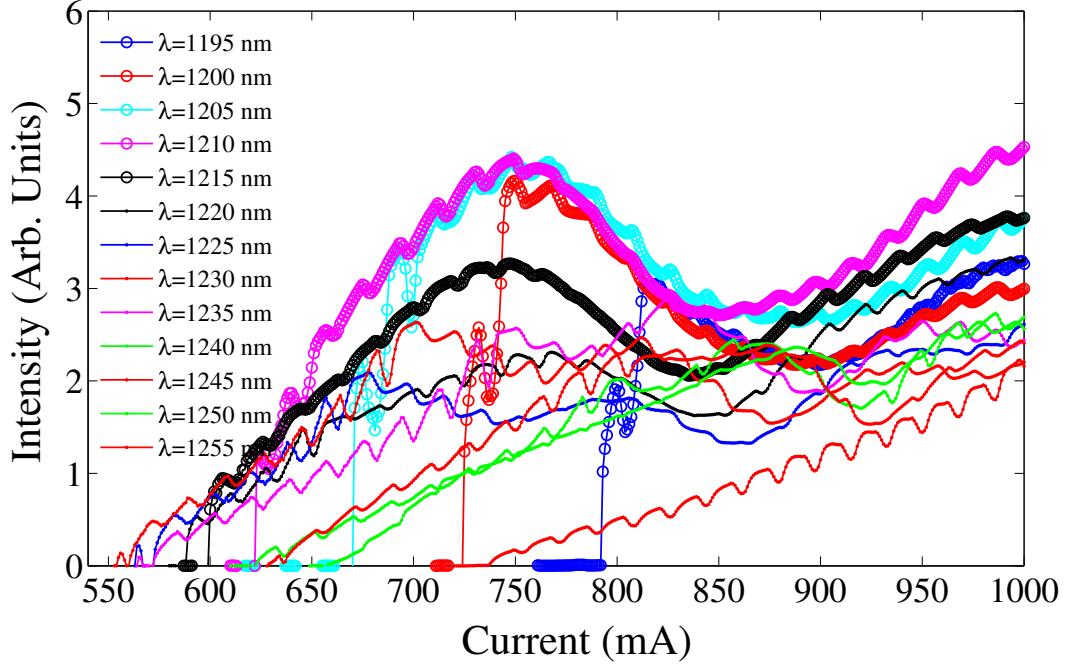
Figure 3.9: LI-curves for vertical polarization at different wavelength.

compared to the free running laser, and then decreases again at higher current.

The pulsations start at a frequency of 1 MHz at 7.5 °C to increase to 1.6 MHz and then decrease again to 0.4 MHz where they disappear.

Changing the temperature it turns out that this frequency becomes lower, Fig. 3.10(a), and the starting of the oscillation appear at higher current due to the shifting of the threshold of the laser with temperature.

Fig. 3.10(b) shows the range of the oscillation for different wavelengths available by tuning the diffraction grating from $\lambda = 1195$ nm to $\lambda = 1250$ nm. Between $\lambda = 1195$ nm and $\lambda = 1220$ nm the range where the oscillation are present is quite small, around 40 mA, then it increases to around 100 mA around the gain peak to increase again up to 200 mA for some higher wavelength. This range is for both polarizations of the diode.
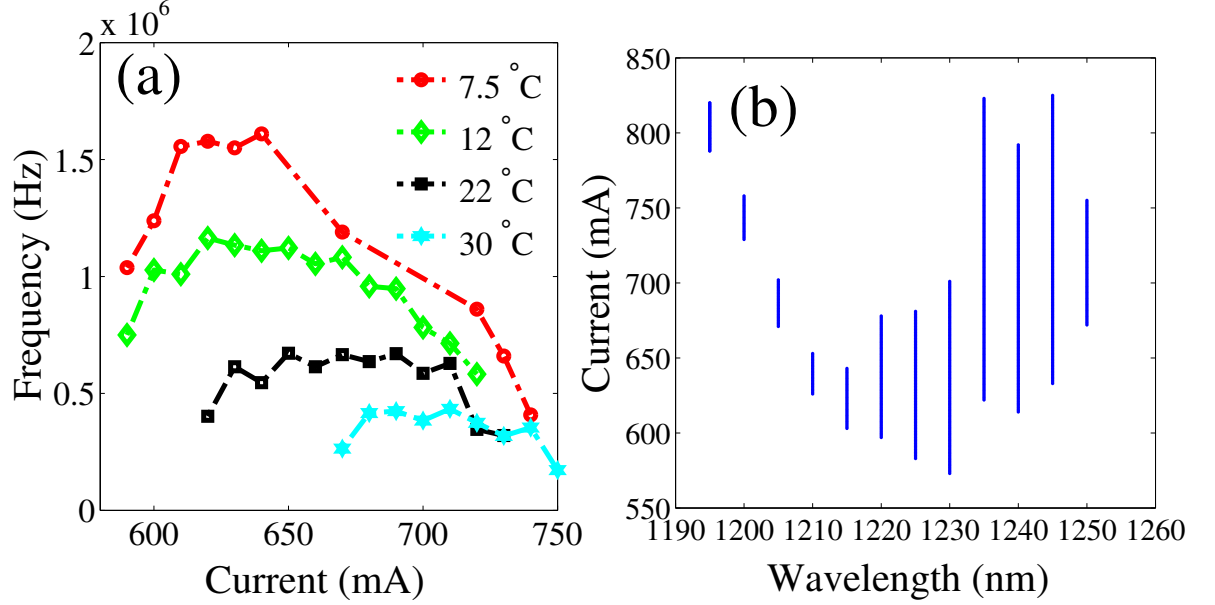
Figure 3.10: (a) Frequency behavior of the laser with feedback for increasing current at different temperatures. (b) Oscillations range in dependence of wavelength.

3.2.4 Bistability behavior

Optical bistability also take place in the diode thought no saturable section is present. The measurement are been taken scanning up and down the current of the laser with a step of 0.1 mA, the resolution of our current driver. The time between each current step is set to 2 second. The time-averaged LI curves differ strongly below the wavelength of minimal threshold of $\lambda = 1225$ nm and above.

At $\lambda = 1195$ nm, Fig. 3.11(a), there is bistability at laser threshold with a pronounced hysteresis loop. Afterwards, the average intensity increases linearly. At a kink of about I = 780 mA the slope of the LI curve changes and the laser becomes stable. Increasing the emission wavelength, the width of the hysteresis loop becomes smaller but an abrupt transition is still present up to $\lambda = 1221$ nm, Fig. 3.11(b). Fig. 3.11(c) refers to $\lambda = 1240$ nm where there is no sign of bistability and the laser threshold is continuous.
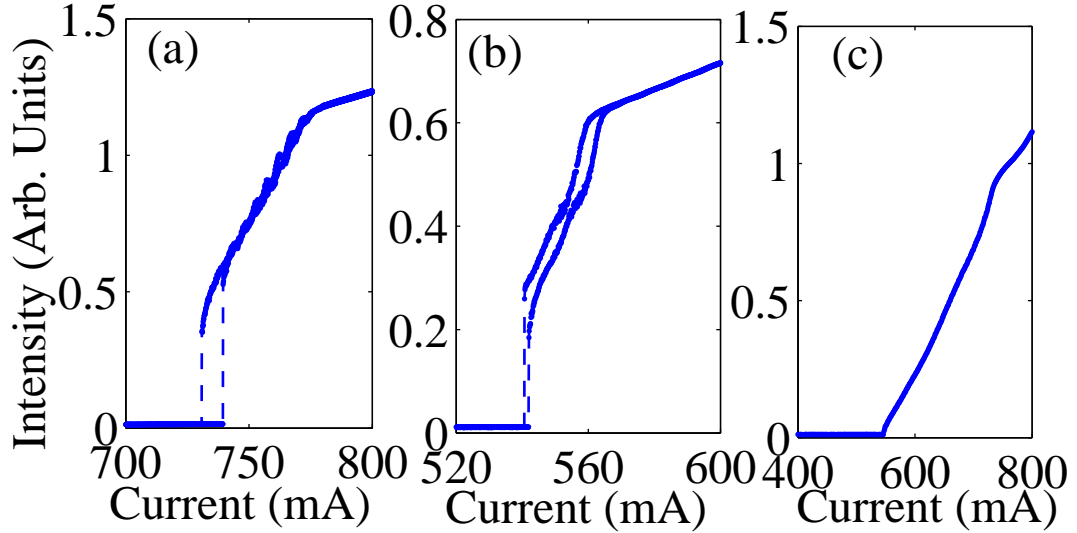
Figure 3.11: Bistability curve: (a) $\lambda = 1195$ nm, (b) gain peak, $\lambda = 1221$ nm, (c) $\lambda = 1240$ nm.

Fig. 3.11(a-b) shows also ripple in the LI curve just above the curve became linear not present for the free running lasers and at wavelength above the gain peak. The repetition of these ripple is of 5 mA for $\lambda = 1195$ nm, but not present for $\lambda = 1221$ nm where also after the switch on there is no overlap between the two side of the LI curve.

3.2.5 Preliminary interpretation of the pulsations and bistability

We note that we did not observe indications for higher QD state lasing, i.e. Fig. 3.2, as in [111] and the frequency of self-pulsing that we observe is in the MHz instead of the GHz range.

The slow time scale of these oscillations indicates that these are opto-thermal pulsations. Opto-thermal pulsation are a common scenario in broad area semiconductor quantum well optical amplifiers though at slightly slower time scales of kHz to tens of kHz [63; 112].

The described phenomenology, reported in the previous section, of pulsing

from low-amplitude state vs. 50% duty cycle to drop-outs from a high-amplitude state is found nearly identically in both systems. In the amplifier, the scenario can be dynamically interpreted within the Van Der Pol–Fitzugh–Nagumo model of interaction of dynamics at two very different time scales. In physical terms, there is a competition between two frequencies/resonances, e.g. in a laser with injection the frequency of the injected light and the cavity resonance of the slave. Initially they might be in resonance but if then amplification sets in, the slave cools due to the reduction in carrier density due to stimulated emission, its resonance shifts and interaction is lost. Then the carrier density is high again and the laser heats until it is in resonance again and a new pulse can start. The different time scales of thermal heating/cooling and stimulated emission/carrier injection lead then to relaxation oscillation-like pulsations. The same might happen in an experiment with frequency-selective feedback into a single-longitudinal mode vertical-cavity surface-emitting laser (VCSEL) where the role of the injection frequency is played by the center frequency of the grating [119].

Optical bistability in quantum dot lasers is usually associated with two-section laser structures where one section is actively pumped while the other acts as a saturable absorber [107; 120]. In two-section diode lasers, the ability to separately control the gain and absorbing regions can lead to various forms of optical bistability. In particular, these lasers can exhibit power bistability when the current applied to the gain section is swept [107]. Wavelength bistability has been more difficult to achieve but has been observed in continuous-wave, two-section distributed feedback (DFB) diode lasers [121]. The bistable operation has important applications in optical switching and modulation [122].

Frequency-selective feedback is known also to support bistability at lasing onset in bulk and quantum well lasers [123]. In contrary to [124] the origin of the bistability behavior is unclear, maybe can be due to saturable absorption in the excited state.

3.3   Time resolved spectra

The difference between our case and the previous cited literature [63; 111; 112] is the fact that in our case these oscillations appear also in the free running

lasers. This indicates that the laser itself provides a mechanism able to generate oscillations in the MHz range.

This and the fact that one is interested in a direct proof for a transient temperature shift during the pulse motivates an investigation of the optical spectra, especially time-resolved ones, developed in the following section.

3.3.1 Experimental Setup

The experimental setup is illustrated in Fig. 3.12.
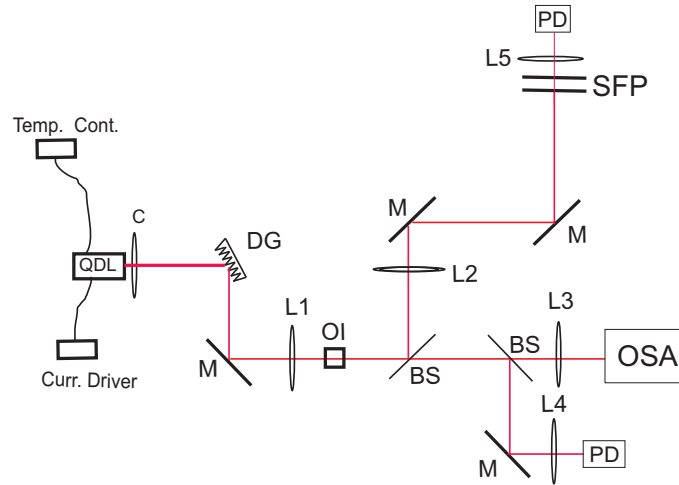
Figure 3.12: Experimental setup: quantum dot laser (QDL), aspheric collimator (C) (f = 3.1 mm), diffraction grating (DG), mirror (M), L1 (f = 100 mm), optical isolator (OI), beam splitter (BS), L2 (f = 250 mm), scanning Fabry Perot interferometer (SFP), L3 (f = 35 mm), L4 (f = 50 mm), L5 (f = 50 mm), optical spectrum analyzer (OSA), photo diode (PD).

After the external cavity, there are two lenses L1, L2 for beam shaping and an optical isolator (OI) to prevent feedback from the detection part. Two InGaAs fast detector (Thorlabs PDA255) with an active area of 1 mm and bandwidth of 50 MHz are used to monitor the dynamics of the total intensity and the spectrally resolved intensity after the scanning Fabry-Perot interferometer (SFP). The optical spectrum is also monitored by a commercial fiber coupled optical spectrum analyzer (Agilent 86140) with a nominal resolution of 0.07 nm. The plane-plane

scanning Fabry-Perot interferometer (SFP) has a free spectral range of 1.95 nm (390 GHz) and a finesse of about 500-600.

3.3.2 Time averaged spectra

Fig. 3.13 shows standard time-averaged spectra (i.e. the sweeping time of the SFP is much longer than the time scale of pulsations) around the gain peak ($\lambda = 1220$ nm) for two cases, both with feedback, when the laser is not oscillating, upper part (a), and when the laser exhibits oscillations, lower one (b). The time averaged
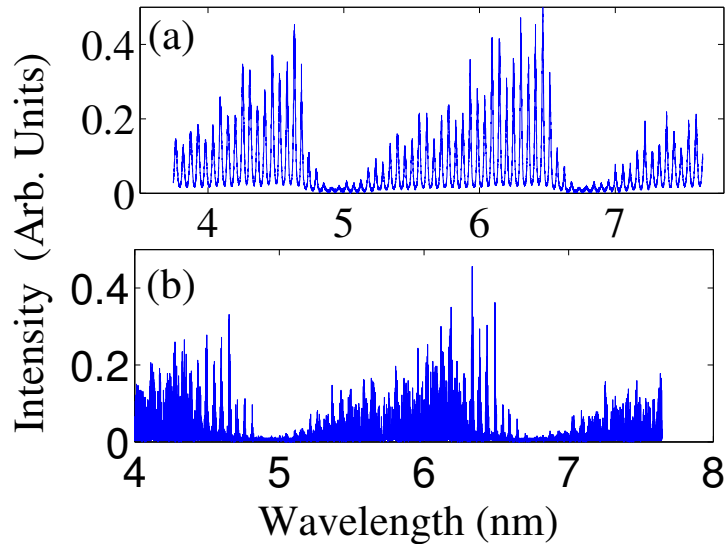
Figure 3.13: Time-averaged spectra for two relevant currents: (a) laser stable at I = 584 mA, (b) laser oscillating at I = 548 mA. The wavelength scale is only relative, the free spectral range of the analyzing SFP is 1.95 nm, i.e. the repetition of modes is a detection artifact.

spectrum is characterized by multi-longitudinal mode emission with an envelope width slightly increasing with current being 4-5 nm in the interesting range. At the transition between self-pulsing and stable operation there is no noticeable effect on the envelope in the time averaged spectrum but the linewidth of the individual longitudinal modes decreases.

In both cases, the laser is strongly multi-mode covering about 1.5 nm. The modal envelope is increasing from lower to higher wavelengths. The line width of

an individual longitudinal mode is about 0.6 GHz for stable emission. Instead, when pulsating the average linewidth is larger (Fig. 3.13b), about 5.6 GHz, which might be due to modes jittering.

3.3.3   Time resolved spectra

One way to check for temperature changes is to look at spectral shifts, however typical optical spectrum analyzer average over milliseconds or more, i.e. much longer than an oscillation period.
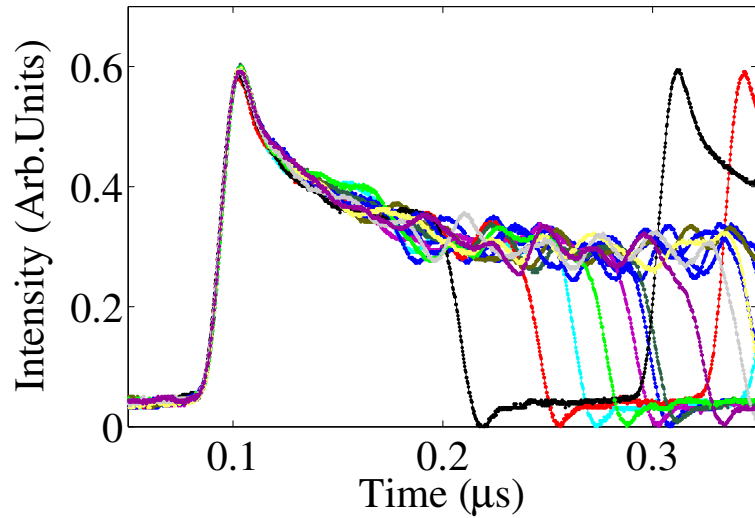
Figure 3.14: Superpositions of pulse shapes obtained by a non-frequency selective monitor illustrating the timing jitter. The results are reliable in the first 0.2 μs, i.e. the interesting interval during the overshoot, whereas the jitter of pulse duration affects the reproducibility later on.

This is investigated in more detail in frequency resolved measurements where the mirror separation in a plano-planar Fabry-Perot cavity is changed stepwise via a computer and the pulse shape after the Fabry-Perot at that wavelength taken by a digital oscilloscope. The oscilloscope is triggered on the steep front edge of the pulse which is reproducible from event to event (see Fig. 3.14) so that a time-resolved spectrum can be reconstructed).

Following [125], we record the time-resolved spectrum for all frequencies inside a free spectral range and superimpose the data recorded for every frequency.

This is done by scanning the piezoelectric translators of the SFP by a computer controlled voltage slowly (stepwise) while we record with a fast detector the signal transmitted by the SFP. The diode drive current is kept fixed during the experiment. To maintain a stable signal on the scope we trigger on the pulse read out by the other fast detector. In our case 0.47 V correspond to a free spectral range of 1.95 nm. The scan covers 0.8 V with a resolution of 1 mV steps leading to almost two FSR with a nominal wavelength resolution of 0.0041 nm.
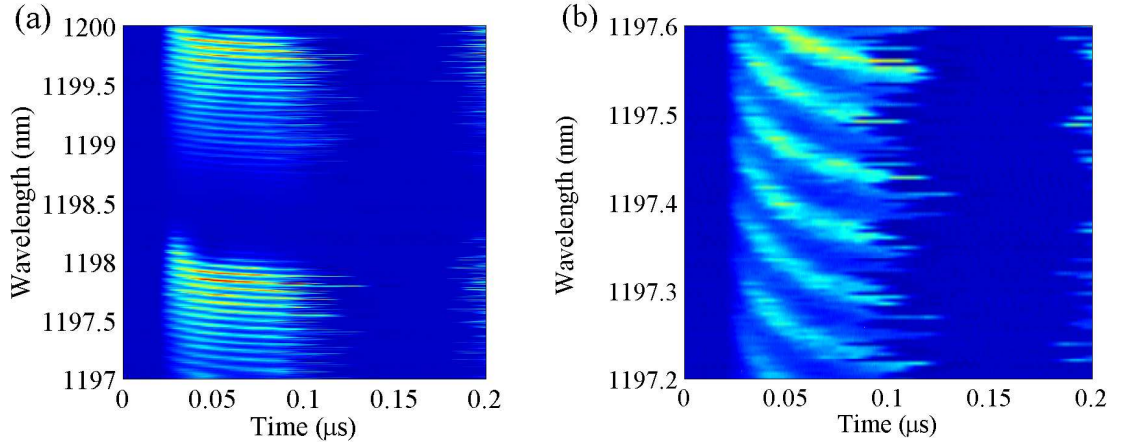
Figure 3.15: Time-resolved spectrum for (a) $\lambda = 1197$ nm, I $= 724$ mA, (b) Zoom of (a) from $\lambda = 1197.2$ nm to $\lambda = 1197.4$ nm.

Fig. 3.15 shows the time-resolved spectra for two different wavelength achievable tuning the diffraction grating. Fig. 3.15(a) is for $\lambda = 1197$ nm at I $= 724$ mA, almost at the low-wavelength edge of the tuning range. One can see that the trajectory of each longitudinal mode is initially curved (blue-shifting) until it remains essentially constant for the remainder of the pulse. This blue-shift covers about 0.13 nm and might be due to radiative cooling. This would fit the interpretation in the amplifier systems [126] where it wasn't demonstrated experimentally explicitly though. In addition, the envelope of lasing also blue-shifts with the most reddish modes being excited and dying first.

Fig. 3.16(a) is for $\lambda = 1220$ nm, around the gain peak, at I $= 548$ mA. Again the envelope blue-shifts in the initial phase but then swings back towards the red. Within each cavity mode there is a blue-shift of 0.11 nm.

Fig. 3.16(b) is for $\lambda = 1240$ nm at I $= 600$ mA. In this case, the lasing starts at low wavelengths and then the envelope red-shifts. Within each cavity mode there is a blue-shift of 0.06 nm.
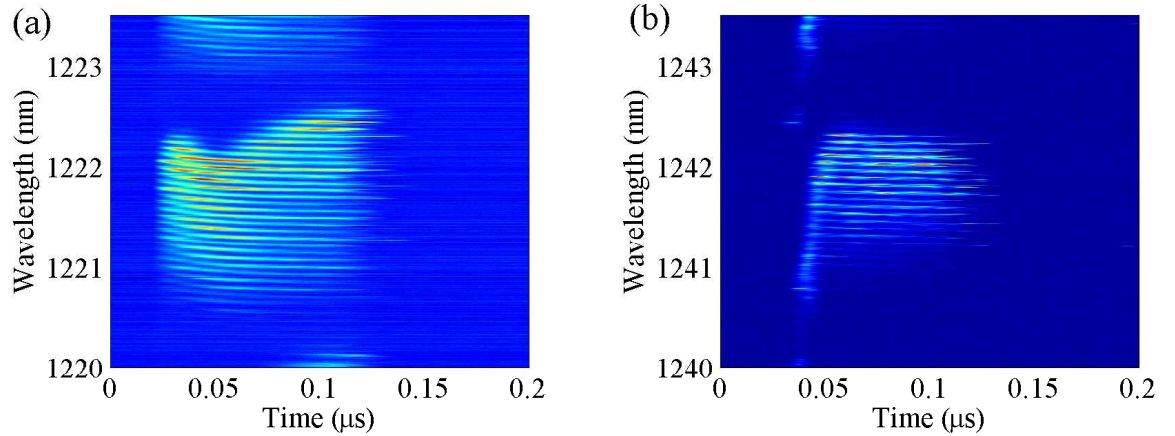
Figure 3.16: Time resolved spectrum for (a) $\lambda = 1221$ nm at I $= 548$ mA, (b) $\lambda = 1240$ nm, I $= 600$ mA.
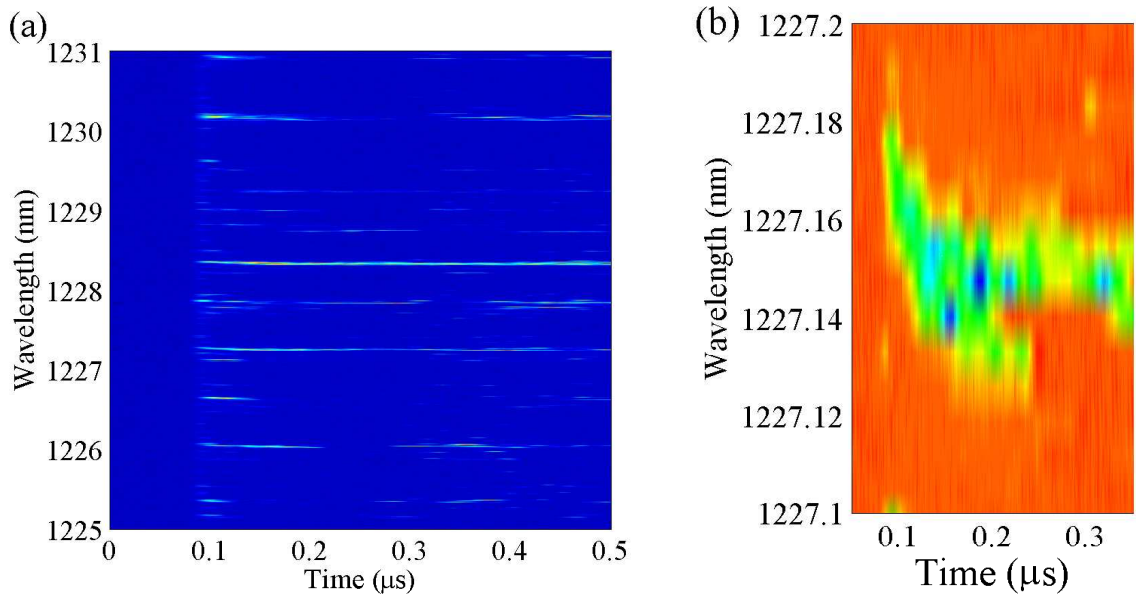
Figure 3.17: Time resolved spectrum for (a) free running laser $\lambda = 1225$ nm at I $= 831$ mA the FSR of the analyzing SFP was increased to 5.7 nm, (b) Zoom in of (a) from $\lambda = 1227.1$ nm to $\lambda = 1227.2$ nm.

Fig 3.17(a) shows instead the time-resolved spectrum for the free running laser at a typical current. In this case there is a very weak blue-shift of 0.02 nm for each longitudinal mode but the envelope does not shift very much. The fact that the diagram is quite jagged for longer times is related to the fact that there is a larger dispersion of pulse length in the free-running laser than in the laser with feedback which makes the sampling technique less reliable further away from the trigger point.

During the first 0.1 μs of the pulse there is a blue- shift of about 0.03 nm for each longitudinal mode, Fig 3.17(b). A blue shift is consistent with radiative cooling because after switch-on stimulated emission leads to a reduction of carriers and hence dissipated heat and hence supports the notion of a thermal effect.

3.3.4 Analysis and interpretation

Switching between longitudinal modes was discussed in [127; 128; 129; 130] for quantum well lasers and in [131] for quantum dot lasers. An important conclusion was that longitudinal mode switching is not a merely stochastic process but follows a quite deterministic switching sequence influenced by nonlinearities. A preference for a switching sequence from blue to red modes was related to the breaking of the symmetry of four-wave mixing processes by a nonzero α-factor. The α-factor or linewidth-enhancement factor describes phase-amplitude coupling in semiconductors and is positive for quantum well samples [23].

A positive α-factor was found to be consistent with the blue-to-red switching sequence observed [129; 130]. The 3D quantum confinement of ideal QD should lead to a 'quasi-atomic' behavior with a delta function-like density of states. A symmetric gain spectrum should have zero phase-amplitude coupling or linewidth enhancement factor at gain maximum, positive for lower frequencies and negative for higher frequencies. The different shift of the longitudinal modes during the pulses observed is in qualitative agreement with this expectation: On gain maximum, the free-running as well as the laser with feedback do not show much of a shift consistent with a zero or small α-factor. The detuned emission under frequency-selective feedback shows the same tendency as the quantum well

devices for lower frequencies (positive α-factor) and the opposite for higher frequencies (negative α-factor). The size and sign of the α-factor is very important for feedback and filamentation instabilities. Indeed, a reduced (or even negative) α-factor and a reduced tendency to beam filamentation was observed in many QD samples, at least under some operating conditions [26; 27; 132; 133; 134; 135]. The real susceptibility of QD are more complicated than the one of a two-level atom due to contributions from the wetting layer, higher QD states and inhomogeneous broadening (e.g. [136]), though the possibility of a negative $\alpha-$factor under gain conditions can survive. The current observation of a qualitative agreement with the two-level expectation seems to be interesting though it should be cautioned that the argument is quite indirect.

Finally, the fact that each longitudinal mode blue-shifts at the beginning of the pulse hints to a detuning-independent effect like a temperature shift. Indeed, it is consistent with radiative cooling, which might trigger the thermal relaxation oscillations.

3.4 Waveguiding properties

As seen in the previous section there is no obvious mechanism of a competition between resonance conditions. Also discussion with Innolume assure us that the device used for the previous experiment is only shallow edged.

This reason lead to a theoretical and experimental investigation of how the device behave in the center and wings. Differences between the dynamics in device center and beam wings might indicate thermal lensing or a wave guiding mechanism in maintaining this pulsations.

3.4.1 Waveguide description and simulation

The waveguide model used for the simulation is illustrated in Fig. 3.18. We use the slab geometry according to [137]. The guide is assumed to be infinite in the y direction. The structure is composed of three lossless dielectric regions: the middle layer know as slab or film. It has a thickness d and refractive index n_1. The upper and lower cladding regions, having index n_2, are semi-infinite in the

positive and negative x direction. Light propagates into the slab from left and the waveguide modes propagate in the positive z directions.
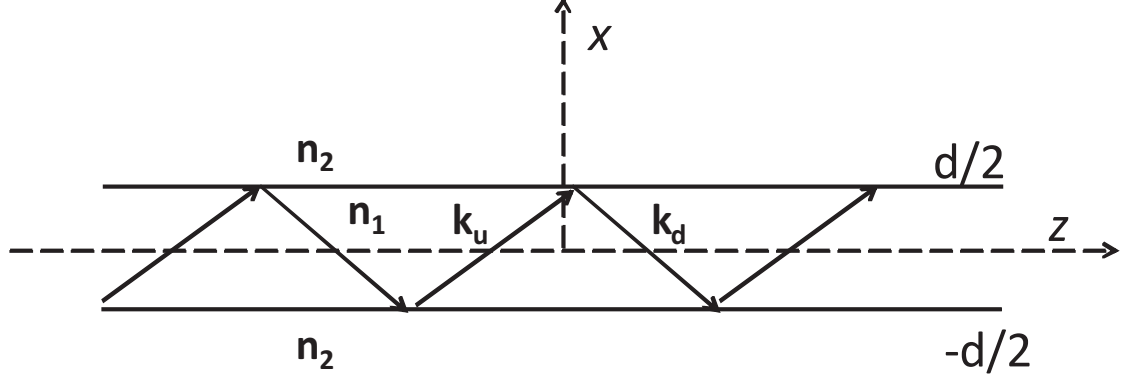
Figure 3.18: View, Symmetric slab ray geometry.

The equations that relate the attenuation coefficient and the projection of k long the x direction are given by:

$$\gamma_2 = (\beta^2 - n_2^2 k_0^2)^{1/2} \tag{3.1}$$

$$k_{x1} = (n_1^2 k_0^2 - \beta^2)^{1/2} \tag{3.2}$$

From the previous equation we have:

$$(k_{x1}d)^2 + (\gamma_2 d)^2 = k_0^2 d^2 (n_1^2 - n_2^2) \tag{3.3}$$

Plotted with coordinate $k_{x1}d$ and $\gamma_2 d$ this is the equation of a circle of radius $R = k_0 d (n_1^2 - n_2^2)^{1/2}$.

Solving for $\gamma_2 d$ we have;

$$\gamma_2 d = d[k_0^2(n_1^2 - n_2^2) - k_{x1}^2] =$$

$$k_{x1}d \tan(k_{x1}d/2) \text{ m} = 0, 2, 4..$$

$$= -k_{x1}d \tan(k_{x1}d/2) \text{ m} = 1, 3, 5..$$

We numerically solve the previous equation with the parameter set in the Table 1.1.

Table 3.1: Value of the parameter used for the simulation (Courtesy of Innolume GmbH).

Parameter	name	Value
Thickness	d	4.6 μm
Wavelength	λ	1.225 μm
Core effective refractive index	n_1	3.396
Cladding effective refractive index	n_2	3.395
V parameter	V	1.9442
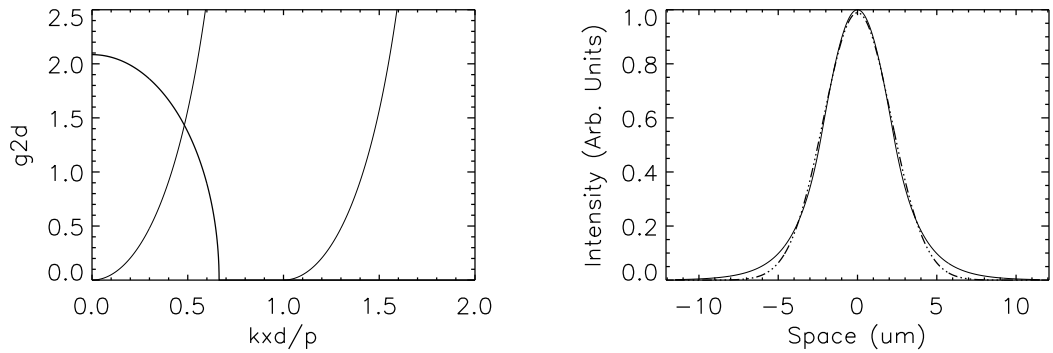
Figure 3.19: Left: Plot of a graphical solution for TE mode in a symmetric slab waveguide, showing the single mode case, right: Mode profile of the intensity and Gaussian fit

The result of the simulation are given in Fig. 3.19. The left side of Fig. 3.19 shows that with the parameter of Table 1.1., the waveguide is single mode.

The right-side of Fig. 3.19 shows the profile of the waveguide mode. The mode is Gaussian in good approximation, see fitted dotted line, with a mode size of 4.54 μm.

Varying the effective index by $\pm 10^{-4}$ we have the value reported in the table 3.2:

This rather pronounced change in the mode profile motivates an investigation of the beam profiles discussed in the next section.

Table 3.2: Value of mode profile, size and V parameter for different Δn

Effective Δn	mode (Gauss. Fit) μm	Size ($1/e^2$-point) μm	V parameter
0.9997	5.4276	5.92255	1.62664
0.9998	5.05994	5.46714	1.73895
0.99985	4.90813	5.27956	1.79247
0.9999	4.77256	5.11064	1.84458
0.001	4.54238	4.82544	1.9442
0.0011	4.35241	4.58854	2.03936
0.0012	4.2702	4.48503	2.08493
0.0015	4.39073	4.19399	2.12989

3.4.2 Experimental Setup
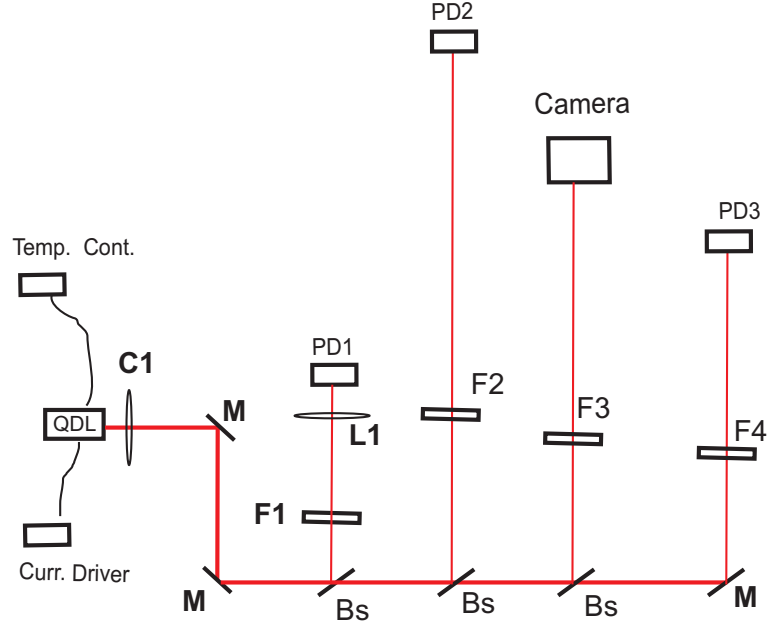
Figure 3.20: Experimental setup: quantum dot laser (QDL), aspheric collimator (C1) (f = 3.1 mm), mirror (M), L1 (f = 50 mm), beam splitter (BS), optical spectrum analyzer (OSA), filter (F1, F2, F3, F4), photo diode (PD1, PD2, PD3).

The experimental setup of Fig. 3.20 is made for looking simultaneously at the beam in different parts. We use three equal photodiodes (Thorlabs PDA255, bandwidth of 50 MHz) for this experiment. With the first photodiode (PD1)

we monitor the total intensity of the QDL diode and then also simultaneously we monitor the beam center (PD2) and beam side (PD3). Also the intensity distribution at the exit facet of the diode is imaged into an InGaAs camera at a distance of $d = 1660$ mm. The magnification of the system is of 535.5.

3.4.3 Results

Fig. 3.21 shows the beam radius ($1/e^2$-point of intensity along the horizontal slow) axis of the QDL as function of current. The profiles are Gaussian in good approximation (see inset). From the results it is possible to infer that the beam width decreases with increasing current. Accounting for the magnification of the system one infers for the beam sizes in the laser that it drops from 5.3 μm at I = 820 mA to 4.4 μm at I = 920 mA.
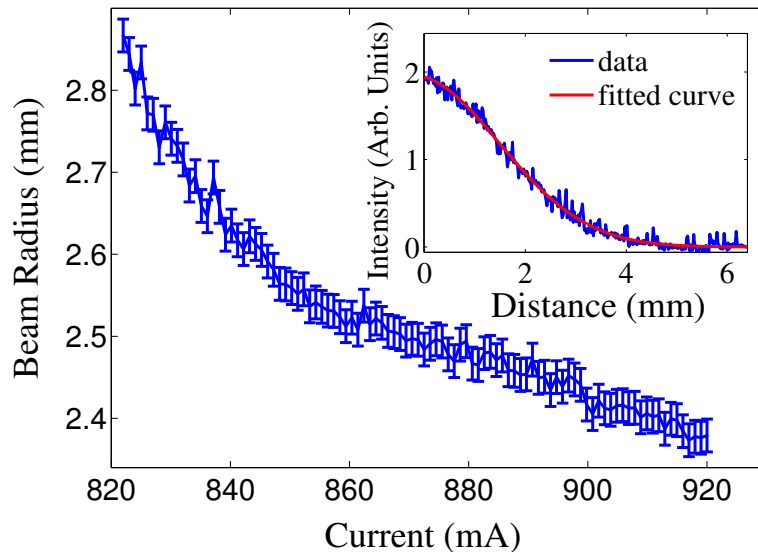
Figure 3.21: Time averaged horizontal beam radius as function of current. The inset shows the profile (blue line) with a Gaussian fit (red line) at I = 834 mA. Laser threshold I = 800 mA.

In contrast, the beam size of the vertical profile (fast axis) is much more constant as shown in Fig. 3.22. The inset of Fig. 3.22 show the beam size long the fast axis at I = 900 mA, in blue curve, and the Gaussian fit (red curve). The shoulder on the Gaussian profile is due to the large divergence of the beam.
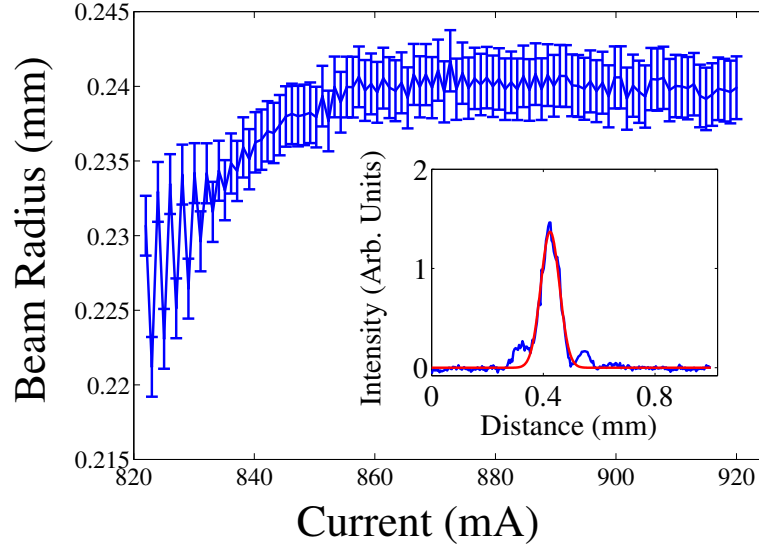
Figure 3.22: Time averaged vertical beam radius as function of current. The inset shows the profile (blue line) with a Gaussian fit (red line) at $I = 900$ mA.

In this setup is possible also to look on how the shapes of the pulse differ in the beam center and in the wings. Fig. 3.23(a) illustrates that the detectors yield essentially the same signals if both are moved into the beam center. This signal follows closely the one obtained for the total power in a third arm. In contrast, if the second detector is moved 5 mm off center, the initial overshoot disappears and the pulse is essentially rectangularly shaped (Fig. 3.23(b)-blue line). Fig. 3.23(c) shows quantitatively the ratio of the height of the initial overshoot to the pulse amplitude just before switch-down. The ratio drops to 1 rather abruptly after 4 mm, i.e. about 1.5 times the beam radius. From that is possible to infer that initially the output is more localized in the center compatible with a stronger waveguiding.

71
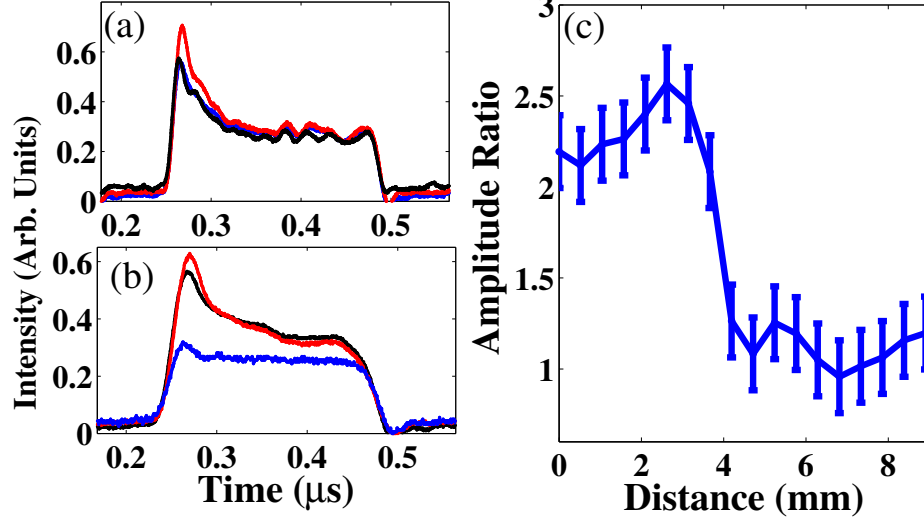
Figure 3.23: Pulse shape at different locations I = 822 mA: (a) Red and blue curves monitor the beam center, the black curve is obtained from focusing the whole beam on the detector with a lens. (b) As in (a) but blue curve obtained now 5 mm off beam center. (c) Evolution of ratio between initial overshoot and pulse amplitude before switch-off as function of distance from beam center.

3.4.4 Analysis and Interpretation

As indicated before, the time scale and the bifurcation scenario suggest that these are opto-thermal pulsations similar to the ones reported in quantum well amplifiers [63] but there is no obvious mechanism of a competition between the cavity resonance condition and another frequency-selected process like in the situations discussed in the introduction. Instead, the experiments support a new mechanism for opto-thermal pulsations based on waveguiding. Due to the shallow etching, the mode is not strongly confined but the confinement – and hence the modal gain – is enhanced by the refractive index increase in the ridge due to Joule heating. After switch-on, radiative cooling leads to a reduction in confinement and the laser switched down again. Then the process is started again by heating. At some point, the average heat load is high enough to sustain cw lasing. Assuming the one-dimensional theory for simple rectangularly-shaped dielectric waveguides

this is compatible with a change of the effective index difference between core and cladding of $\pm 1.5 \times 10^{-4}$ around the estimated effective index difference of 0.001. Since the thermal change of the refractive index of GaAs is about 2×10^{-4}/K, it seems very feasible that a thermal lens induced by the Joule heating of the current is providing this increased lateral confinement of the mode in the waveguide. The relationship between temporal (τ) and spatial (s) scales for diffusive processes (diffusion constant D) is roughly given by $\tau = s^2/D$ (see also [138] for specific geometries). Taking the width of the ridge-waveguide as a typical length scale, $s = 5 \ \mu$m, and a thermal diffusivity of GaAs of $D = 2.5 \times 10^{-5} - 1.3 \times 10^{-4} \ \text{m}^2/\text{s}$ [139; 140], one obtains $\tau = 0.2 - 1 \ \mu$s in good agreement with observation. In support, we established that devices with a slightly deeper etching (discussed in Chapter 2, section 2.4.), and hence better confinement do not show this instability.

Chapter 4

Numerical simulations

In this chapter, we are addressing the room temperature, cw nonlinear optics of QDs. Because of the strong coupling of QDs to the semiconductor matrix they are incorporated in, QDs are more complex than 'simple' atoms and we are adopting a model including QD and wetting layer (WL) dynamics with the basic coupling mechanisms using phenomenological rate constants. Another complication comes from the fact that QD spectra correspond to a 'Voigt'-profile where neither the homogeneous nor the inhomogeneous broadening is strongly dominating. Hence, we will mainly rely on numerical simulations. It turns out that indeed the saturation behavior is in between the expectations for the two limiting cases.

4.0.5 Background information

A convenient way to characterize the nonlinear refractive index is measuring the *lensing* incurred by a spatially varying input beam by the z-scan technique [141] or variants thereof, as done, e.g., for atomic vapors [142]. Measuring the self-lensing provides also an alternative approach to the important problem of characterizing phase-amplitude coupling in QD [132; 133]. Due to their symmetric, atom-like gain spectrum, QD should have zero phase-amplitude coupling or linewidth enhancement factor (or α-factor, [23]) at gain maximum and hence a reduced tendency to instabilities compared to quantum well and bulk devices. Indeed, a reduced α-factor and a reduced tendency to beam filamentation was observed in

many QD samples, at least under some operating conditions [26; 27; 134; 135]. Characterizing self-lensing will give a direct indication of the tendency of the system to filamentation.

4.1   Maxwell and paraxial wave equation

The Maxwell equation relate the electric field **E** and magnetic **H** are:

$$\vec{\nabla} \times \vec{\mathbf{E}} = -\frac{\partial}{\partial t}\vec{H} \tag{4.1}$$

$$\vec{\nabla} \times \vec{\mathbf{H}} = \mu_0(\vec{j} + \epsilon_0\frac{\partial}{\partial t}\vec{D}) \tag{4.2}$$

$$\vec{\nabla} \cdot \vec{\mathbf{H}} = 0 \tag{4.3}$$

$$\vec{\nabla} \cdot \vec{\mathbf{E}} = \frac{\rho}{\epsilon_0} \tag{4.4}$$

where ρ is the free charge density and $\vec{j}$ the current density. The electric and magnetic flux density, $\vec{\mathbf{D}}$ and $\vec{\mathbf{B}}$ are given by:

$$\vec{\mathbf{D}} = \epsilon_0\vec{\mathbf{E}} + \vec{\mathbf{P}} \tag{4.5}$$

$$\vec{\mathbf{B}} = \mu_0\vec{\mathbf{H}} + \vec{\mathbf{M}} \tag{4.6}$$

$$\tag{4.7}$$

where **P** and **M** are the electric and magnetic field polarizations, ϵ_0 and μ_0 are the permittivity and permeability in a vacuum. The propagation in a non-magnetic medium without free charges ($\mathbf{M} = \vec{j} = \rho = 0$) allows to write the previous equations in the form of the propagation equation [143; 144]:

$$\Delta\vec{\mathbf{E}} - \frac{1}{c^2}\frac{\partial^2}{\partial t^2}\vec{\mathbf{E}} = \frac{1}{\epsilon_0 c^2}\frac{\partial^2}{\partial t^2}\vec{\mathbf{P}} - \frac{1}{\epsilon_0}\vec{\nabla}(\vec{\nabla} \cdot \vec{\mathbf{P}}) \tag{4.8}$$

In the approximation $\vec{\nabla} \cdot \vec{\mathbf{P}} = -\epsilon_0\vec{\nabla} \cdot \vec{\mathbf{E}} \approx 0$ for most media and in particular linear and isotropic, the nonlinear wave equation is:

$$\Delta\vec{\mathbf{E}} - \frac{1}{c^2}\frac{\partial^2}{\partial t^2}\vec{\mathbf{E}} = \frac{1}{\epsilon_0 c^2}\frac{\partial^2}{\partial t^2}\vec{\mathbf{P}} \tag{4.9}$$

In the following, a well defined linear polarization state is assumed. Electric field and polarization summed with Fourier component with complex amplitude $E_0(\omega_0)$ and $P_0(\omega_0)$ are described by:

$$E = \frac{1}{2}(E_0 e^{-i\omega_0 t + ik_0 n_b z} + cc.) \tag{4.10}$$

$$P = \frac{1}{2}(P_0 e^{-i\omega_0 t + ik_0 n_b z} + cc.), \tag{4.11}$$

where $k_0 = \omega_0/c$. The complex envelope is assumed to be slowly varying, i.e. $E_0 = E_0(x, y, z, t)$, $P_0 = P_0(x, y, z, t)$. Polarization and electrical field are connected via the susceptibility:

$$P_0(\omega_0) = \epsilon_0 \chi(\omega_0) E_0(\omega_0). \tag{4.12}$$

In nonlinear optics, $\chi(\omega)$ depends itself on the field and might be depend also on other frequency components than ω_0, i.e. $\chi = \chi(E_0, E_1, E_2, \ldots)$ where E_i are the envelopes of all the fields present. We will limit to the frequency-degenerate, single-field case here though. In the temporal domain, the statement $P(t) = \epsilon_0 \chi E(t)$ is problematic, since it assumes an instantaneous response of the mediums. Here, it is assumed that the polarization consists of a linear background contribution and the one of the particular transition under study. The background part might be complex but the following explicit calculation address as only there is the real case.

$$P = P_b + P_{transition} = \epsilon_0 \chi_b E + P_{transition}, \tag{4.13}$$

where we will drop the 'transition' index again in the following. The refractive index of the host material is denoted by n_b and the wave number is then $k = k_0 n_b$, $n_b = 1$ corresponds to the case of propagation in a dilute atomic vapour.

In the next step, (4.10) and (4.11) are inserted into (4.9) and only the leading contributions kept (first derivatives in E_0, constant driving in P_0). Taking into account that the host medium might be dispersive, the group index n_g and the group velocity v_g enter instead of phase index and velocity.

This leads to the paraxial wave equation for pulse propagation

$$\left(\frac{\partial}{\partial z} + \frac{1}{v_g}\frac{\partial}{\partial t} + i\frac{k''}{2}\frac{\partial^2}{\partial t^2}\right)E_0 = \frac{i}{2k}\left(\Delta_\perp + \frac{\omega_0^2}{c^2}\chi(E_0)\right)E_0. \tag{4.14}$$

The term proportional to k'' describing group velocity dispersion is only relevant for pulse propagation and the paraxial wave equation applicable to beam propagation and cavity experiments is

$$\left(\frac{\partial}{\partial z} + \frac{1}{v_g}\frac{\partial}{\partial t}\right)E_0 = \frac{i}{2k}\left(\Delta_\perp + \frac{\omega_0^2}{c^2}\chi(E_0)\right)E_0. \tag{4.15}$$

Eq.(4.15) gives the important inside that absorption coefficients per unit length and per unit time can be converted into each other via the group velocity. The absorption coefficient for the field in Beer's law per unit length is:

$$\alpha = \frac{k_0}{2n_b}\mathrm{Im}\chi. \tag{4.16}$$

Note that the absorption coefficient for the intensity/energy is twice this value. Assuming that the total refractive index is $n_b + n' + in''$, the refractive index contribution due to the transition is

$$n' = \frac{1}{2n_b}\mathrm{Re}\chi \tag{4.17}$$

and

$$n'' = \frac{1}{2(n_b + n')}\mathrm{Im}\chi \approx \frac{1}{2n_b}\mathrm{Im}\chi, \tag{4.18}$$

where it is assumed that n', $n'' << 1$, which is necessary for the validity of the paraxial equation.

4.1.1 Confinement factor

Propagation in photonic devices is often characterized by the fact that the overlap between field and active medium is not perfect. This is characterized by a modal

gain (or susceptibility) or confinement factors arising from an overlap integral

$$< \chi >= \chi \frac{\int_{active} dV |E(x,y,z)|}{\int_{cavity} dV |E(x,y,z)|} = \Gamma\chi \tag{4.19}$$

The confinement factor results from a combination of transverse and longitudinal overlap and interference effects,

$$\Gamma = \Gamma_{trans}\Gamma_l\Gamma_r. \tag{4.20}$$

$$\Gamma_{trans} = \frac{\int_{-d/2}^{d/2} dy |E(y)|}{\int_{-\infty}^{\infty} dy |E(y)|}, \tag{4.21}$$

where d is the layer thickness or aperture width. Γ_{trans} is typically 1 in VCSELs and 0.03-0.01 in edge emitters with single action layer. The longitudinal confinement factor is:

$$\Gamma_l = \frac{L_A}{L} \tag{4.22}$$

takes into account that typically only a fraction L_A of the total cavity length L contains the active medium.

Γ_r takes into account that in a VCSEL the active layers are typically close to an anti-node of the field where forward and backward field interfere constructively. Hence the value is nearly 2 for a single quantum well and about 1.8 for a group of 3 quantum well (or quantum dot layers). We only concern with edge-emitting samples where $\Gamma_l = 1$, $\Gamma_r = 1$.

4.2 Optical Bloch equations

The interaction of light with a 2-level medium can be calculated by the density matrix approach, e.g. [144], see also [145]. The result is given by the following set of equation:

$$\frac{d}{dt}P_0 = i\Delta P_0 + i\frac{\mu}{\hbar}E_0\Delta N - \Gamma_2 P_0 \tag{4.23}$$

$$\frac{d}{dt}\Delta N = \frac{2i}{2^\star 2^\star \hbar}(E_0^* P_0 - E_0 P_0^*) - \Gamma_1(\Delta N - N_D) \tag{4.24}$$

where $\Delta N = N_D(\rho_{11} - \rho_{22})$ is an inversion density, N_D the density of the absorbers, μ the dipole matrix element of the transition, $\Delta = \omega_0 - \omega_a$ the detuning between laser and atomic resonance, Γ_2 the homogeneous linewidth (HWHM) in angular frequencies and Γ_1 the decay rate of the inversion.

Since in systems with strong interaction with the environment (semiconductors, atomic vapors in a buffer gas atmosphere) typically $\Gamma_2 >> \Gamma_1$, the polarization can be adiabatically eliminated. The stationary solution for the polarization is given by:

$$P_0 = i\frac{\mu}{\hbar}\frac{1}{\Gamma_2 - i\Delta}E_0\Delta N. \tag{4.25}$$

Inserting this into the equation of motion (4.24)) for the inversion gives:

$$\frac{d}{dt}\Delta N = -\frac{4\mu^2}{2^\star 2^\star \hbar^2 \Gamma_2}\Delta N \mid E_0 \mid^2 \frac{1}{1 + \bar{\Delta}^2} - \Gamma_1(\Delta N - N_D), \tag{4.26}$$

where $\bar{\Delta} = \Delta/\Gamma_2$ is a normalized detuning. The stationary solution is

$$\Delta N = \frac{N_D}{1 + \left(\frac{|E_0|}{|E_s|}\right)^2} \tag{4.27}$$

where the square of the saturation field strength is

$$|E_s|^2 = (1 + \bar{\Delta}^2)\frac{2^\star 2^\star \hbar^2 \Gamma_2 \Gamma_1}{4\mu^2} \tag{4.28}$$

The susceptibility of a two-level medium is then found as

$$\chi = \frac{\mu^2}{\hbar\epsilon_0\Gamma_2}\frac{i - \bar{\Delta}}{1 + \bar{\Delta}^2}\Delta N = \frac{\mu^2}{\hbar\epsilon_0\Gamma_2}\frac{i - \bar{\Delta}}{1 + \bar{\Delta}^2}\frac{N_D}{1 + \left(\frac{|E_0|}{|E_s|}\right)^2}. \tag{4.29}$$

It is often useful the to define a lineshape function

$$\tilde{\chi} = \frac{i - \bar{\Delta}}{1 + \bar{\Delta}^2}, \tag{4.30}$$

which gives

$$\chi = \frac{\mu^2}{\hbar\epsilon_0\Gamma_2} \tilde{\chi} \frac{N_D}{1 + \left(\frac{|E_0|}{|E_s|}\right)^2}. \tag{4.31}$$

The rate of spontaneous emission Γ_1 can be related to the dipole matrix element

$$\mu^2 = \Gamma_1 \frac{\pi c^3 \hbar\epsilon_0}{\omega_0^3 n_b}. \tag{4.32}$$

This gives the susceptibility in terms of directly measurable parameters

$$\chi = \frac{\Gamma_1}{\Gamma_2} \frac{\pi c^3}{\omega_0^3 n_b} \tilde{\chi} \frac{N_D}{1 + \left(\frac{|E_0|}{|E_s|}\right)^2}. \tag{4.33}$$

The small signal absorption coefficient in line center is

$$\alpha_0 = \frac{\mu^2\omega_0}{2n_b\hbar c\epsilon_0\Gamma_2} N_D = \frac{\Gamma_1}{\Gamma_2} N_D \frac{\pi c^2}{2\omega_0^2 n_b^2}. \tag{4.34}$$

4.2.1 Propagation in two-level systems

The equations of motion describing propagation in a two-level medium without feedback are from eq.(4.15), eq.(4.25) and eq.(4.30):

$$\partial_z E_0 = i \frac{c}{2n_b\omega_0} \Delta_\perp E_0 + i \Gamma_{trans} \alpha_0 \tilde{\chi} \frac{\Delta N}{N_D} E_0 \tag{4.35}$$

$$\partial_t \Delta N = -\frac{4\mu^2}{2^\star 2^\star \hbar^2\Gamma_2} \tilde{\chi}'' \Delta N \mid E_0 \mid^2 - \Gamma_1(\Delta N - N_D). \tag{4.36}$$

The transmitted field after a thin layer of matter, thin enough such that diffraction can be neglected, with thickness L_A is given by:

$$E_0(x, y, z + L_A) = \exp\left[i\frac{\omega_0}{2n_b c}\chi(x,y)L_a\right] E_0(x,y,z). \tag{4.37}$$

The local power transmission is

$$T(x,y) = \exp\left[-\frac{\omega_0}{n_b c}\text{Im}\chi(x,y)L_a\right]. \tag{4.38}$$

The total power transmission for a circular Gaussian beam with a radius w_0 is

$$T = \int_{-\infty}^{\infty} \int_{-\infty}^{\infty} dxdy \exp\left[-\frac{\omega_0}{n_b c} \text{Im}\chi(x,y)L_a\right] \frac{2}{\pi w_0^2} e^{-2\frac{x^2+y^2}{w_0^2}}, \qquad (4.39)$$

and for an elliptical beam with principal axes w_z, w_y

$$T = \int_{-\infty}^{\infty} \int_{-\infty}^{\infty} dxdy \exp\left[-\frac{\omega_0}{n_b c} \text{Im}\chi(x,y)L_a\right] \frac{2}{\pi w_x w_y} e^{-2\left(\frac{x^2}{w_x^2}+\frac{y^2}{w_y^2}\right)}. \qquad (4.40)$$

In an edge-emitting structure, $\chi(x,y)$ is usually assumed to be constant over the active area in the y direction due to its thinness compared to the beam width and zero otherwise. Then the integral in y can be performed easily and it turn out that the two-dimensional susceptibility can be replaced by a 1D one with two confinement factor. As consequences it is sufficient the equations for field and transmission only in 1D.

$$\chi(x,y) \rightarrow \Gamma_{trans}\chi(x). \qquad (4.41)$$

The transmission is given by:

$$T = \int_{-\infty}^{\infty} dx \exp\left[-\frac{\omega_0}{n_b c}\Gamma_{trans}\text{Im}\chi(x)L_a\right] \frac{\sqrt{2}}{\sqrt{\pi}w_x} e^{-2\frac{x^2}{w_x^2}}. \qquad (4.42)$$

4.3 Theoretical model

Following the approach developed by [28; 146] for carrier dynamics in QD we are modeling the ensemble of QD absorbers as a collection of inhomogeneously broadened two-level systems characterized by a homogeneous linewidth γ_p peaked around a frequency ω_a^C with coupling to a wetting layer (WL) as described in Fig. 4.1.

This is due to the fact that the way to grow QD is the Stransky-Krastanov growth mode, where QD have non-identical heights, results in a broadening of the spectral linewidth of the dot ensemble. Carriers in the excited states of the
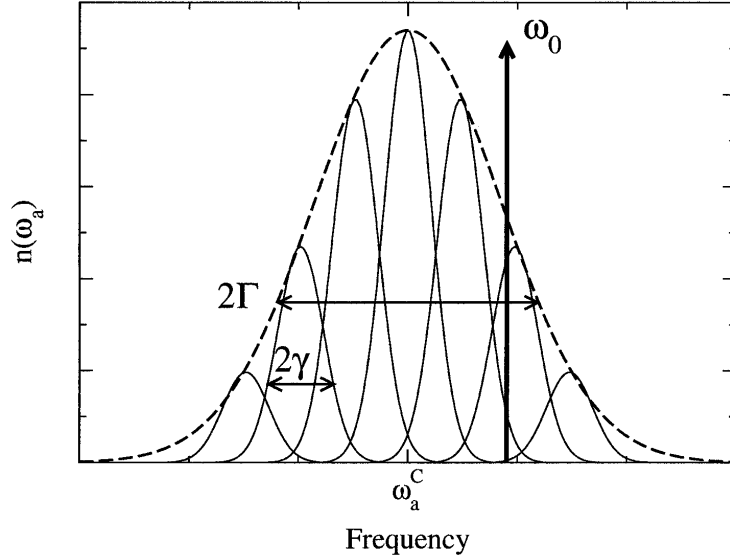
Figure 4.1: Inhomogeneous broadening of a population of two-level systems. At a given frequency, ω_0, light experiences the contribution of various classes of QD, both on the high- and low-energy side of their resonance [28].

QD [147] are not explicitly taken into account but it is assumed that WL and excited states constitute a common reservoir for the QD ground state population [148]. Due to the large separation between the lifetimes of the carriers in the QD ground state (100 ps to 2 ns) and the fast coupling between the other states to the ground state (100 fs to some ps) [147; 149] the details of this coupling are not very important for the properties of the cw state, if probing and pumping are done at the same frequency. Hence, we will use 'QD population' synonymous to 'QD ground state population' and 'WL layer population' synonymous to 'WL and excited QD state population'. The contribution of each quantum dot size class is accounted for by a statistical weight:

$$
\begin{aligned}
G(\Delta_i, \Delta) &= \frac{1}{\sqrt{\pi}(\Gamma/\gamma_p)} \exp\left[-\left(\Delta_i - \frac{\gamma_p}{\Gamma}\Delta\right)^2\right] \\
&= \frac{1}{\sqrt{\pi}(\Gamma/\gamma_p)} \exp\left[-\left(\frac{\omega_a^c - \omega_a}{\Gamma}\right)^2\right]
\end{aligned}
\tag{4.43}
$$

where ω_0 is the frequency of the light field interacting with the QD, $\Delta_i =$

$(\omega_a^c - \omega_0)/\Gamma$ is its normalized detuning from the QD population line center, $\Delta = (\omega_a - \omega_0)/\gamma_p$ is the single dot detuning from resonance and γ_p and Γ are the homogeneous and inhomogeneous broadening parameters.

The equations of motion for the electron and hole population in the QD, n^e, n^h, and in the WL, N^e and N^h, are for driving with linearly polarized light:

$$
\begin{aligned}
\frac{\partial n^{e,h}}{\partial t} &= -\gamma_{nr}\Big[n^{e,h} + \frac{|E|^2}{1+\Delta^2}(n^e + n^h - \Pi) \pm \\
&\quad B_{he}N_{WL}^h n^e(\Pi - n^h) \mp B_{eh}N_{WL}^e n^h(\Pi - n^e) \\
&\quad +\gamma_{esc}^{e,h}n^{e,h} - \sigma_{cap}^{e,h}N_{WL}^{e,h}(\Pi - n^{e,h})\Big] \\
\frac{\partial N_{WL}^{e,h}}{\partial t} &= -\gamma_{nr}^{WL}\Big[-\Lambda + N_{WL}^{e,h} - \gamma_{esc}^{e,h}\int n^{e,h}G(\Delta_i, \Delta)d\Delta \\
&\quad -\sigma_{cap}^{e,h}N_{WL}^{e,h}\int(\Pi - n^{e,h})G(\Delta_i, \Delta)d\Delta\Big] \\
&\quad \mp B_{he}N_{WL}^h\int n^e(\Pi - n^h)G(\Delta_i, \Delta)d\Delta \\
&\quad \pm B_{eh}N_{WL}^e\int n^h(\Pi - n^e)G(\Delta_i, \Delta)d\Delta.
\end{aligned}
$$

(4.44)

(4.45)

Here γ_{nr} and γ_{nr}^{WL} denote the decay rates of carriers in the QD and the WL, respectively. E represents the optical field strength, Λ the injection current, $\Pi = 2$ the level degeneracy for the two opposite spins. All parameters are suitably scaled [28; 146]. The equation for the carrier populations need to be solved for the different size classes: i.e $n^{e,h} = n^{e,h}(\Delta)$. We use 61 classes in our code. We do not consider coupling between QDs due to diffusion in the WL because the effective diffusion length is not larger than 1 μm [150] and we are interested in structures on a larger scale. The terms in the second line of Eq. (4.44) and the third and last lines of Eq. (4.45) represent Auger processes coupling the carrier populations in WL and QD as illustrated in Fig. 4.2. [151]

The other coupling processes present in Eqs. (4.44), (4.45) are thermally activated escape from the QD to the WL and the capture of carriers from the WL into the QD. When we account for the energy level spreading of dots, the capture γ_{esc} and the escape coefficients σ_{esc} can be phrased as [28; 146]:
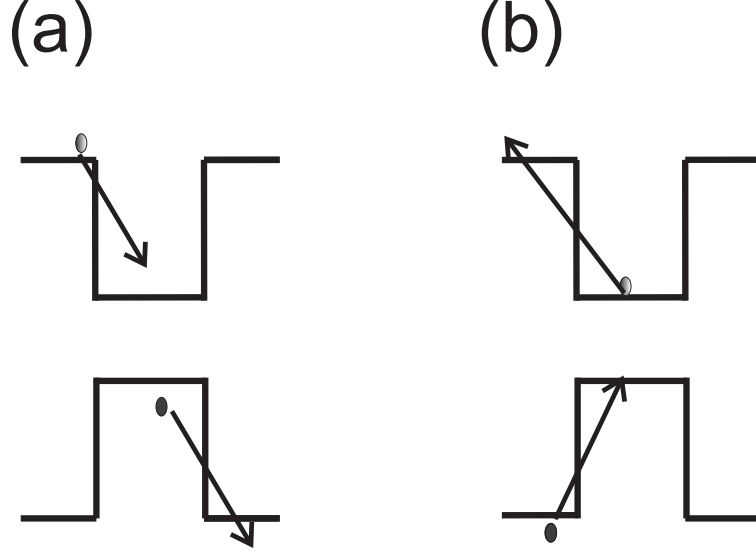
Figure 4.2: (a) Auger capture process of type I represented by the coefficient B_{eh}: a WL electron is scattered into the QD and a hole is scattered from the QD to the WL; (b) Auger capture of type II characterized by the coefficient B_{he} : a hole from the WL is scattered into the QD and an electron is captured from the QD in the WL.

$$\gamma_{esc} = \bar{\gamma}_{esc} \exp \left(-\frac{\Gamma}{\gamma_p} \beta \Delta_i \right) \exp(\beta \Delta), \qquad (4.46)$$

$$\sigma_{cap} = \bar{\sigma}_{cap} \exp \left(\frac{\Gamma}{\gamma_p} \beta \Delta_i \right) \exp(-\beta \Delta), \qquad (4.47)$$

with $\beta = \hbar \gamma_p / k_b T$ ($k_b T$ thermal energy).

The direct physical interpretation of γ_{esc}, is that when the difference in energy between the WL and the GS is bigger, the carrier lasts long in the ground state, i.e., it is more difficult for it to escape into the WL. γ_{esc} is just the inverse of the escape time, $\tau^{ES} \propto \exp \left[(E_{WL} - E_{GS}) / k_B T \right]$.

4.4 Parameters used for the simulation

The parameters used for the simulations and the model are summarized in table 4.1. We are choosing parameters typical for InGa QD emitting in the 1.3 μm

region at room temperature [22; 36; 68; 147; 149].

Table 4.1: Value of the parameter used for the simulation and in the model

Parameter	Normalized value	Real value
Non radiative decay rate for e and h in QD (γ_{nr})	0.15	78 ps
Non radiative decay rate for e and h in Wl (γ_{nr}^{WL})	0.15	78 ps
Capture rate cross section into the QD(σ_{cap})	500	6.4 ps
Escape rate for electron from the QD (γ_{esc}^{e})	0.01	667 ps
Escape rate for hole from QD (γ_{esc}^{h})	100	0.067 ps
Thermal imbalance in QD occupation (Δ)	0.02	0.2
Pumping rate in the WL (Λ)	1.8	0.46 s^{-1}cm^2
Auger coefficient (B_{he})	200	6×10^{10} cm^2 s^{-1}
Auger coefficient (B_{eh})	200	6×10^{10} cm^2 s^{-1}
Cavity detuning (θ)	-2	-2
Detuning normalized to Γ (Δ_i)	1	300
Linewidth of homogeneous broadening (γ_p)	15	15 nm
Linewidth of inhomogeneous broadening (Γ)	60	60 nm
Quantum dot sheet density (N_{QD})	5×10^{10} cm^{-2}	
Number of QD layer (N_l)	10	
Spacing (d)	$10 \times 3.9 \times 10^{-8}$ m	
Length of the sample (L_a)	1 mm	
Dipole matrix element (μ)	1.23×10^{-28} Cm	
Wavelength (λ)	$1.3\,\mu$m	
Radiative lifetime	0.5 ns	
Confinement factor (Γ_{trans})	0.094	

The equation for the conversion that led the scaled unit to the normal one are described below. Starting from the time scale of 11.7 ps chosen for historical reason [152] and because is in between the fast time scales governing the GS-WL dynamics and the slow role of the GS population, more than 10 ps. This led to the value for the non radiative decay for electrons and holes of 78 ps. The capture rate instead is given by $\sigma_{cap} = (\sigma_{cap}/\gamma)$=6.4 ps^{-1}. The escape coefficient rate for electron is given by $\gamma_{esc}^{e} = \gamma_{esc}^{e}/\gamma_{nr}$=0.067 ps^{-1}.

The thermal imbalance in QD occupation is given by $\Delta = \hbar\gamma_p/(k_bT)$ where $\hbar = 1.05 \times 10^{-34}$ Js, $k_b = 1.38 \times 10^{-23}$ Cm, and T is the temperature.

The scaling of pump pumping rate is given by $\Lambda = \Lambda/(N_{QD}\gamma_{nr}^{WL}) = 0.46$ s^{-1} $\times$cm^2. The auger coefficient are scaled as $B_{he,eh}=(\gamma_{nr}/N_{QD})$, $B_{he,eh} = 6 \times 10^{10}$
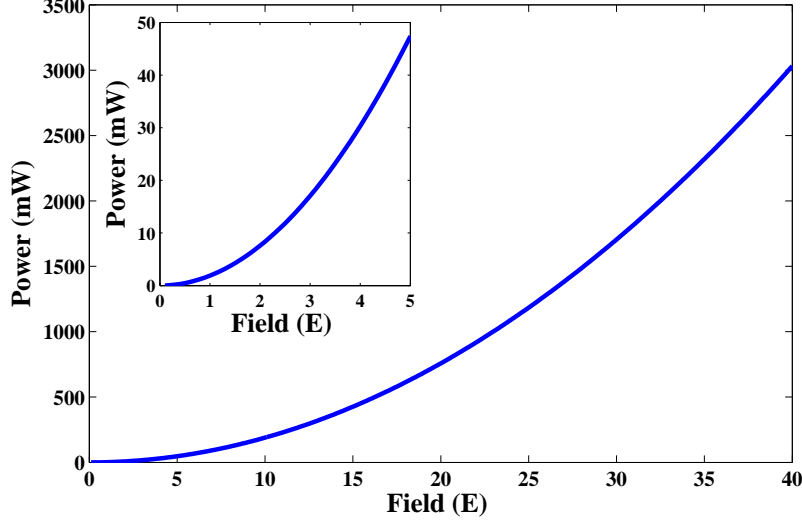
Figure 4.3: Power versus normalized field. The inset shows an enlargement for low field values.

cm ^{2} s $^{-1}$ The dipole matrix element is given by:

$$\mu^2 = \frac{\pi \hbar \gamma \epsilon_o c^3}{\omega_o^3 n_b} \tag{4.48}$$

the value obtained is $\mu = 1.23 \times 10^{-28}$ Cm for a radiative lifetime of 0.5 ns. The scaling for the field is given instead by:

$$E = E_{norm} \left(\frac{\hbar^2 \gamma_p \gamma_{nr}}{2\mu^2} \right)^{1/2} \tag{4.49}$$

where E_{norm} is the normalized field strength. From that we can infer the intensity given by: $I = (n_b c \epsilon_o / 2) E^2$. To scale in power we need to multiply by the active area:

$$P = \frac{I \omega_x \omega_y \pi}{2} \tag{4.50}$$

where of $\omega_x = 1.55 \times 10^{-5}$ m is the radius of the fundamental mode in the slow direction and $\omega_y = 0.5 \times 10^{-6}$ m is the same for the fast axis. This led to the scaling in power of Fig. 4.3.

From Fig. 4.3 is possible to infer the relevant corresponding power compared to the field. It is worth to spot the relation between field strength and power.

These value led to $< \alpha_{0,I} >= 26/cm$ in good agreement with observation [68; 149] and is actually a conservative value.

4.5 Modal susceptibility of self-assembled quantum dot

The imaginary and real part of the normalized susceptibility χ_I, describing the strength of light-matter interaction are given by [28; 64] :

$$\text{Im}(\chi_I) = - \int \frac{1}{1+\Delta^2}(n^e + n^h - \pi)G(\Delta_i, \Delta)d\Delta \qquad (4.51)$$

$$\text{Re}(\chi_I) = - \int \frac{\Delta}{1+\Delta^2}(n^e + n^h - \pi)G(\Delta_i, \Delta)d\Delta \qquad (4.52)$$

Here, for (energetically) deeply buried QDs, we neglected possibly contributions from the WL states and high-level QD states [133] in order to elucidate the principles in a first treatment.

The numerical code (Fortran 77) obtained from University of Bari has been adapted for the present situation. The spatio-temporal dynamics of Eqs. (4.44), (4.45) are directly integrated using a split-step operator integrator, in which nonlinear terms are computed via a second order Runge-Kutta method and the Laplacian by a fast Fourier transform (FFT) [153] on a transverse computational mesh of 64 grid points.

Eqs. (4.44), (4.45) are solved numerically for a cw Gaussian input beam $E(x) = E_0 \times \exp\left(-x^2/w_0^2\right)$ on a numerical grid with 64 space point and a beam waist w_0 of 15 points. The number of iteration is 8000, found to be sufficient to approach an "asyntothic" level.

The equations for the quantum dot case are obtained from eq.(4.32) by inserting

$$\chi = \frac{\mu^2 N_D \chi_I}{\hbar\epsilon_o\gamma_p} \qquad (4.53)$$

into the propagation equations for the two-level medium.

χ_I is a lineshape function that takes into account the inhomogeneous broadening and spin degeneracy and depends on the number of electron and holes n_e,n_h in the quantum dot.

The small-signal absorption coefficient for the inhomogeneously broadened medium is

$$\alpha_{0,I}(\Delta_i) = \frac{\omega_0 \mu^2}{n_b c \hbar \epsilon_0 \Gamma_2} N_D \text{Im} \chi_I(\Delta_i, n_e = n_h = 0). \tag{4.54}$$

In VCSELs,

$$N_D = \frac{N_{QD} N_l}{L_A} \tag{4.55}$$

in EEL

$$N_D = \frac{N_{QD} N_l}{d}, \tag{4.56}$$

where Δ_i is the detuning to the inhomogeneous broadening line, N_l is the number of QD layers, d is the total thickness of the active zone (EEL) and L_A the total length of the active zone (VCSEL). Hence the absorption coefficient per unit length is independent of the number of QD layers and depends only on N_{QD} and thickness of one layer (the distinction is important for the refractive index though, see below). In the edge-emitting case the modal absorption coefficient is

$$< \alpha_{0,I}(\Delta_i) >= \Gamma_{trans} \alpha_{0,I}(\Delta_i). \tag{4.57}$$

In experiments, $< \alpha_{0,I}(0) >$ is often measured. This can be used for the calibration of density and matrix element, if the integral

$$\text{Im} \chi_I(0, n_e = n_h = 0) = \frac{\Gamma_2}{\sqrt{\pi} \Gamma_D} \int_{-\infty}^{+\infty} d\bar{\Delta} \frac{2}{1 + \bar{\Delta}^2} e^{-\left(\frac{\Gamma_2}{\Gamma_D} \bar{\Delta}\right)^2} \tag{4.58}$$

is calculated numerically

Calculations are performed for the (quasi-one-dimensional) case of an edge-emitter. The resulting spatial distributions $n^e(x)$ and $n^h(x)$ are then used to calculate the spatial distribution of the susceptibility by Eqs. (4.70) and (4.52).

In order to make a connection to experiments, the scaled units need to be

related to real ones. The unscaled susceptibility is:

$$\chi(\Delta_i, n_e, n_h) = \left(\frac{\mu^2 N_{QD} N_l}{\hbar \epsilon_0 \gamma_p d} \right) \chi_I(\Delta_i, n_e, n_h), \qquad (4.59)$$

from which the absorption coefficient for the intensity can be obtained as

$$\alpha_I(\Delta_i, n_e, n_h) = \frac{\omega_0}{n_b c} \text{Im}\chi(\Delta_i, n_e, n_h). \qquad (4.60)$$

Here, N_{QD} is the sheet density of QD, N_l is the number of QD layers, d is the total thickness of the active zone, μ is the dipole matrix element. In the experiment, one is not measuring the absorption coefficient directly but transmission. Typically, the latter will be integrated over the beam in addition:

$$T = \int \exp\left[-\Gamma_{trans}\alpha_I(x)L_a\right] \left(\frac{2}{\pi}\right)^{1/2} \frac{1}{w_0} \exp\left(\frac{-2x^2}{w_0^2}\right) dx \qquad (4.61)$$

where Γ_{trans} is the confinement factor for an edge-emitting structure and L_A is the length of the sample.

4.5.1 Results

Fig. 4.4 displays the gain, respectively absorption, coefficient obtained from Eq. (4.61) in dependence of the input intensity for different detuning. For all curves, it starts at the small-signal value and then drops to the vacuum value of zero due to the generation of carriers and the resulting bleaching.
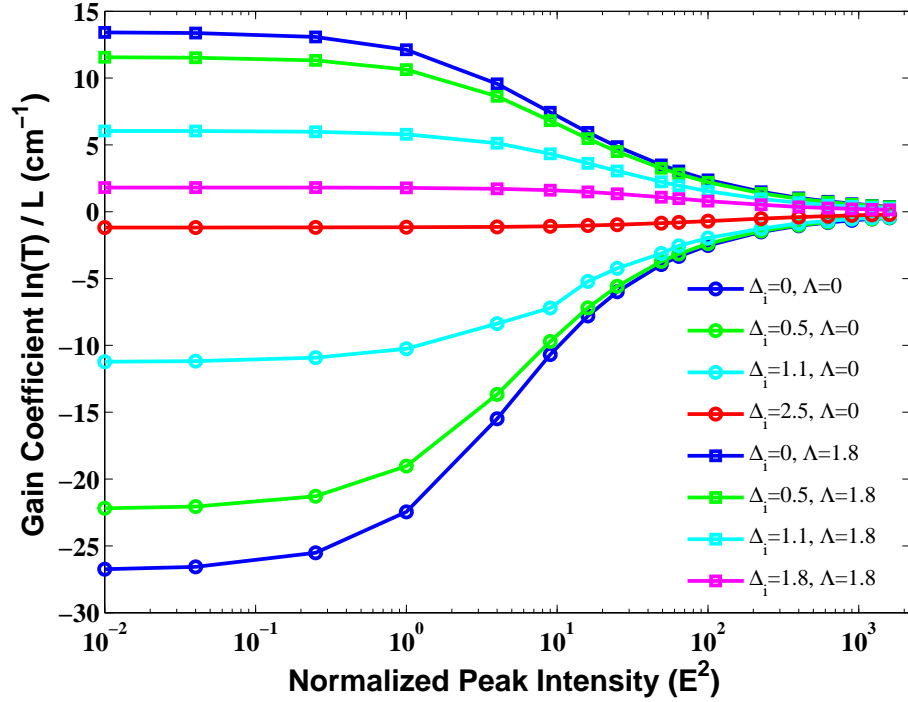
Figure 4.4: Modal gain coefficient as a function of the normalized intensity in the center of the Gaussian input beam for different values of the detuning in the absorption (circles)and gain regimes (squares)

Obviously, the small-signal absorption/gain is highest at $\Delta_i = 0$ and decreases for increasing modulus of detuning according to Eq. (4.60). The intensity where saturation becomes apparent seems to increase with increasing modulus of detuning.

The ratio of $\Gamma/\gamma_p = 4$ refers to a Voigt-profile situation. The Voigt profile [154], is a spectral line profile named after Woldemar Voigt and found in all branches of spectroscopy in which a spectral line is broadened by two types of mechanisms (homogeneous broadening and inhomogeneous), one of which alone

would produce a Gaussian profile (usually, as a result of the Doppler broadening), and the other would produce a Lorentzian profile. Since neither homogeneous nor inhomogeneous broadening are clearly dominating, we fit the dependence of the gain coefficient on intensity with different models that describe saturable absorption in the case of two-level systems with inhomogeneous, $\alpha_I = \alpha_{0,I}/\sqrt{(1 + E^2/I_{sat})}$ and homogeneous, $\alpha_I = \alpha_{0,I}/(1 + E^2/I_{sat})$, broadening [144]. The latter proves to fit best the simulation. We show in Fig. 4.5, I_{sat} vs Δ_i as extrapolated from the above formula. The saturation intensity is minimal at $\Delta_i = 0$ and is slightly different for the gain ($E^2 = 6.83$) and the absorption case ($E^2 = 2.99$).
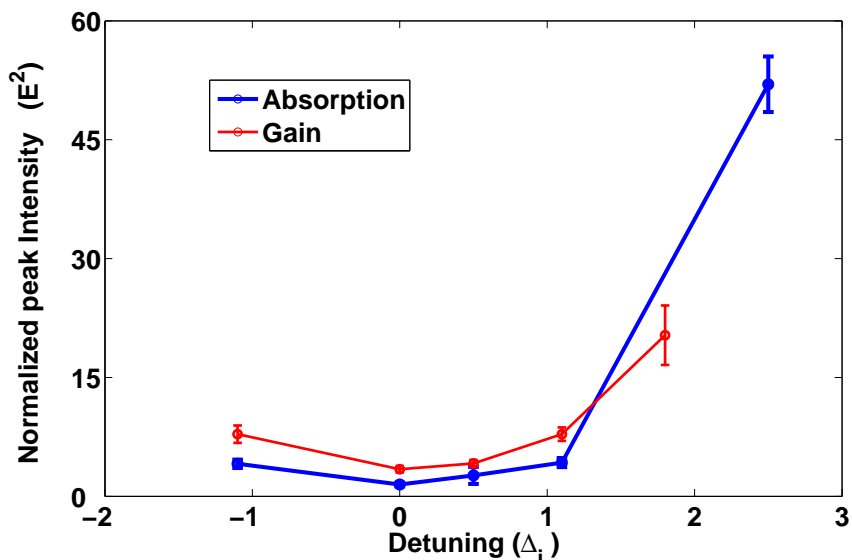
Figure 4.5: Saturation intensity as function of the detuning in absorption $\Lambda = 0$ and gain cases, $\Lambda = 1.8$.

It strongly increases in both cases for increasing modulus of the detuning, whereas it should be constant in the strongly inhomogeneous limit [144]. For an experimental situation with $w_x = 15\ \mu$m and $w_y = 0.5\ \mu$m, $E^2 = 1$ corresponds to a power of 2.1 mW. Hence the minimum value of the saturation power is 3 mW in the absorption case and 6.8 mW in the gain case. If instead of $\gamma = 0.15$ (or 78 ps lifetime), the purely radiative lifetime is considered, the corresponding values are about a factor of 10 lower and easily accessible experimentally.

4.6 Self-lensing in self-assembled quantum dots

Self-focusing or lensing is a non-linear optical phenomenon induced by the change in refractive index of materials exposed to intense electromagnetic radiation [155; 156].

A medium whose refractive index increases with the optical field intensity acts as a focusing lens for an electromagnetic wave characterized by an initial transverse intensity gradient, as in a laser beam [145]. The peak intensity of the self-focused region keeps increasing as the wave travels through the medium, until defocusing effects or medium damage take place.

Self-focusing is an important mechanism for studying transverse effects in resonators containing a nonlinear medium. One example is Kerr-lens self-mode locking in solid state lasers [157] or nonlinear spectroscopy [158].

Describing a nonlinear medium in terms of a self-induced lens allows to describe the nonlinear cavity and medium in terms of a linear one containing a parameter-dependent lens. In this case the system can be treated with the ABCD matrix formalism in this way simplifying the theoretical description.

According to [145], the radius of curvature acquired by a wave propagating a distance δz in a medium with a radially varying refractive index is given by:

$$\frac{1}{R(r)} = \frac{1}{r}\frac{\partial}{\partial r} n(r)\,\delta z \tag{4.62}$$

For a parabolic variation of the refractive index: $n(r) = n_0 - \frac{1}{2}n_2 r^2$, this is independent of r and equal to the curvature n_2, i.e. a perfect lens. Hence, we can identify an effective focal power:

$$\frac{1}{f} = -\frac{1}{r}\frac{\partial}{\partial r} n(r)\,\delta z = n_2\delta z \tag{4.63}$$

possibly spatially varying and thus representing an imperfect lens.

The refractive index is given by:

$$n = \frac{1}{2n_b}\operatorname{Re}\chi = \frac{1}{2n_b}\frac{\mu^2}{\hbar\epsilon_0\Gamma_2}\frac{N_{QD}N_l}{L_A}\operatorname{Re}\chi_I = \Delta n_0 \operatorname{Re}\chi_I \tag{4.64}$$

where the definition

$$\Delta n_0 = \frac{\mu^2}{2n_b\hbar\epsilon_0\Gamma_2}\frac{N_{QD}N_l}{L_A} \tag{4.65}$$

enables us to split the refractive index in a normalized part and a prefactor characterizing the sample under study.

The corresponding value for an edge-emitting device is given by:

$$< \Delta n_0 >= \frac{\mu^2}{2n_b\hbar\epsilon_0\Gamma_2}\Gamma_{trans}\frac{N_{QD}N_l}{d}, \tag{4.66}$$

where d is the thickness of the active zone. Then

$$\frac{1}{f} = -\frac{1}{r}\frac{\partial n}{\partial r}(r)\,L_A = -\Delta n_0\,L_A\left(\frac{1}{r}\frac{\partial}{\partial r}\mathrm{Re}\chi_I(r)\right), \tag{4.67}$$

The curvature of the normalized $\mathrm{Re}\chi_I$ is calculated by taking 2 times the maximum of $\mathrm{Re}\chi_I$ minus the symmetric value of $\mathrm{Re}\chi_I$ 4 space point and dividing by the distance between these symmetric point.

Once is determined the curvature, then we need to multiply by $\Delta n_0 L_A$. Since the input beam is spatially varying, also the refractive index is. Around the beam center, the variation is necessarily parabolic. If the refractive index distribution would be a pure parabola, the focal power would be constant over the whole beam, thus implying an aberration-free equivalent lens. In reality, this is obviously not the case because the pumping Gaussian has an inflection point. Nevertheless the parabola is often a good approximation in beam center where most of the beam energy is. This was studied in detail in atomic vapors [142]. In any case, the curvature will give a quantitative indicator for the strength of beam shaping even if the lens is not perfect. The focusing can be experimentally detected by a change of the beam width in far field [159] or at some distance after the medium [142] (similar as in z-scan techniques [141]). In this first treatment, we will confine to a thin lens to demonstrate the principles. For a quantitative description of a real experiment it might be necessary to include absorption and nonlinear beam reshaping during propagation.

4.6.1 Results

Fig. 4.6 shows how the lens power change as function of input intensity for different detuning in the absorption case. Apart from the $\Delta_i \approx 0$-case, the focal power increases from zero with increasing intensity, reaches a peak at an intermediate intensity and decreases again if the intensity is increased further.
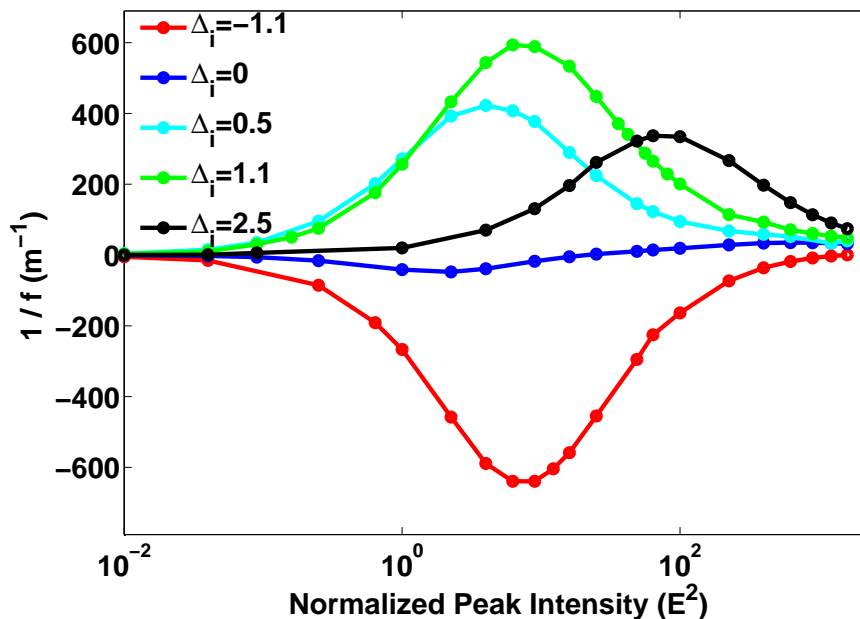
Figure 4.6: Focal power as function of normalized peak intensity for different detuning in the absorption case.

The sign of the lensing depends on the sign of detuning and whether the sample is absorbing or providing gain (see Fig. 4.8), as expected. The maximum lens effect occurs at $\Delta_i = 1.1$ and $E^2 = 9$ ($P = 19$ mW). The focal power is maximum at an intermediate input power a few times higher than the saturation power. The intensity needed to obtain maximum lens power increases for increasing modulus of detuning. This is probably due to the fact that the saturation intensity increases with detuning and the maximum effect is found for the same saturation condition.

The fact that the maximum focal power is obtained at intermediate input intensity can be explained by looking at Fig. 4.7. For low intensity the curvature

follows the curvature of the input profile ('Kerr-limit', $\Delta n(x) \sim |E|^2(x)$), but the total effect is low because the excursion from the background refractive index is small (note that the curve is blown up by a factor of 10). For high intensity, the excursion is large ($\mathrm{Re}(\chi_I)$ becomes nearly zero) but the total focal power is again low because the curvature is strongly reduced. This is due to the fact that saturation is effective over a large area at high intensities.
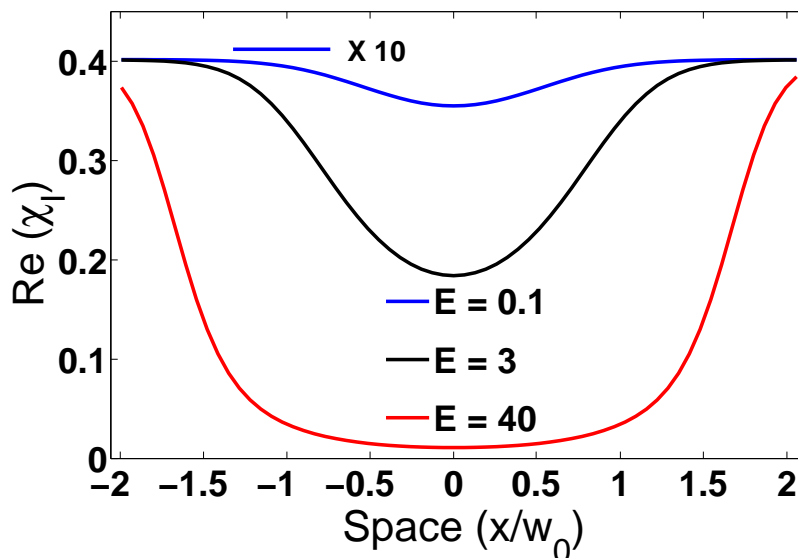
Figure 4.7: Spatial profile of the real part of the susceptibility for low (blue line, amplitude enhanced by a factor of 10), intermediate (black line) and high excitation (red line). $\Lambda = 0$, $\Delta_i = 1.1$. The total excursion is $\Delta n = 1.6 \times 10^{-4}$.

The case of intermediate intensity is in between: On the one hand the excursion is of reasonable size, about half the maximal effect, on the other hand the curvature is still quite close to the one of the input beam. Both is characteristic for intensity levels around the saturation intensity, i.e. for the onset of saturation, and hence the total effect is maximal. Similar characteristics were found for atomic vapors [142]. There, in the homogeneously broadened case, it can be demonstrated analytically that maximum focal power is found at the saturation power [142].

The lensing effect is minimal at $\Delta_i = 0$. Indeed, in a purely two-level system no effect at all is expected for $\Delta_i = 0$ because the contributions of blue and
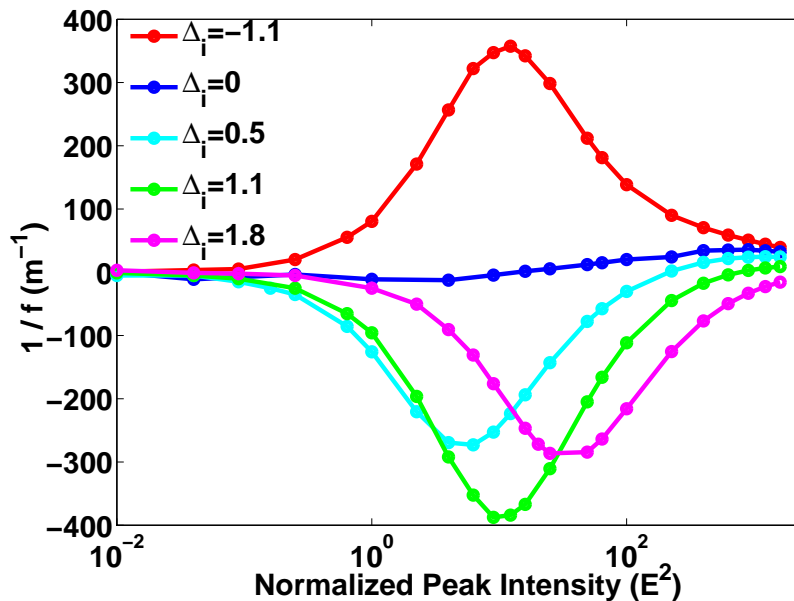
Figure 4.8: Focal power as function of normalized peak intensity for different detuning in the gain case.

red detuned size classes cancel. It is the thermally induced coupling to the WL (described by the parameter β) which breaks that symmetry.

Fig. 4.8 refers to the case of gain of $\Lambda = 1.8$. The values of focal power are lower compared to the absorption case but they exhibit the same behavior: the focal length start from a low value to increase up to a maximum at intermediate intensity to decrease again. The curves are flipped compared to the absorption case as expected.

In the peak, the predicted lensing effect is actually quite substantial, $|f_{min}| \approx$ 1.7 mm, in a sense, because the focal length reaches the length of the medium $L_A = 1$ mm, i.e. the point where the approximation by a thin lens becomes questionable.

These values were calculated assuming an input beam radius of $w_0 = 15$ μm chosen because it would be conveniently to work with experimentally and being somewhat larger than typical fundamental mode sizes in edge-emitting lasers, i.e. in a range where filamentation phenomena might occur. The size of cavity solitons is also in that range (about 10 μm [126; 160]).

4.7 Experimental observability of the lensing effect

Nevertheless, it turns out that an experimental confirmation is not straightforward: The modification of the input beam by the lensing of the sample can be detected by either measuring the on-axis amplitude (being proportional to the square of the new beam waist of the transmitted beam, $w_0'^2$) or the beam width in far field ($\sim 1/w_0'^2$) [159] or, more sensitively, by measuring the beam size either directly or via the transmission through a pinhole at some suitable chosen distance after the medium as it is done in usual z-scan techniques [141]. Replacing the medium by a thin lens of focal length f, the size of the new beam waist w_0' can be calculated by ABCD-matrix theory as

$$w_0' = w_0 \, \frac{1}{1 + \frac{\pi w_0^4}{\lambda^2 f^2}}. \tag{4.68}$$

For an input beam waist of $w_0 = 15~\mu$m and a thin lens with $f \approx 1.7$ mm, the new beam waist is $w_0 = 14.3~\mu$m at a distance of 0.16 mm from the back focal plane of the lens. This rather small change in beam is quite difficult to detect. Eq. (4.68) says that the effect becomes more pronounced if the initial beam radius is increased (at constant f), being substantial if the Rayleigh length of the input beam $z_r = \pi w_0^2 / \lambda$ is of the order of f. In reality, however, the focal length scales like $f \sim w_0^2$, since, as discussed for Fig. 4.7, the curvature of the susceptibility profile follows the curvature of the input beam in first approximation for not too strong saturation (see [142] for an analytical treatment). Hence, actually the strength of the detected signal can't be influenced by choice of the input beam size.

However, due to the approximately quadratic dependence of the ratio of w_0^2 / f, the situation rapidly improves with increasing focal power. For example, a change of size by 20%, which should be experimentally detectable, is reached already for a focal power of about 1000/m, i.e. only about two times the maximum value reported in Fig. 4.6, Fig. 4.8.

4.8 Variation of the parameters

Since it appears that the numbers are somewhat at the edge, it is useful to discuss the influence of other uncertainties, e.g. the exact nature of the relaxation processes between the QD and WL states. First, we changed the ratio between the electron and hole escape from 10^{-4} to 10^{-2} and 1.
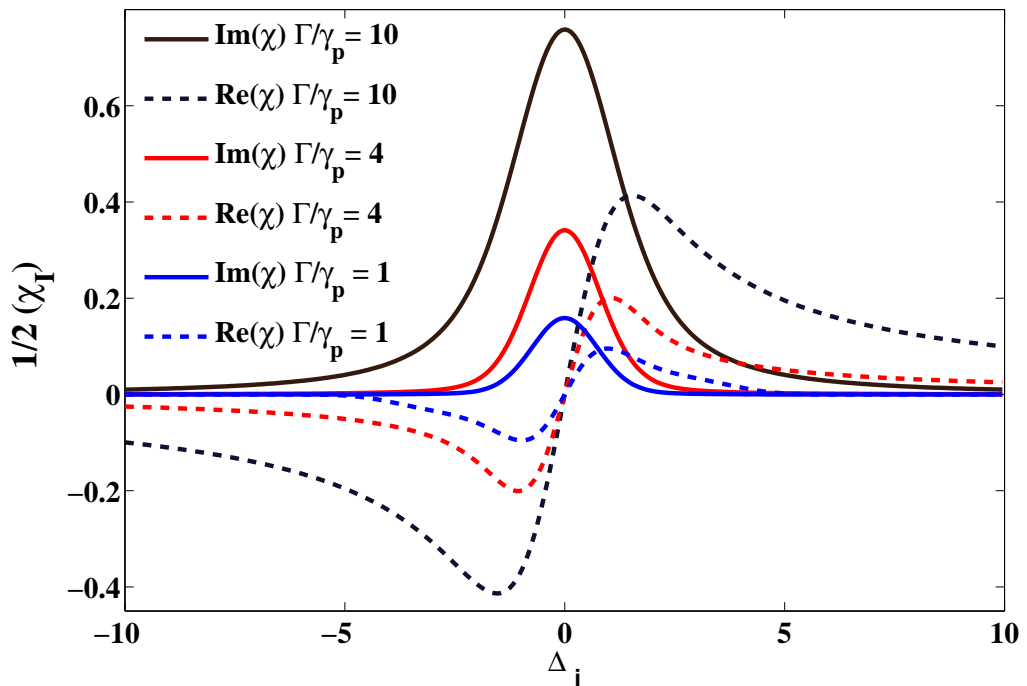
Figure 4.9: Real and Imaginary part of the linear susceptibility as function of detuning for different ratios between homogeneous and inhomogeneous broadening.

For detuned excitation ($\Delta_i = 1.1$), the effect on $\mathrm{Re}(\chi_I)$ is negligible and about 22% on $\mathrm{Im}(\chi_I)$. At resonance ($\Delta_i = 0$), the values are 19% on $\mathrm{Re}(\chi_I)$ and 6% on $\mathrm{Im}(\chi_I)$. Switching the Auger processes completely off, on resonance the change of $\mathrm{Im}(\chi_I)$ is 21% and 60% for $\mathrm{Re}(\chi_I)$ (but the total value is very small as discussed above). For $\Delta_i = 1.1$, the change is 64% for $\mathrm{Im}(\chi_I)$ and 7% for $\mathrm{Re}(\chi_I)$.

Fig. 4.9 shows how real and imaginary part of the linear susceptibility change as function of detuning for different ratios between homogeneous and inhomo-

geneous broadening. Since the linear susceptibility defines the maximum value of the nonlinear index change, this provides a good guidance on the maximum effect to be expected. Choosing a ratio of $\Gamma/\gamma_p = 10$ instead of 4 decreases the maximum of the real part of the susceptibility by a factor of 2.1. For a ratio of $\Gamma/\gamma_p = 1$, it is a factor of 2 higher. Hence, at constant γ_p, one can expect to benefit from improved growth with a reduced inhomogeneous broadening [161; 162]. Note that increasing γ_p at constant Γ is not beneficial because the increase of the scaled susceptibility is sublinear (Fig. 4.9) and is overcompensated by the dependence of the proportionality factor between scaled and unscaled susceptibility on γ_p, see Eq. 4.59.

We conclude that though uncertainties in the relaxation constants will influence the measurements quantitatively, our overall conclusion that the lensing is at the edge of being detectable is not changed.

Finally, the carrier lifetime in the QD was assumed be 78 ps, much smaller than the radiative lifetime of 500 ps. This was done on the one hand to be on the conservative side with respect to the possible influence of defect induced recombination and on the other hand to reduce the computational load, which is rather high due to the separation of time scales between scattering processes between WL and QS and carrier lifetime in QD and due to the fact that the carrier density needs to be spectrally and spatially resolved in our case. We did some test runs using a lifetime of 0.5 ns which yield an increase of 10% in saturation and negligible effect in lensing. Note that the influence of the lifetime on the scaling of the saturation power can be treated exactly without additional calculations (as discussed above) due the way the equations are scaled.

4.9 Nonlinear index shift

A very sensitive approaches to obtain refractive index shift is to measure the shift of the resonances of a Fabry-Perot cavity with QD (e.g. a laser below threshold or without electrical injection). If $n_b \approx 3.41$ is the background index, the shift of a cavity resonance expected as function of wavelength is given by:

$$\Delta\lambda = \frac{\Delta n}{n_b}\lambda_0 \tag{4.69}$$

where Δn is the maximum refractive index shift and is on the order $\Delta n = 1.6 \times 10^{-4}$, see Fig. 4.7. For $\lambda = 1.3$ μm the expected shift is 0.06 nm. For $\lambda = 0.8$ μm it is 0.037 nm.

This is a quarter of a free spectral range of a 1 mm sample and one free spectral range for a 4 mm sample for $\lambda = 1.3$ μm , hence it should be possible to detect in experiment, as discussed later in the thesis.

4.10 Spectral hole burning in self-assembled quantum dots

When a large flux density of monochromatic photons at frequency ν_1 is applied to an inhomogeneously broadened medium, the gain saturates only for those atoms whose lineshape function overlaps ν_1. Other atoms simply do not interact with the photons and remain unsaturated. When the saturated medium is probed by a weak monochromatic light source of varying frequency ν, the profile of the gain coefficient therefore exhibits a hole centered around ν_1, as illustrated in Fig. 4.10. This phenomenon is known as spectral hole burning. Since the gain coefficient $\gamma_{barra}(\nu)$ of the subset of atoms with velocity v_β has a Lorentzian shape with width δ_{ν_s}, it follows that the width of the hole is δ_{ν_s}. As the flux density of saturating photons at ν_1 increases, both the depth and the width of the hole increase.

The spectral hole burning (SHB) of self-assembled QD is a nonlinear optical effect in zero-dimension [163].

First observation of SHB in photocurrent spectra of InAs self-assembled QDs has been addressed by [164]. At 5 K, a narrow hole with width of less than 1 nm was observed and the hole depth increased as electric field increased with the writing light power of 8 mW. The hole was observed up to 40 K. Heotz et al. [165] observed SHB for self-organized InAs/GaAs with Full Width Half Maximum of the spectral hole of 190 μeV. Also direct observation of the coherent hole in the
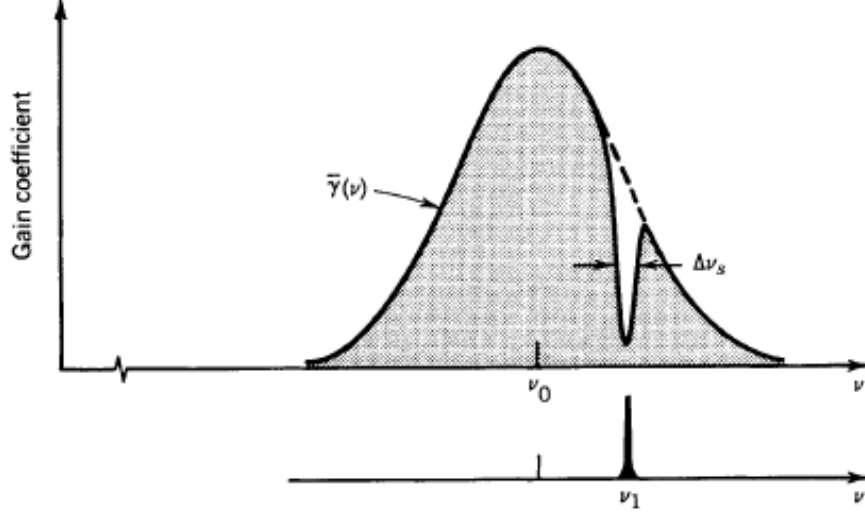
Figure 4.10: Gain coefficient saturated by a large flux density at frequency ν_1 [163].

spontaneous emission spectra with a width of 500-600 GHz hole in a saturated quantum dash amplifier is reported in [166].

An important application of spectral hole burning is resonant high-resolution spectroscopy [167] in the spectral range beyond that covered by single QD spectroscopy.

Our model allows to get an estimation of the spectral hole burning at room temperature. We follow the equation:

$$\text{Im}(\chi_I, \Delta_i) = -\int \frac{1}{1 + \Delta^2}(n^e + n^h - \pi)G(\Delta_i, \Delta)d\Delta \qquad (4.70)$$

and choose different value coming out from the numerical simulation of the value of n^e and n^h depending on the intensity of the normalized field (E). Fig. 4.11 shows how the imaginary part of susceptibility change for different detuning and increasing field. It is possible to see that the effect becomes recognizable when the field is quite high, E = 10. The whole profile decrease and the hole becomes deeper.

The profile is asymmetric especially at starting normalized field of E = 10.

As looking at Fig. 4.3 a field strength of 10 correspond to an optical power of

already 250 mW. The strong broadening is expected due to high saturation. The large width expected due to coupling via the wetting layer.
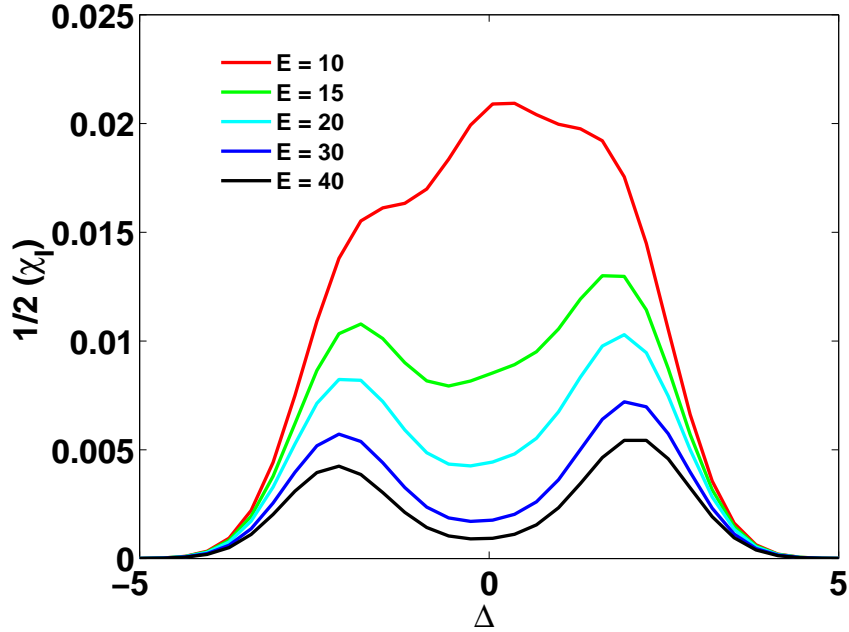
Figure 4.11: Imaginary part of susceptibility as function of detuning for pumping at $\Delta_i = 0$, $\Lambda = 0$.

4.11 Linewidth enhancement factor for quantum dot

Since the refractive index is related to the real part of the susceptibility and the gain is linked to the imaginary part of the susceptibility, the α-factor can be evaluated as [28]:

$$\alpha \approx \frac{d\mathrm{Re}(\chi)/dN}{d\mathrm{Im}(\chi)/dN} \tag{4.71}$$

N is the total carrier density $N = \int (n_e + n_h)G(\Delta)d\Delta$ defined as the total density of electrons and holes. We took the rate of the difference of the beam center of real and imaginary part of susceptibility for different detunings. The set

of parameters adopted for the calculation of the susceptibility and of the α-factor are the same reported for the previous simulation. In order to calculate the α-factor we must consider a fixed value of Δ_i and then make a scan over the carrier density so to calculate in a numerical way the derivative of the susceptibility with respect to N.
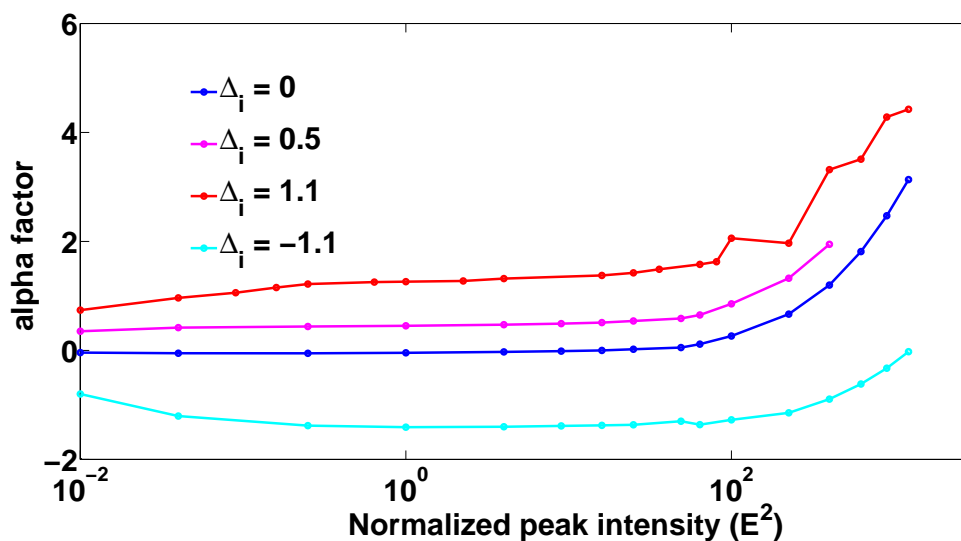
Figure 4.12: α-factor as function of normalized peak intensity for different detuning with $\Lambda = 0$.

Fig. 4.9 shows how the α-factor evolves as function of the normalized peak intensity for different detuning. It is possible to see that the α factor for negative detuning ($\delta_i = -1.1$) is negative for almost all the peak intensity, increasing only at very high intensity. For $\Delta_i = 0$ it stay constant to zero until it increase to almost 4 at very high peak intensity. For positive detuning it is constant positive until some point to increase again. Fig. 4.9 is related to Fig. 4.12, indeed the change of sign of the α-factor is related to the change of sign of Δ_i as expected.

.

Chapter 5

Saturation of gain and absorption in quantum dots with continuous-wave driving

5.1   Introduction

We report, in this chapter, studies on the interaction strength information between continuous wave (cw) laser and self assembled quantum dots, as a function of power in the form of the absorption coefficient and gain. Firsts are reported studies on using equal QD diode as slave and master but with no idea of coupling efficiency between them. After a new technique is developed to couple ligth in QD diode and results are presented.

5.1.1   Background information

An important information in many experiments on self-assembled InGaAs quantum dots is the interaction strength between the dots and a laser. This information is useful, in low temperature as well as room temperature regimes, and in nonlinear as well as linear absorption regimes [168; 169]. Quantum computing experiments, for example, deal with π pulses in order to make qubit flips and lower temperatures in order to take advantage of long dephasing times.

So far absorption measurements have proven very difficult to perform on dots, primarily due to the small net absorbance of a layer of dots at normal incidence, as also discussed theoretically in Chapter 4.

One way to overcome this problem is to embed quantum dots in a waveguide, where the interaction length is increased. However, this introduces a new problem, in that the input and output coupling are very difficult to determine.

Absorption of dots has been directly obtained by multi-bounce measurements [170]. In this case light that is coupled out of the waveguide is mixed with a gating pulse in a nonlinear crystal. By scanning the delay of the gating pulse, is possible to resolve the waveguide output and have information on gain. Pump-probe differential transmission experiments performed in heterodyne detection [149; 171; 172] also revel gain dynamics and saturation behavior of quantum dots.

But up to now, there are few investigations on nonlinear optics of QD samples with cw beam, probably because most researchers consider the case where excitation takes place via the wetting layer and not by optical excitation of the ground state. Important work has been done on gain saturation dynamics and filamentation characteristics of broad-area lasers based on quantum dot [134; 135; 173; 174; 175; 176].

The latter indicate that phase-amplitude coupling is in tendency lower in QD than in quantum well samples [177]. In addition, the physical processes involved are rather complicated and partially still unclear. Hence, it appears important, to perform first studies on saturation properties of QD samples with cw driving field.

Two kinds of samples has been investigated: one broad-area with tilted stripe and other with straight one. The advantage of the first is that the tilt of the stripe avoids back reflection from the facet. But after several experiments with different setup involving cylindrical optics to keep the coupling in the fast and slow axis constant and optimal, have proven very difficult and unsuccessful to couple light to these samples and hence to perform measurement. This reason has led us to turn the attention to samples with a straight stripe and a ridge waveguide.

5.1.2 Model of saturation of absorption and gain

Saturation of absorption (SA) takes place when the rate of generation of excited states is equal to the rate of its depletion by stimulated emission and excited state relaxation [143]. At sufficiently high incident light intensity, atoms in the ground state of a saturable absorber material become excited into an upper energy state at such a rate that there is insufficient time for them to decay back to the ground state before the ground state becomes depleted, and the absorption subsequently saturates [143; 145].

Saturable absorbers are also useful in laser cavities. The key parameters for a saturable absorber are its wavelength range (where it absorbs), its dynamic response (how fast it recovers), and its saturation intensity and fluence (at what intensity or pulse energy it saturates). They are commonly used for passive Q-switching.

The optical intensity variation of the laser beam propagating through a thin saturable absorber is governed by differential equation. Within simple model of saturated absorption, the relaxation rate of excitations does not depend on the intensity. Then, for the continuous-wave operation, the absorption rate (or simply absorption) is determined by intensity I [178], as discussed also in Chapter 3:

$$\frac{dI}{dZ} = -\alpha_{(I)}I \tag{5.1}$$

where I is the optical intensity and Z the propagation distance inside the sample. The variation of the absorption coefficient with intensity, in general, is expressed as [145; 179; 180]

$$\alpha_{(I)} = \frac{\alpha_{(0)}}{1 + \frac{I}{I_{sat}}} \tag{5.2}$$

where $\alpha_{(0)}$ is the low intensity absorption coefficient and I_{sat} is the saturation intensity.

A strong, narrow-band laser field saturates one segment of the inhomogeneous absorption profile (e.g., Doppler broadening), leading to decreased absorption. Malcuit et al [181] proposed the following equation for this kind of inhomogeneous saturation:

$$\alpha_{(I)} = \frac{\alpha_{(0)}}{(1 + \frac{I}{I_{sat}})^{1/2}} \tag{5.3}$$

An other model was proposed by Samoc et al [182] :

$$\alpha_{(I)} = \frac{\alpha_{(0)}}{1 + (\frac{I}{I_{sat}})^{1/2}} \tag{5.4}$$

Saturation of absorption, which results in decreased absorption at high incident light intensity, competes with other mechanisms (for example, increase in temperature, formation of color centers, two photon absorption, etc.), which result in increased absorption [183; 184; 185]. In particular, saturable absorption is only one of several mechanisms that produce self-pulsation in lasers, especially in semiconductor lasers [186].

5.2 Saturation of gain in InAs quantum dots

In order to obtain absorption and gain information on quantum dots, it is possible to utilize two equal quantum dot laser diodes, and use one configured with feedback as source (master) and couple the light into the other (slave). The slave can be used for measurements in absorption and gain, the latter achievable increasing the current with a current driver. This will be the topics of next section.

5.2.1 Experimental setup

The setup utilized for the experiment is the following showed in Fig. 5.1. The laser used for injection is a quantum dot edge-emitting diode from Innolume GmbH with a length of L = 4 mm and a stripe width of w = 5 μm. The structure is similar to that used in Chapter 2, section 2.4.1. The front facet reflectivity is of order of 1 % and the back facet reflectivity is 99 %. The laser is mounted on a C-mount and the temperature is controlled by a Peltier element.

Feedback is provided in Littman scheme with a diffraction grating (DG) that has 1450 lines/mm. A Littrow scheme was also tested also yielding higher power and threshold reduction, which is in accordance with expectation but in Littrow configuration the beam position move over distance in position when wavelength

Figure 5.1: Experimental setup: quantum dot laser (QDL), mirror (M), diffraction grating (DG) , aspherical collimator (C1) (f = 3 mm), aspherical collimator (C) (f = 8 mm) , L1 (f = 50 mm), L2 (f = 200 mm), L3 (f = 50 mm), filter (D), Photodiode (Pd1,Pd2), Optical Spectrum Analyzer (OSA), beam splitter (Bs1, Bs2), L4 (f = 100 mm), L5 (f = 50 mm), L6 (f = 75 mm), filter (F).

is tuned, so it is not suitable for precision measurement over different wavelength. After the DG there are two lenses L2 and L3 to collimate and shape the beam and then an aspherical lens C1 of focal length 3.1 mm and numerical aperture NA = 0.68 to focus the beam into the other diode.

The slave diode used is the same one as the injected one, also temperature controlled. Two amplified InGaAs Pin photodiode (Hamamatsu-G8370-03) are used to record data through a National Instrument card (DAQ) controlled in real time with Labview. An InGaAs camera also monitors constantly the superposition of the two beams.

Fig. 5.2 shows the spontaneous emission spectra of the diode used as slave for several currents starting at I = 150 mA. The spontaneous emission spectra has a Half Width Half Maximum (HWHM) of 6 nm for current less than I = 500 mA, after that lasing emission took place. The PL has three lobes, first one centered at λ = 1220 nm, the second one to the gain peak, λ = 1235nm, and the last one at λ = 1245 nm.

There is no evidence of lasing emission from the first excited state (ES1) and
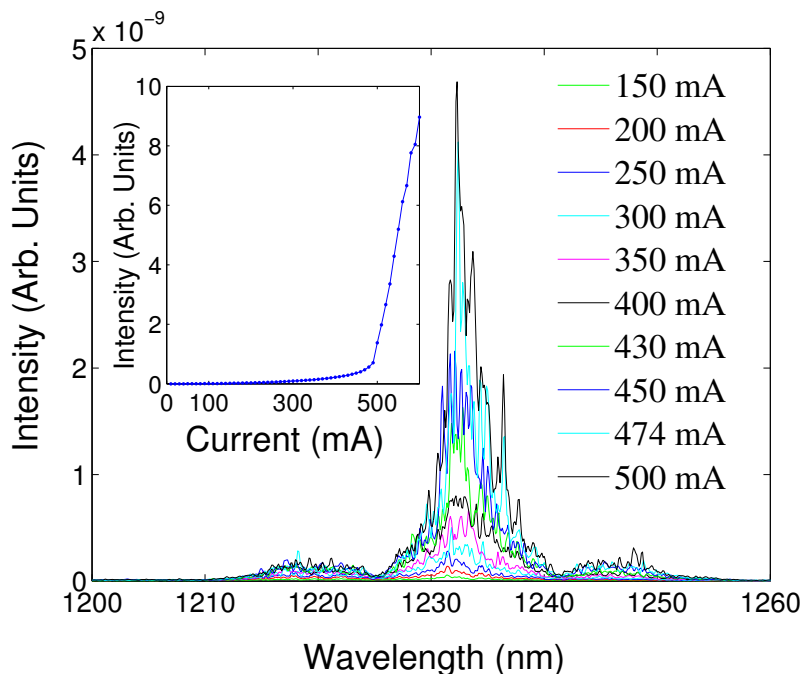
Figure 5.2: Spontaneous emission from the QDL diode, inset intensity vs current showing the threshold of lasing for the ground state of the diode.

from the wetting layer (WL) increasing the current until maximum current level. The inset of fig. 5.2 shows the LI-curve of the slave diode. The diode has a threshold current of I $= 500$ mA at T $= 14\,°$C.

5.2.2 Coupling to the waveguide

It is important for this experiment to have a good coupling into the waveguide due to the smallness of it. Indeed the beam radii of the mode intensity profile of the waveguide are $w_x = 3$ μm and $w_y = 0.6$ μm. To achieve the maximum coupling different method have been tried.

First has been looked with the camera, fig. 5.1, to see the overlap between the two beam: one of the (master) diode reflected by the (slave) diode and the one coming out from the slave itself. If they interact, the intensity of both beam should be more than the normal superposition of the two. Fig. 5.3 shows three different beams taken with the camera. Fig. 5.3(a) shows the reflection of the
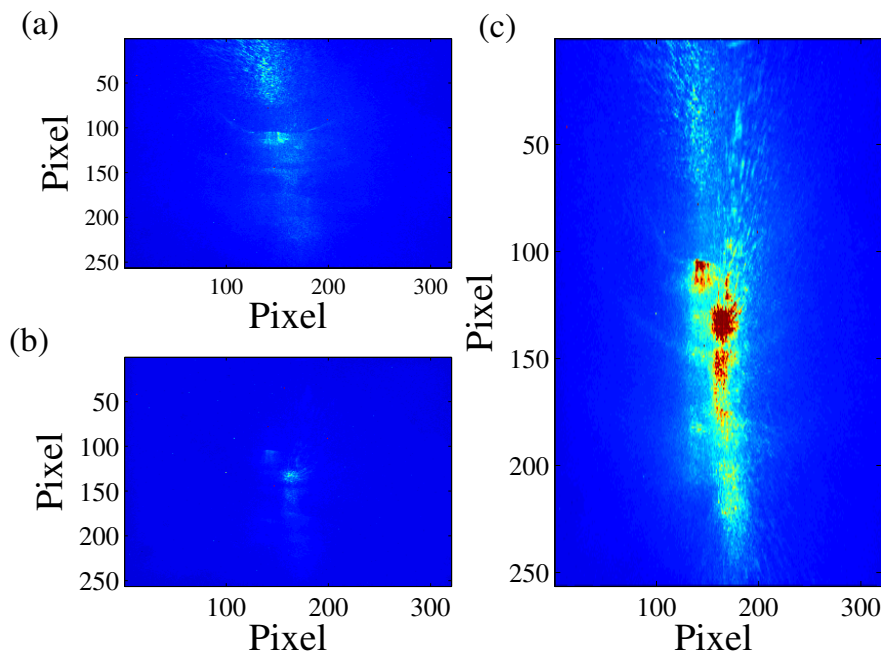
Figure 5.3: (a) Master diode beam reflected into the camera (b) Slave diode Photo-luminescence (c) Interaction of the two beams.

master from the slave diode. The beam is quite scattered basically due to the material interaction and dispersion. Fig. 5.3(b) shows an image of the slave diode when fixed at a current of I = 50 mA. Fig. 5.3(c) is taken instead when both, master and slave, are superimposed. It is possible to see that there is interaction, Fig. 5.3(c), due to the fact that there is more light when both are together than the sum of the two.

An other indication of interaction comes out looking at the amplified spontaneous emission spectra of the slave diode as it evolves increasing the injection power of the master diode. Fig. 5.4(a) shows a zoom of the optical spectra taken with the optical spectrum analyzer centered around the gain peak. The spontaneous emission spectra of the slave diode decrease with increasing injection current of the master diode due to depletion of carrier fig. 5.4(a).

It is possible to use the gain material of the slave diode to induce lasing and injection locking using only the master diode, as achieved in [187; 188; 189; 190].
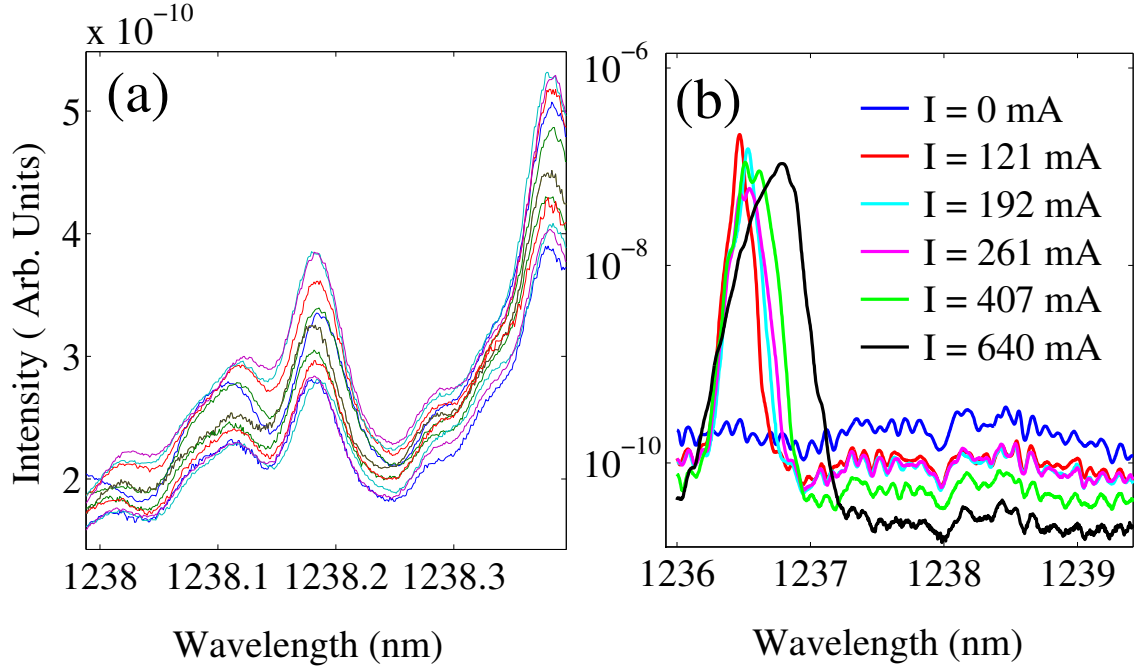
Figure 5.4: (a) Spontaneous emission spectra reduction as increase the pump power of the master diode (b) Slave lasing as increasing the master current.

Fig. 5.4(b) shows the evolution of the beam injected by the master diode, then reflected by the slave diode and recorded by the optical spectrum analyzer. At I = 121 mA lasing emission start to took place. Fig. 5.4(b) shows that the spontaneous emission decreases again as the injection increase.

Once there are all these good indications of coupling to the waveguide, the final adjustments come out looking at the signal on the output detector and precisely adjusting the beam path with hight precision translation stages in such a way to maximize the amplification of the overlap.

5.2.3 Experimental results

Measurements have been taken, at fixed wavelength of the master diode, tuning the current of the diode, and recording the input signal on the first photodiode (PD1) and the one reflected by the second diode on the output photodiode (PD2), ref. Fig. 5.1. After the data have been taken, through Labview programme, it is
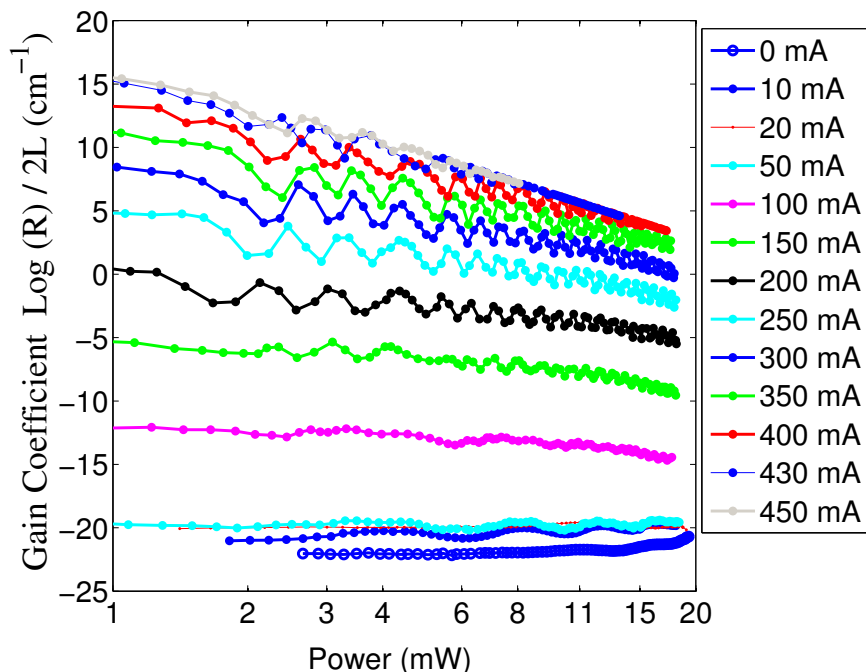
Figure 5.5: Gain coefficient as function of power for increasing current at λ = 1240 nm. The ripple present in the graph are probably due to the fact that the laser hits resonance.

possible to analyze and calibrate the signal according to the gain setting of the detectors (four stage possible) and the splitting ratio present in the setup. To get a better resolution in the measurements and good signal to noise ratio we increase the sensitivity of our detectors especially at lower power level, i.e. curve without current and low current one. Also in the measurement with fixed current of the slave diode it is removed the offset due to the spontaneous emission of the sample in the output detector.

Once calibrated the data it is possible to calculate the gain coefficient expresses as $1/2L \log(I_{out}/I_{in})$ where I_{out} is the signal in the output photodiode and I_{in} is the signal of the input photodiode, L = 4 mm is the length of the diode.

We use 2 in the expression of the gain coefficient case due to the fact we initially consider that cavity effect can be important especially close to threshold and the system can be considered as two-pass amplifiers. All the measurement are not calibrated for the coupling efficient. Indeed was very demanding to have

an idea of the coupling to the waveguide of the sample.
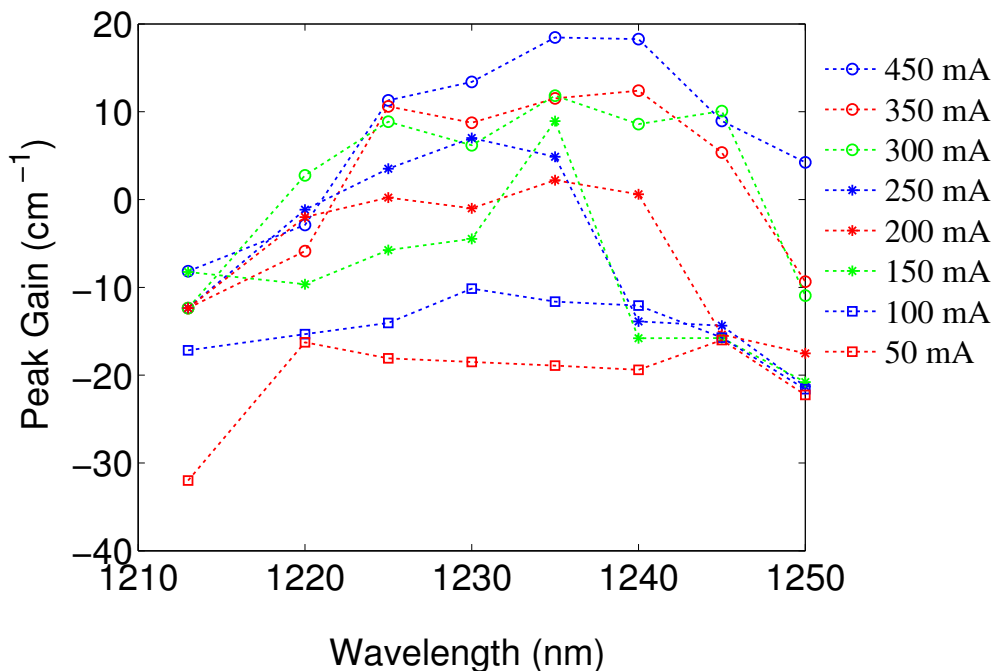
Figure 5.6: Maximum gain as function of wavelength for increasing current.

Fig. 5.5 shows how the gain coefficient changes as function of injected power of the diode for increasing current. The current of the master diode is increased in steps of 1 mA from threshold up to 1000 mA, with a delay between each data of 2 second. The wavelength of the injected beam is fixed in this case at λ = 1240 nm. Without current in the slave diode, it possible to see that the small-signal gain coefficient is fixed at constant value of -24 cm^{-1} increasing slightly at injected power level above 14 mW, an indication of nonlinear transmission and saturation of absorption.

The small-signal gain increases for increasing current of the slave diode, as expected [191; 192]. At higher current, still below the threshold of the laser, the gain coefficient is almost constant and doesn't change, also reported in [193; 194]. For higher current, below lasing condition, is possible to notice that the gain coefficient saturates for higher injection power.
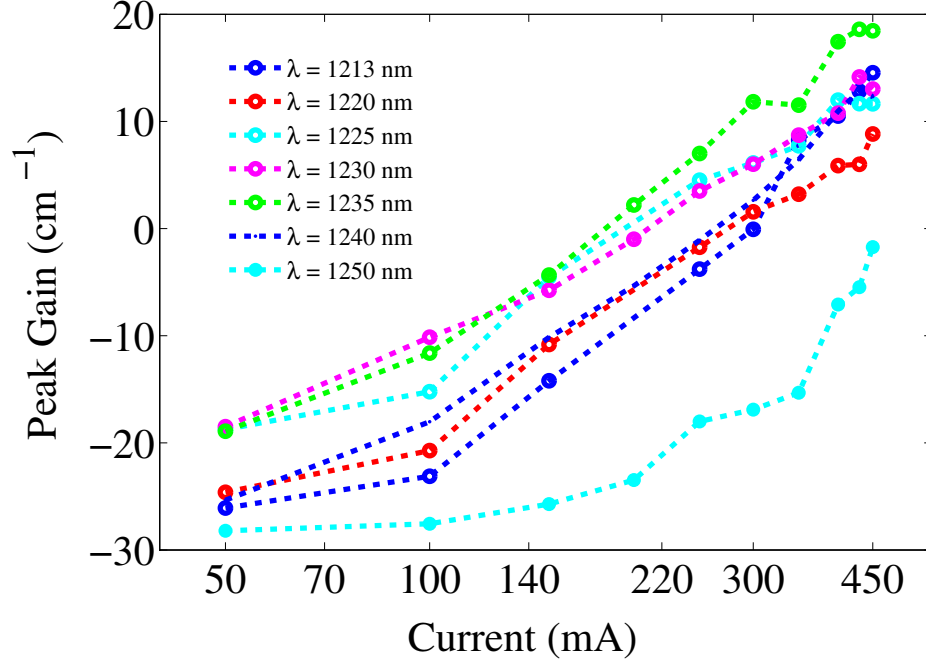
Figure 5.7: Gain peak as function of increasing current for different wavelength.

Fig. 5.6 shows the peak small-signal gain achievable by the system as function of wavelength for different current level. The peak gain increase with increasing current and is more relevant at wavelength around $\lambda = 1230-1235$ nm as expected from the PL.

Fig. 5.7 shows the evolution of the gain peak as function of current for several wavelength starting at $\lambda = 1213$ nm up to $\lambda = 1250$ nm. For low current levels the gain is quite constant at fixed value depending on the wavelength. Then it increase linearly for increasing current up to reach a constant value at higher current. After that the gain stay constant and increasing more the current lasing emission took place.

5.2.4 Saturation of gain

It is possible to fit the gain coefficient, for the various wavelengths, following nonlinear fit model as discussed in section 5.1.2.
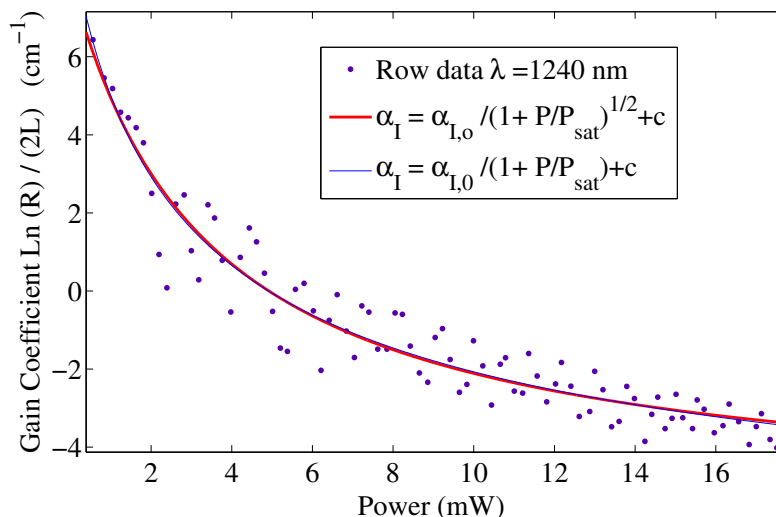
Figure 5.8: Saturation of gain with fits, I = 350 mA.

Fig. 5.8 show raw data and fit of the dependence of the gain coefficient on power with two different models that describe saturable absorption in the case of two-level systems with inhomogeneous, $\alpha_I = \alpha_{I,0}/\sqrt{(1 + P/P_{sat})}$+c and homogeneous, $\alpha_I = \alpha_{I,0}/(1 + P/P_{sat})$+c, broadening [144] with $\alpha_{I,0}$ the small signal absorption coefficient. The fit parameter used are $\alpha_{I,0}$, P_{sat} and c.

Both prove to fit the data well. This can be due to the small scale on the x-axis, indeed the windows where the data are present is not enougth large to give sufficient information on what model fit better.

Fig. 5.9(a) shows how the gain coefficient change as function of wavelength. It has been taken for a fixed current of I = 350 mA, quite below the threshold of the laser, see inset of. Fig. 5.2.

Fig. 5.9(b) shows instead how the saturation power change as function of wavelength. It is almost constant to 10 mW to decrease to 5 mW at $\lambda = 1240$ nm and then to increase again for $\lambda = 1250$ nm.

Fig. 5.9(c) shows the transmission loss, c parameter of the fit, as function of wavelength. They are constant around -5 cm^{-1} until $\lambda = 1240$ and then decrease.
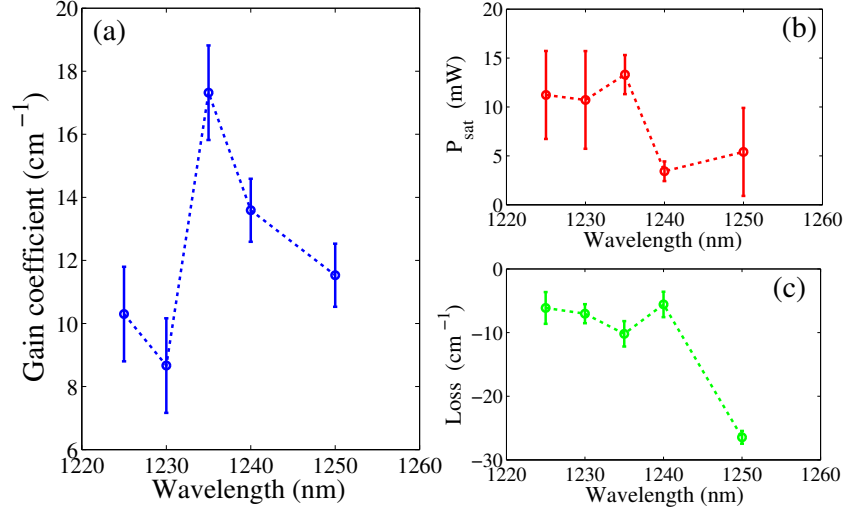
Figure 5.9: (a)Gain coefficient as function of wavelength at I = 350 mA (b) Power saturation as function of wavelength (c) Losses as function of wavelength.

5.3 Analytical Model

It is useful to analyze the resonance properties of a plano-planar Fabry-Perot cavity driven by a plane monochromatic scalar light field. Hence cavity effect in spite of AR coatings are important to address.

5.3.1 Airy function

We are considering an etalon as show in Fig. 5.10. The round trip phase shift is given by [195]:

$$\Delta\Phi = 2n_b L \cos\theta \frac{2\pi}{\lambda_0} \tag{5.5}$$

where L is the length of the cavity, n_b is the refractive index of the material inside the cavity, n_l is the refractive index of the material outside the cavity, θ is the angle of the incoming beam with the normal, λ_0 is the wavelength of the light. The reflected field is given by:
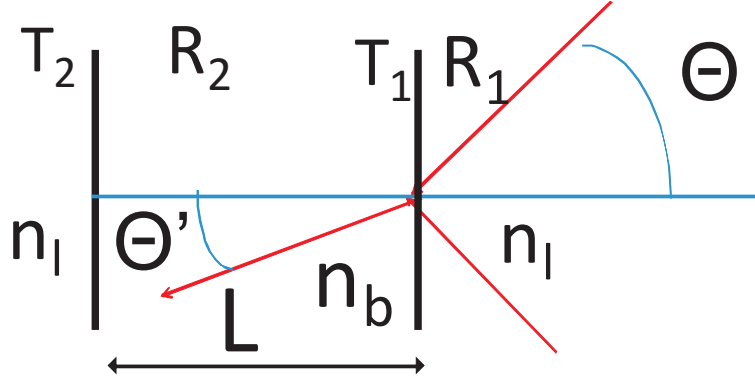
Figure 5.10: Schematic of the Fabry Perot cavity: angle of incidence (θ), is the length of the cavity (L), refractive index of the material (n_b), refractive index outside the material (n_l), reflectivity of the first and second mirror (R_1, R_2), transmission of the in coupling and out coupling mirror (T_1, T_2).

$$A_R = A_0 \sqrt{R_1} \frac{-1 + R_{eff} e^{-i\Delta\Phi} + \frac{T_1}{R_1} R_{eff} e^{-i\Delta\Phi}}{1 - e^{-i\Delta\Phi} R_{eff}} \tag{5.6}$$

where R_1 is the power reflectivity of the in coupling mirror, R_2 is the power reflectivity of the out coupling mirror, T_1 and T_2 respectively are the power transmission of the in coupling and out coupling mirror. R_{eff} is the effective reflectivity $R_{eff} = \sqrt{R_1 R_2} V$ with $V = e^{-2\alpha_i L}$ and $1 - V$ are the fractional losses for field during round trip. α_i are losses for field per unit length within the cavity.

The reflected intensity is:

$$I_R = |A_0|^2 R_1 \frac{(1 - R_{eff})^2 + 4R_{eff} \sin^2 \frac{\Delta\Phi}{2} + 4\frac{T_1}{R_1} R_{eff} \sin^2 \frac{\Delta\Phi}{2} + \frac{2T_1}{R_1} R_{eff}^2 + (\frac{T_1}{R_1})^2 R_{eff}^2}{(1 - R_{eff})^2 + 4R_{eff} \sin^2(\frac{\Delta\Phi}{2})} \tag{5.7}$$

The reflected field is a superposition of the transmitted intra-cavity field in forward direction and the reflection at the first surface. In transmission the field is given by:

$$A_T = A_0 \sqrt{T_1 T_2 V} \frac{e^{-i\Delta\Phi_1}}{1 - R_{eff} e^{-i\Delta\Phi_1}} \tag{5.8}$$

where

$$\Delta\Phi_1 = \frac{\Delta\Phi}{2} \tag{5.9}$$

describes the phase shift the field is accumulating during one passage through the resonator. The transmitted intensity is given by:

$$I_T = |A_0|^2 \frac{T_1 T_2 V}{(1 - R_{eff})^2 + 4R_{eff} \sin^2 \frac{\Delta\Phi}{2}} \tag{5.10}$$

It is proportional to the intra cavity intensity

$$I_C = \frac{I_T}{T_2} \tag{5.11}$$

5.3.2 Results

It is possible to solve the above equation and get an idea on how the gain coefficient evolve as function of transmission and reflection.
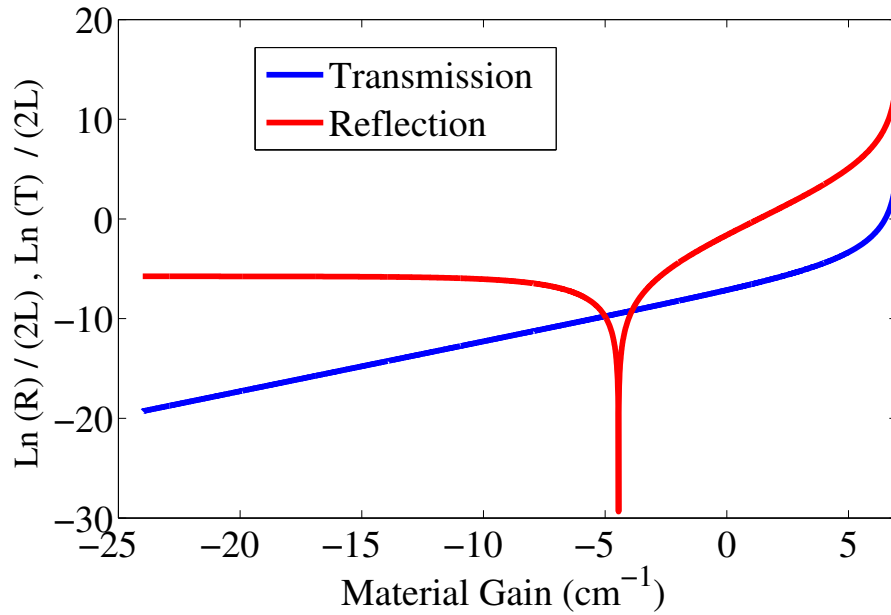
Figure 5.11: Ln (R) / (2L) and Ln (T) / (2L) as function of material gain for transmission (blue curve) and reflection (red curve) in a Fabry-Perot cavity.

Fig. 5.11 shows how the ln(R) as function of material gain for transmission and reflection. The parameter used are in the table 1.1.

The starting value of the curve corresponding to the reflection is given by ln(R1) / 2L = -5.76. The curve stay constant to that value until impedance matching is achieved. Impedance matching is for $V^2 R_2 = R_1$. From Fig. 5.11 it is where the reflection curve has a dip to - 24. After that the curve goes up and the region relevant to the experiment discussed in the previous section corresponds to the starting of modal gain of 4 up to 7. After that the emission took place.

The curve of Fig. 5.11 can be read as variation of gain and absorption as increasing current or, at constant current, changing modal gain due to saturation.

In transmission, blue curve of Fig. 5.11, it is possible to see the ln(T) change linearly with the material gain, but in this case we don't have access to the output facet due to the HR coating.

Table 5.1: Value of the parameters used for the simulation

Parameter	name	Value
Reflectivity of in coupling mirror	R_1	0.01
Reflectivity of out coupling mirror	R_2	0.995
Background losses intensity	$2\alpha_i$	1.3/cm
Cavity length	L	4 mm

5.4   Discussion

The results present in this section are in agreement with gain measurement [147; 149; 161; 194; 196] and theoretical result on gain saturation [64; 197]. The modal gain of semiconductor materials usually has been be obtained using Hakki-Paoli technique [198] or the Henry technique [199]. Gain of the quantum dot material can be obtained also following the multi-section method of Thomson et al. [200].

Mi [193] find peak modal gains as high as 19 cm^{-1} per QD layer measured in 1.1μm in p-doped QD laser heterostructure. The higher value of gain, compared with that of conventional QD lasers, is attributed to minimization of hot carrier effects and a decrease of dot excited states and wetting layer occupation.

Salhi [194] find also that the modal gain increases linearly with the number of QDs layers and reaches a value of 25 cm^{-1} for devices containing 5 QDs layers which corresponds to 5 cm^{-1} per QDs layer.

5.5 Saturation of absorption and nonlinear index shift in InAlAs QD

In this section we report on measurement on saturation of absorption and nonlinear refractive index of InAlAs quantum dot samples. These samples are different from the previous one in composition and emission wavelength. There is no excited states. Also they are investigated with a well established tunable and hight power laser source, in this case Ti-Sapphire that will allow measurement in transmission.

5.5.1 Sample and Experimental setup

The sample was grown at Laboratory Physics Nanostructure (LPN-Paris) [201] and is made of 5 layers of InAl$_{0.33}$As quantum dots on As matrix on a substrate of GaAs tailored for emission at 780 nm (see Fig. 5.12 for photoluminescence curve for a similar sample). Inside the sample a two-dimensional single-mode waveguide is fabricated.

The facets are not coated and hence form a low Finesse resonator. The free spectral range of the cavity is 0.0419 nm assuming a refractive index of n$_b$ = 3.51 and a length of the sample of L $\approx$ 2.1 mm.

The experimental setup is show in Fig. 5.13. The laser utilized is a cw Ti:Sapphire emitting at 780 nm. Part of the beam coming out from the laser is sent to a wavemeter (WA-1100) and the main part (90 %) is sent to an optical isolator to prevent feedback from the optics, (Fig. 5.13).

After passing the isolator the beam is sent to a telescope and then to an acousto-optic modulator (AOM). Two modulated beams are coming out from the AOM, from those the first modulated one is used. The beam is coupled to a single-mode fiber. The peak power coupled power to the single mode fiber is around 50 mW.
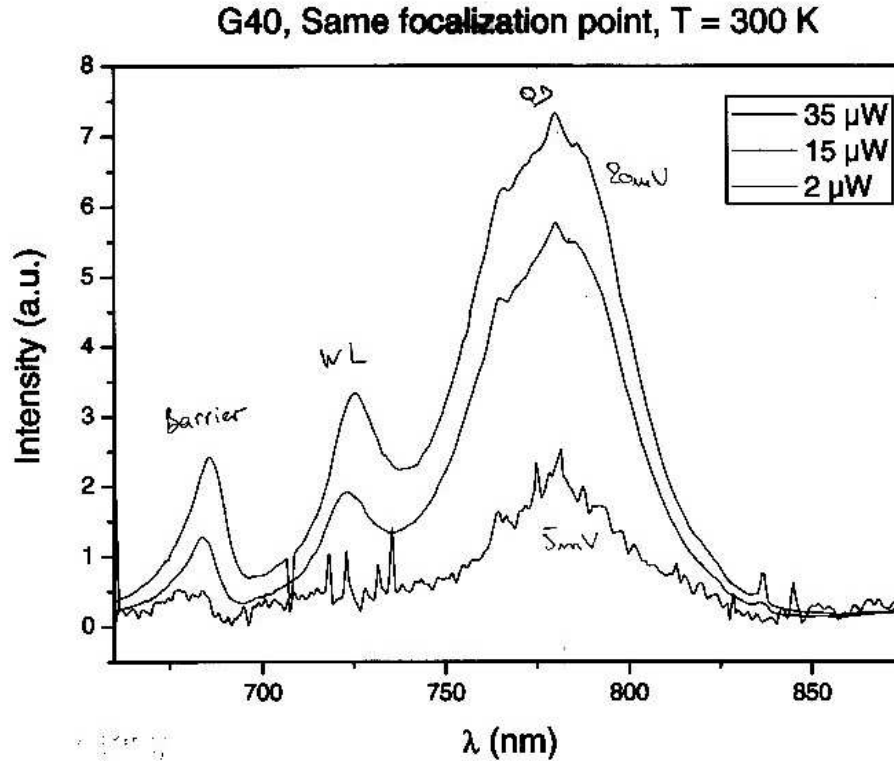
Figure 5.12: Spontaneous emission spectra of a typical InAlAs QD structure. Courtesy of R. Kuszelewicz.

After the single mode fiber there is a polarization control single mode fiber which enable to select the polarization of the incoming beam.

This is connected to a fiber coupler that splits the incoming beam in 10% and 90%. The weak part of the beam is sent to the input photodiode (Pd1).

The main part (90 %) is connected to a single mode fiber with a lensed output end. The tapered fiber has a focus spot size of 2 μm and a working distance of around 40 μm. So from this value appear to be crucial the position of the fiber. Indeed the Rayleigh length is $z_r = (\pi\omega_0^2)/\lambda = 16.11$ μm. Hence accuracy precision is crucial and is made with a high-precision xyz-translation stage. The light transmitted is collected by a microscope objective (Mo2, 10x, f = 8 mm) also positioned on a xyz-translation stage. A 50/50 beam splitter positioned after sent part of the beam to a camera and the other part to the output photodiode (Pd2). A mirror also is located above the sample to collect light from a lamp
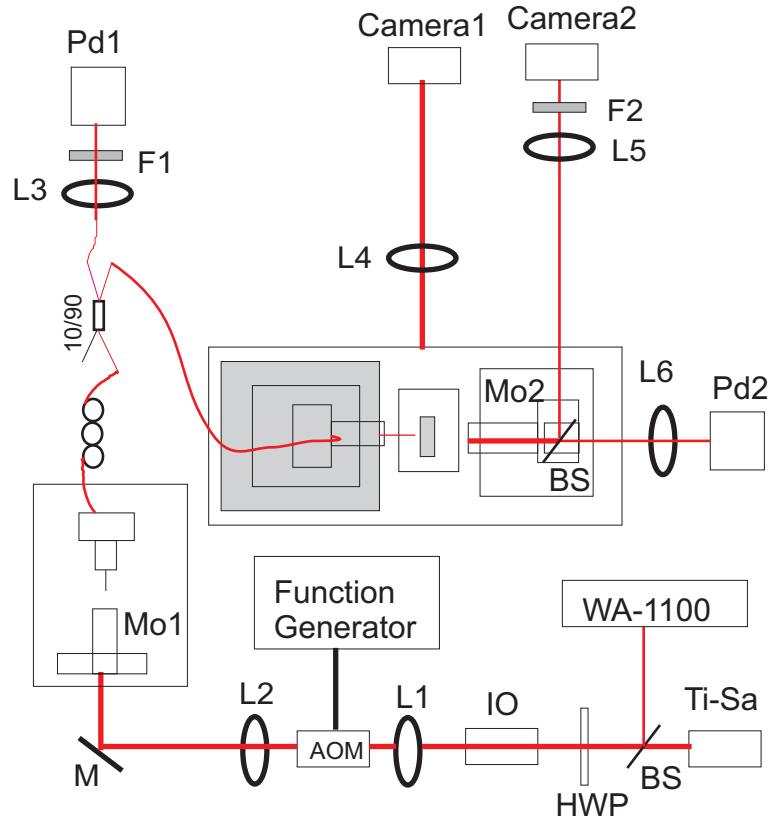
Figure 5.13: Experimental setup: Ti:Sapphire laser (Ti-Sa), beam splitter (BS), Half wave plate (HWP), Wavemeter (WA-1100), Optical Isolator (IO), L1 (f = 10 mm), L2 (f = 10 mm), acusto opto-modulator (AOM), Microscope Objective (Mo1,Mo2), L3 (f = 35 mm), mirror (M), Filter (F1,F2), L4 (f = 50 mm), L5 (f = 35 mm), L6 (f = 35 mm), L7 (f = 35 mm), filter (F1, F2), Photodiode (Pd1, Pd2).

that has been reflected by the sample and sent to a second camera situated close to the other one.

The temperature of the sample is kept fixed at 15 °C with resolution of 0.01 degree level by a temperature controller (Thorlabs-TED350).

5.5.2   Control of the laser system

The wavelength of the Ti-Sapphire laser is controlled by a Lyot filter in combination with an etalon. Labview programme simultaneous adjust these.
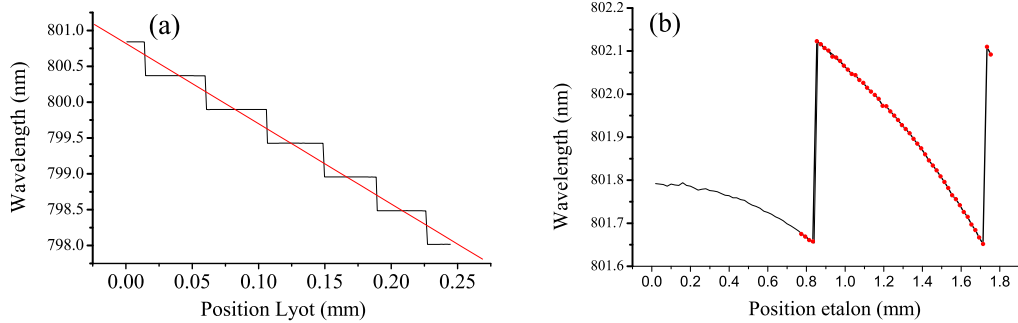
Figure 5.14: (a) Lyot filter calibration, (b) Thin etalon calibration

Lyot and etalon are controlled by a motion controller driver (ESP 3000 Newport). The combination of these two filters results in only one longitudinal mode of the laser favorable and in a tunability of wavelength of the laser. The Lyot filter changes the wavelength of the laser by several nanometers, Fig. 5.14(a), while the thin etalon is for fine tuning the wavelength of the laser, Fig. 5.14(b).

Fig. 5.14(a) shows a typical calibration curve of the Lyot filter obtained moving the motor with the Labview programme. The shift in wavelength as function of position is not linear but proceed in steps each one of 0.025 mm. After each of this steps the laser moves to the successive wavelength, while staying constant in the range. From fig. 5.14(a) it is possible to infer that to move the Ti-Sa by 2 nm the position of the Lyot has to move of 0.25 mm.

Fig. 5.14(b) shows instead the calibration of the thin etalon. In this case the excursion where it is possible to move, without jumping, the thin etalon is of 0.45 nm in 0.7 mm movement of the motor corresponding to resolution of the thin etalon of 1 pm, also the resolution of the wavemeter used to read the wavelength of the laser. The excursion of the etalon follows a cosine formula, to repeat again after 1 mm.

So moving the thin etalon, for fixed position of the lyot filter, is possible to shift the wavelength position of the laser by a few angstroms with a good resolution (± 1 pm). Each time the wavelength is shifted the Lyot filter need to be calibrated in position due to the fact that Lyot and etalon are correlated.

5.5.3 The imaging system and waveguide coupling

It is important to couple the beam coming out from the single-mode lensed fiber into the waveguide of the sample with good efficiency. This is made by looking at the sample with two cameras, Fig. 5.15. The first camera is taking real time images looking from the top of the sample, Fig. 5.15(a). The second camera is taking images from the rear of the sample, Fig. 5.15(b).

The sample is illuminated with a high intensity fiber coupled light source (Thorlabs OSL1). From that it is possible to build an image into the two camera following the two configurations, Fig. 5.15. In the first one, the light reflected
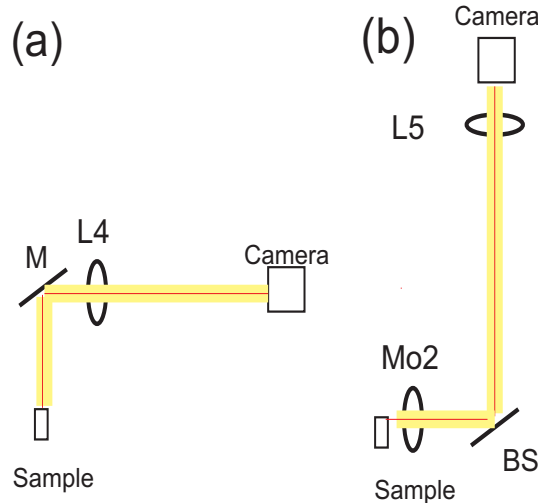
Figure 5.15: (a) Side view of the system for imaging top view (b) Side view of the system for imaging the exit facet.

by the sample is collected by a mirror positioned on the top of the sample and then a lens L4 (f = 200 mm) image it on to a camera. It is also possible to solve the ABCD matrix of the system for the two configuration to calculate the size of the image and the distance where it forms. The image after the final lens for the configuration (a) is at d = 825.05 mm with a magnification of M = -10.

Fig. 5.15(b) shows the imaging system used from the rear of the sample. In this case it is possible to look directly at the sample side and to view the transmitted mode of the waveguide. Again before to shine the laser into the sample an image

is construed with the lamp. The calculated image after final lens is at distance of d = 233.9 mm and with a magnification of M = -1.49.

Hence it is possible to record and look in real-time at the images of the coupling with two monitors. From the top view we see the location inside the sample of the waveguides, (Fig. 5.16-left), so it is possible to position the tapered lensed fiber at a correct distance from the sample. Fig. 5.16-left shows the image of the light reflected from the sample. It is possible to spot the three waveguide inside the sample and the tips of the tapered fiber.

Instead looking from the back, it is possible to position the tapered lensed fiber in the other two directions.
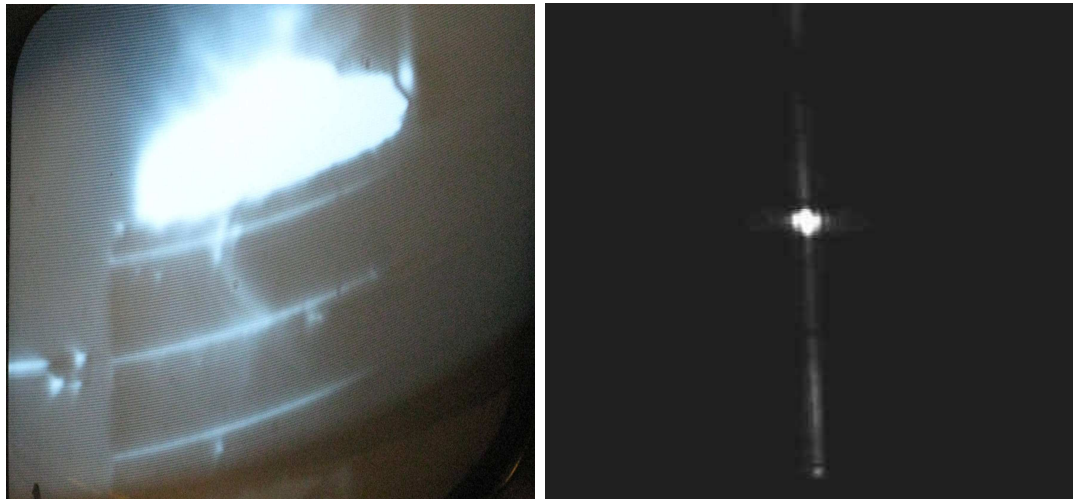
Figure 5.16: (Left-Image) Top view were is possible to spot the three waveguide, (Right-image) Rear facet of the sample.

Fig. 5.16-right shows instead the mode of the waveguide in transmission. Both information are important due to the fact that is very easy to loose coupling to the waveguide due to the smallness of it.

5.5.4 Results

The system is suitable for absorption measurements. Indeed due to the AOM there is a signal modulated in power so there is no need to change the power of the laser.
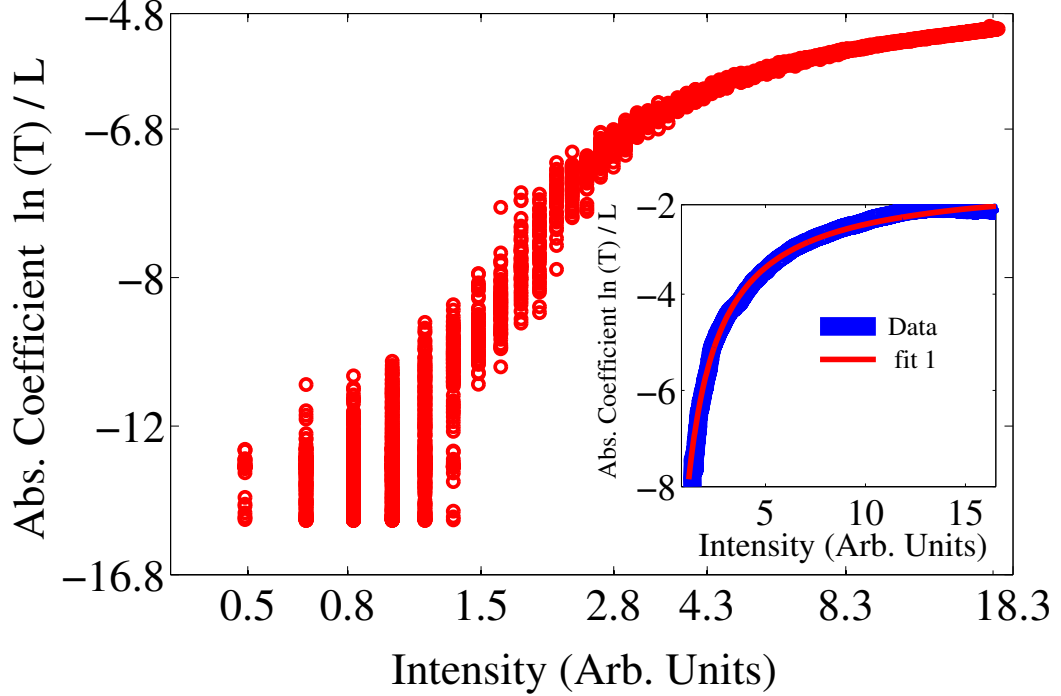
Figure 5.17: Plot of the transmission as function of wavelength for different input intensity, inset smoothing curve and nonlinear fit.

Fig. 5.17 shows the absorption coefficient in dependence of the input intensity for the gain peak ($\lambda = 789$ nm). It starts at the small-signal value and then drops to the value given by the non saturable losses due to the generation of carriers and the resulting bleaching.

We fit the dependence of the gain coefficient on intensity with different models that describe saturable absorption in the case of two-level systems with inhomogeneous, $\alpha_I = \alpha_I / \sqrt{(1 + P/P_{sat})} + c$ and homogeneous, $\alpha_I = \alpha_I / (1 + P/P_{sat}) + c$, broadening [144]. Both proves to fit well the data, inset of Fig. 5.17 as the case of section 5.2.4. From the coefficient of the fit is possible to recover the relevant parameter. The absorption coefficient is of 21.4 cm^{-1}. This will led to an absorption for QD layer of 4.27 cm^{-1}. The saturation power is of 8 mW.

5.5.5   Nonlinear index shift

A linear ramp was applied to the acusto-optical-modulator (AOM) to ramp the incident power. Keeping the position of the Lyot filter fixed the thin etalon was moved by steps of 0.05 Angstrom. At each step the readings of both photodiodes (before and after the sample) are recorded together with the wavelength measured by a wavemeter (WA-1100). Data were taken around the gain peak of $\lambda = 786\ nm$.

Each measurement, within a scan of a free spectral ranges of the sample, is quite demanding cause the Ti:Sapphire has some power fluctuation resulting in jumps in the wavelength reading of the laser. Sometimes, tuning the wavelength, the lasers is spontaneously jumping to a wavelength different to the desired one. So collecting a complete set of measurements took some times.
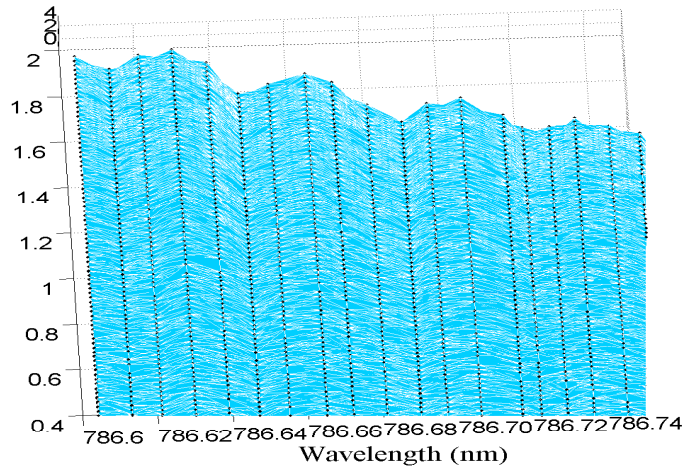
Figure 5.18: Plot of the transmission as function of wavelength for different input intensities.

Fig. 5.18 shows a 3D plot of transmission as function of input intensity for different wavelengths. There are regular ripples (peaks and dips) in transmission if the wavelength is scanned around 786 nm. These regular modulations are present only at $\lambda = 786$ nm and not at other wavelengths. The ripples are superimposed over a long scale modulation.
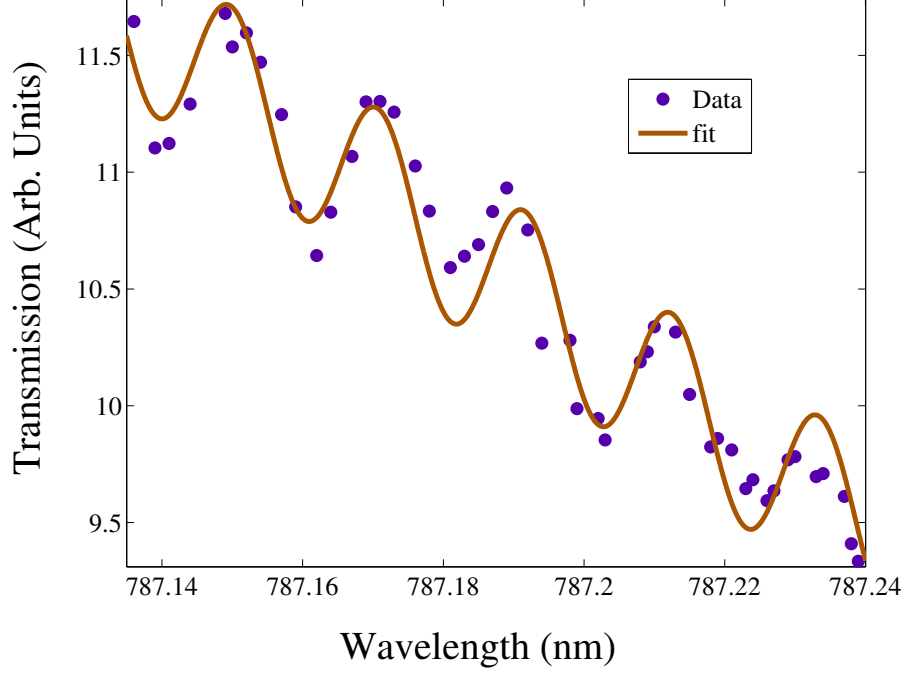
Figure 5.19: Plot of the transmission as function of wavelength for different input intensity.

Fig. 5.19 shows a cut through the 3D plot showing how transmission behaves as function of wavelength. It display also a fit to the function $y(x) = ax + b + c\cos(dx + e)$.

From the coefficient of the fit is possible to infer the periodicity of this ripples. The periodicity is of T = 0.049 nm

This leads to an effective group index of $n_b = 3.01$ according to the equation

$$n_b = \frac{\lambda^2}{2LT} \tag{5.12}$$

where L≈ = 2.1 mm is the length of the sample. This support the interpretation that are longitudinal modes of the cavity.

If there were a nonlinear index shift, the peaks should be shifted as function of the input intensity. It is not possible to see any shift of the modes by increasing the input power in Fig. 5.19.

The reason is that the nonlinear effect is expected to be stronger at the wings

of the photoluminescence curve (Fig. 5.12) and hence not pronounced in the gain peak. Also in absorption is quite difficult to observe nonlinear index shift as will be discussed later.

It is very demanding to detune this particular Ti-Sa over a large wavelength and for this reason are not presented data for wavelengths far from the running wavelength of the laser where a hight nonlinear shift is expected.

5.6 Broad-area quantum dot sample

So far, coupling light to quantum dots embedded in a waveguide has been very difficult and a tedious procedure to address. It is more difficult coupling to light to a single-mode fiber that has the dimension of a waveguide, typically $w_x = 0.6$ μm and $w_x = 3$ μm. All the measurement so far also show that is quite easy to loose coupling in the waveguide and hence the alignment need to be redone for each measurement.

To avoid the complexity of measuring the gain, we developed a new technique based on coupling a single mode fiber the light coming of a quantum dot sample sample and retro-inject again with the same fiber back the light from a laser source.

It is possible to see directly how much light is couple into the fiber. The same amount of light that should couple back into the active area of the sample and hence the waveguide if the source is injected from the other end of the fiber. The following sections describe two experiment based on this principle.

5.6.1 Sample and experimental setup

The setup utilized is the following showed in Fig. 5.25. The quantum dot sample (QDS) is from Innolume GmbH with a length of L = 1.5 mm. It contains 15 layer of InAs QD in a GaAs matrix. It is designed to be broad area (130 μm). The layer structure specification is given in Fig. 5.20. The laser source is a commercial tunable source (TSL-1210). Both facet of the QDS are anti-reflection (AR) coated. The sample is mounted on a specific mount. It possible to inject

Product:										DO2283		

Layer	Material	Group	Repeat	Mole fraction (x)		Thickness	Doping profile		Type	Dopant
				start	finish	(nm)	start	finish		
12	GaAs					200	1e20		P	C
11	Al(x)Ga(1-x)As			0.15	0	15	1e19		P	C
10	Al(x)Ga(1-x)As			0.15		1800	5e17		P	C
9	Al(x)Ga(1-x)As			0.15		700	2.5e17		P	C
8	GaAs	1	15			35			U/D	None
7	In(x)Ga(1-x)As	1	15	0.15		5			U/D	None
6	InAs *	1	15			0.8			U/D	None
5	GaAs					35			U/D	None
4	Al(x)Ga(1-x)As			0.15		1000	5e17		N	Si
3	Al(x)Ga(1-x)As			0.15		1500	1e18		N	Si
2	Al(x)Ga(1-x)As			0	0.15	15	3e18		N	Si
1	GaAs					500	3e18		N	Si
0	GaAs substrate			N+ GaAs 3 inch						

Figure 5.20: Layer structure specification.

current through it by probe tips of 6μm appositely positioned. The temperature is controlled by a Peltier element. All the setup is on a suspended table.
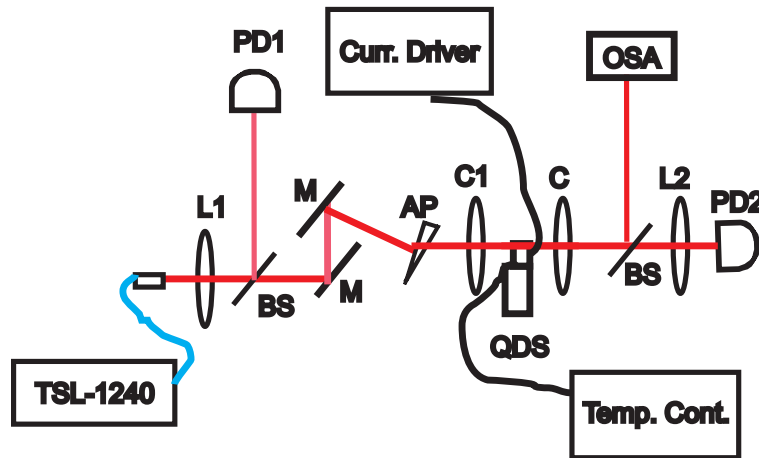
Figure 5.21: Experimental setup: Tunable laser (TSL-1240), L1 (f = 20 mm), beam splitter (BS), mirror (M), anamorphic prism (AP), C1 (f = 3.1 mm), quantum dot sample (QDS), C2 (f = 8 mm), Optical Spectrum Analyzer (OSA), L2 (f = 50 mm), Photodiode (PD1, PD2).

The beam emitted by the quantum dot sample is collimated using an aspherical collimator (C1) of 3.1 mm focal length and numerical aperture NA = 0.68. Due to the fact that the beam after the lens C1 is still quite asymmetric in the horizontal direction an anamorphic prism is settled to shape the beam in a way

to be more circular. Also has been tried an anamorphic prism pair but that did not improve the system. After passing two steering mirror, the beam reaches a lens (L1) of focal length 20 mm.

Then the beam is coupled into the single mode fiber. After obtained the maximum coupling to the fiber we connect the single mode fiber to the tunable source. In this way we sent the beam to the QDS sample. In the other side of the QDS we collect the beam transmitted by the sample with an aspherical lens (f = 8 mm) and a photodiode and optical spectrum analyzer (OSA) are used for the detection part.
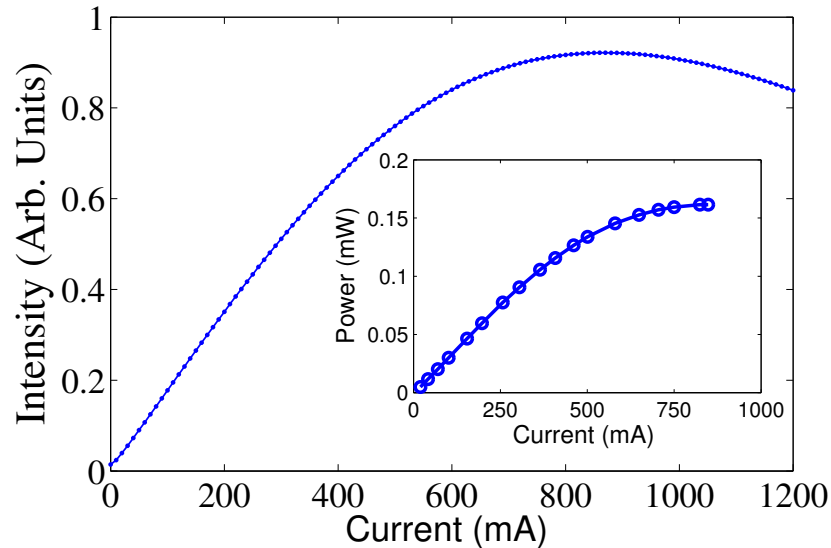
Figure 5.22: Light-current of the diode, inset power as function of current

Fig. 5.22 shows the LI curve for the QD sample. It shows that the intensity increases linearly as function of current until it reaches 500 mA where the output intensity saturates and then for higher current the output intensity drops mainly due to heating induced by the current.

The inset of fig. 5.22 shows instead the power available as function of current. The power reach a maximum of 0.15 mW at 650 mA to stay constant after that. There is no lasing emission from the sample.

Fig. 5.23 shows instead the evolution of the peak of the spontaneous emission, and of the peak intensity as function of current for three different temperatures.
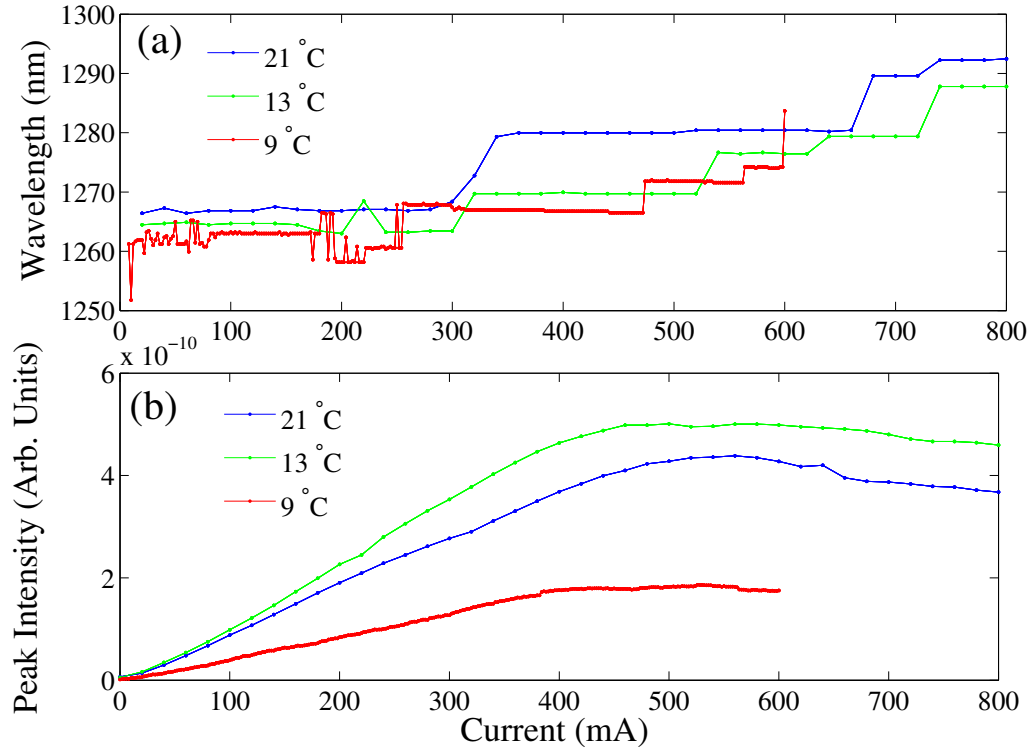
Figure 5.23: (a) Wavelength shift of the peak of the photoluminescence as function of current for three different temperature (b) Peak intensity as function of current for three different temperature.

Fig. 5.23(a) shows that increasing the temperature from T = 9 °C to T = 21 °C the peak of the PL move from $\lambda = 1262$ nm to $\lambda = 1266$ nm, a shift of 0.333 nm/K.

With increasing current, the peaks of PL stay constant until they reach some temperature where they jump to an other wavelength. This jump seem to appear earlier at lower temperatures than at higher ones.

Fig. 5.23(b) shows instead how the peak intensity evolve as function of current for three different temperature. Increasing the current, the peak intensity increases linearly until it reaches a maximum, and then decreases again, following the LI-curve.

5.6.2 Spatial profile and waveguide coupling

Fig. 5.24 shows the image of the emission of the sample taken with a GaAs camera at 940 mm from the sample, in imaging condition, i.e focusing onto the camera. From the data is possible to infer the beam width in both direction of the beam. The vertical width is of $\omega_y = 0.8 \ \mu$m and the horizontal is $\omega_y = 15 \mu$m, 18 times bigger than the other direction.
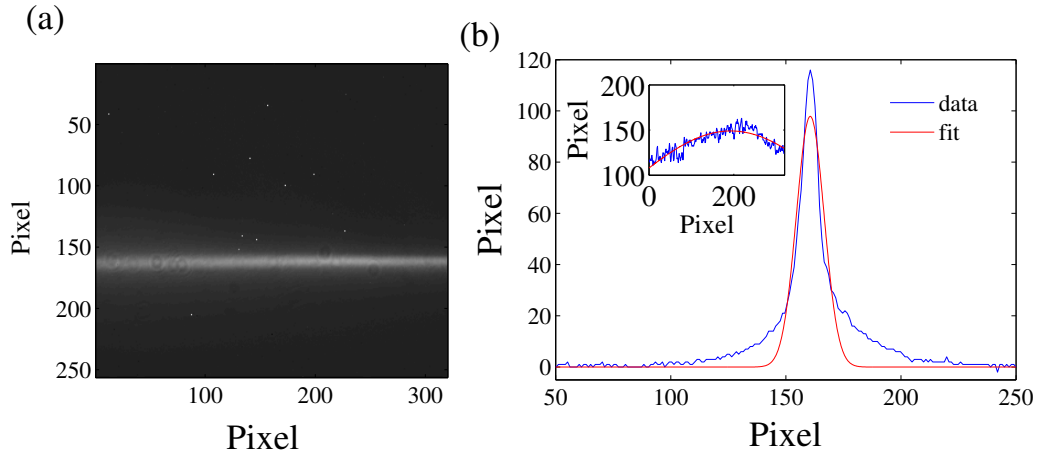
Figure 5.24: Image of the emission of the diode at (a) d = 940 cm, (b) beam profile for the slow and fast axis.

Fig. 5.25(a) shows how the signal of the single-mode fiber change as function of current. It is possible to notice that scanning the current up and down the signal doesn't stay always the same like the signal in the other detector, see Fig. 5.25(b). The reason of the variation in amplitude reported in Fig. 5.25(a) is probably due to thermal change of beam position. Fig. 5.25(c) shows instead the coupling rate achievable by the system calculated as the ratio between the signal in the coupled fiber and into the other one. The coupling is quite low.
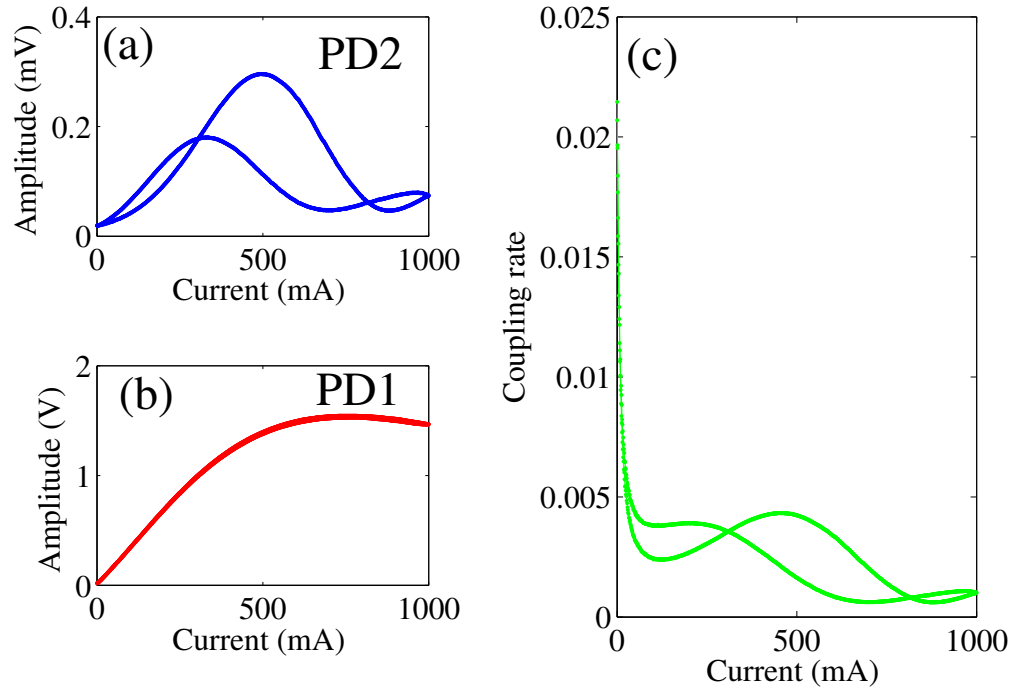
Figure 5.25: (a) Signal detected in the single-mode fiber as function of current, (b) Signal in the other detector as function of current, (c) Coupling rate into the single-mode fiber.

5.6.3   Results

It is possible to have some figure that illustrate how the gain coefficient change as function of wavelength.

Fig. 5.26(a) shows how the gain coefficient changes as function of wavelength for different current level starting at I = 0 mA at T = 5°C. The quantum dot absorb strongly at the wavelengths in the range 1260-1300 nm. Increasing the current there is an effect on gain more relevant at lower wavelength than at higher one.

Fig. 5.26(b) is the same but taken at the temperature of T = 21°C. Increasing the temperature it is possible to see that the range where quantum dots absorb changes due to the shift with temperature of the spontaneous emission spectra.

Figure 5.26: (a) Gain coefficient as function of wavelength for increasing current at T = 5 °C (b) Gain coefficient as function of wavelength for increasing current at T = 21 °C.

It is a redshift towards higher wavelengths.

It is possible to see that there are regular ripples in the transmission curve almost constant over all the wavelength range. The average distance is 5 nm corresponding to a length of 2 cm, it can be a parasitic etalon.

There is no systematic power shift of the quantum dots probably due to the very low coupled power and power available. This motivates us to search for a more powerful laser source at 1.3 μm.

5.7 Saturation of absorption and gain with Cr^{4+}-Forsterite laser

This section describes an experiment on light QD interaction with a home made Cr^{4+}-Forsterite laser that can deliver up to 100 mW at $\lambda = 1245$ to $\lambda = 1280$, much more compared to 14 mW of the previous one. We use also single spatial mode waveguide.

5.7.1 Experimental setup

The experimental setup is illustrated in Fig. 5.27. The laser is a home made (Dr. C. G. Leburn) Cr^{4+}:forsterite laser [202; 203]. After the laser a half wave plate (HWP) and an optical isolator (OI) are present to avoid back reflection to the laser and for adjust the power. The beam passing the OI is fiber coupled through a microscope objective (40X) to a single mode fiber.
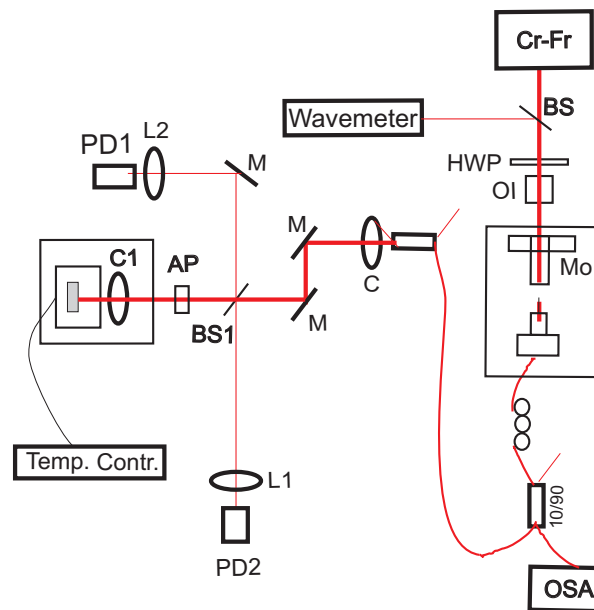
Figure 5.27: Experimental setup: Chromium forsterite (Cr^{4+}-Fr), beam splitter (BS, BS1), Half-Wave plate (HWP), Optical Isolator (OI), microscope objective (Mo), Optical Spectrum Analyzer (OSA), mirror (M), anamorphic prism pair (AP), aspherical collimator (C1) (f = 3 mm), aspherical collimator (C) (f = 3 mm) , L1 (f = 50 mm), L2 (f = 35 mm), Photodiode (PD1, PD2).

The single mode fiber is connected to a polarization control fiber which enables to select the polarization of the beam, kept in this case horizontal. The fiber is connected to a fiber coupler that split the incoming beam in 10% and 90%. The weak part of the beam is sent to an optical spectrum analyzer (OSA) to monitor the beam. The main part (90 %) is collimated by an aspherical lens (C, f = 11 mm) and sent to an anamorphic prism pair (AP). The AP is used

to transform the collimated circular beams to elliptical beam, so matching the waveguide mode.

Then the beam is coupled directly into the sample with an aspherical lens (C1) of focal length f = 3.1 mm, mounted on an high-precision xyz-translation stage. The light reflected by the sample and the light coming out from it is collected with beam splitter (BS1) and focused to the output photodiode PD1.

The laser diode used is based on quantum dot. It has a threshold current of I = 23 mA at T = 15.2 °C and a cavity length of L = 1.5 mm. The layer structure of the diode is equal to the one used in chapter 2, section. 2.4.1.

5.7.2 Diode characterization

Fig. 5.28(a) shows the spontaneous emission spectra taken with a monochromator (Gilden Photonics-resolution 0.04 nm) of the diode for different current levels. The PL is quite broad starting at $\lambda = 1200$ nm and finishing at $\lambda = 1290$ nm. No excited state and wetting layer are visible. Around the gain peak, $\lambda = 1255$ nm, and mostly above several longitudinal mode are present.
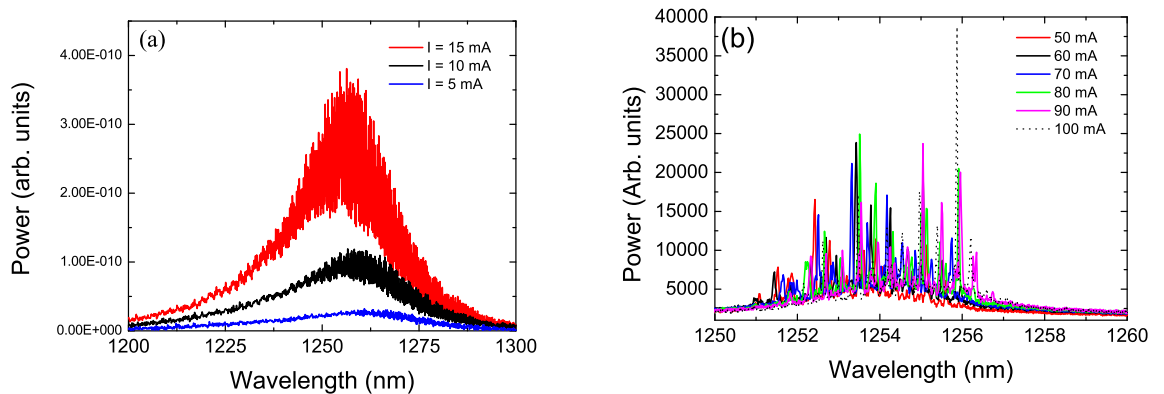
Figure 5.28: (a) Spontaneous emission from the QDL diode for different current level below threshold, (b) lasing spectra of the diode at different current level, T = 15.4 °C

Fig. 5.28(b) shows the lasing spectra for different currents level starting at I = 50 mA up to I = 100 mA. Several peak appear centered around the gain peak $\lambda = 1254$ nm.
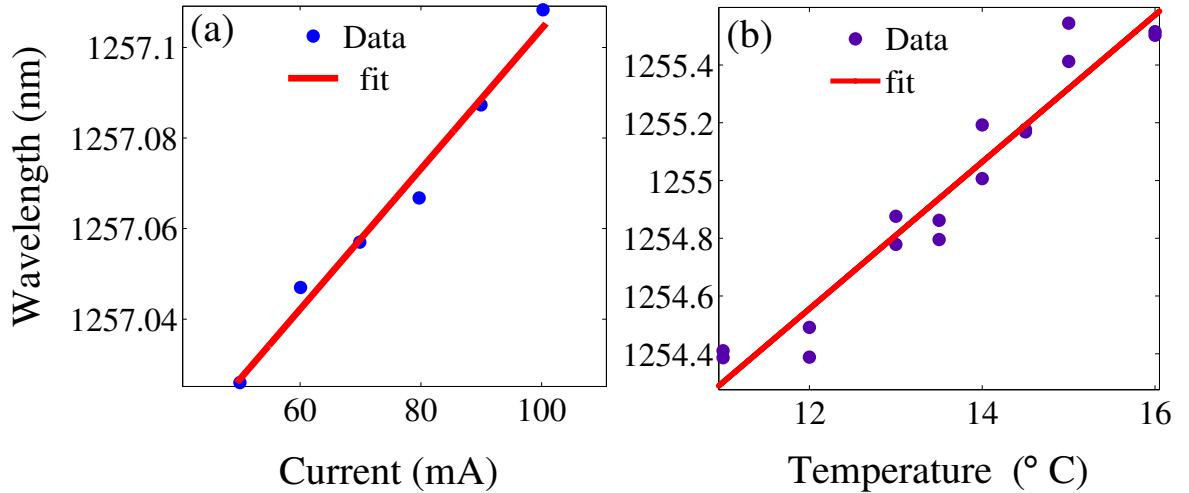
Figure 5.29: (a) Wavelength shift as function of current, T = 15.4 °C (b) Wavelength shift as function of temperature

Fig. 5.31(a) shows the wavelength shift as function of current. From the fit is possible to infer a shift of 0.0016 nm/mA.

Fig. 5.31(b) shows the wavelength shift as function of temperature. The measurement is a medium of the overall spectrum. From the fit is possible to infer a shift with temperature of 0.48 nm°C, like the one reported in the specification [204].

5.7.3   Cr^{4+}: forsterite laser

The Chromium forsterite (Cr^{4+}-Fr) laser is illustrated in Fig. 5.30 [202; 203].

The pump source used is an infrared Nd:YVO$_4$ IR laser (Spectra Physics). This source is capable of producing up to 10W of linearly polarized, near-diffraction limited light at 1064 nm. The beam is passing through a telescope system and a focusing lens before going through one of the folding mirrors (RoC f = -100 mm) and onto the crystal face. With this simple telescope system in conjunction with a focusing lens it is possible to vary the pump spot size and focus the pump beam to an appropriate size in order to maximize the mode matching of the pump and
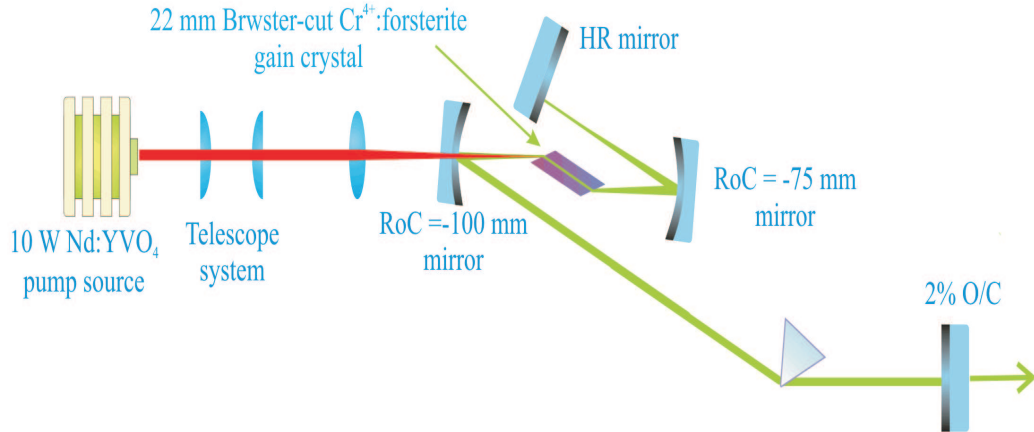
Figure 5.30: Schematic of the pump laser and pump geometry used on the Cr^{4+}:forsterite laser system. Courtesy of C. Leburn.

laser mode beams.

The Brewster-cut Cr^{4+}:forsterite laser crystal has a peak small-signal pump absorption coefficient of 1.3 cm^{-1} and a length of L = 11.6 mm. The crystal is wrapped in indium foil and tightly clamped in a water-cooled copper mount. This mount is maintained at a temperature of 14 °C to aid the removal of heat from the crystal when pumped at high powers.

The pump lensing arrangement produces a beam spot size on the laser crystal that is similar in size to the laser mode beam in the crystal. This facilitated good mode-matching of the two beams. The minimum threshold of 1.4 W is achieved with the 0.2 % output coupling. Fig. 5.31(a) shows a spectra from the Cr^{4+}:forsterite laser over time. The spectra has a full width half maximum of 0.3 nm to 0.2 nm, covering several longitudinal mode of the QD diode. Hence cavity effects are expected to be low.

Fig. 5.31(b) shows the output power achievable by the system from λ = 1235 nm to λ = 1345nm. The output power is 200 mW at λ = 1235 nm, increases up to 550 mW at λ = 1260 nm decreases again linearly to 150 mW at λ = 1345 nm.
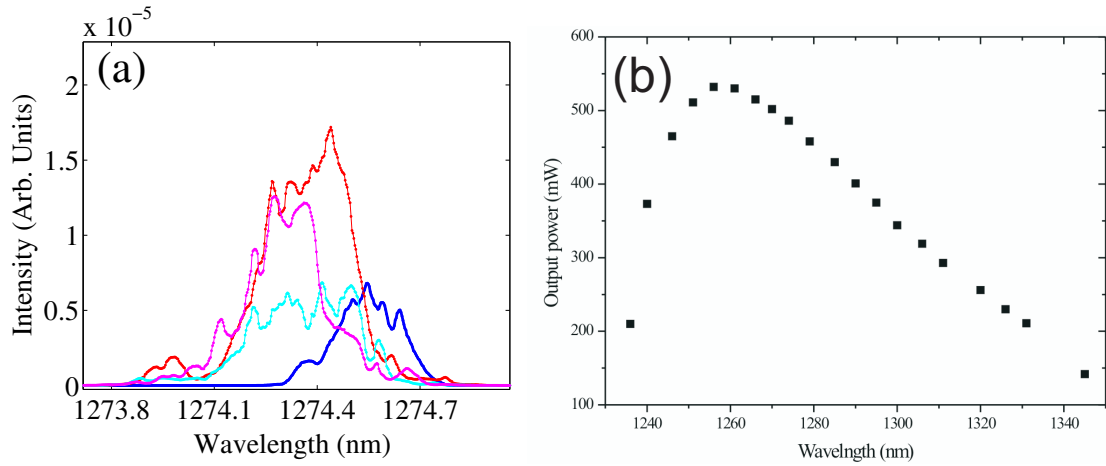
Figure 5.31: (a) Spectra over time from the Cr^{4+}:forsterite laser, (b) output power as function of wavelength.

5.7.4 Results

The procedure for the coupling is the same as discussed in section 5.6.2, where the light coming out from the QD diode is fiber coupled first, and then the beam from the Cr^{4+}-Fr, fiber coupled as well goes. The light from the Cr^{4+}-Fr is maintained horizontal polarized , TE-polarized. The coupling efficiency of the QD diode in the single mode fiber is 37%.

Fig. 5.32(a) shows how the gain coefficient changes as function of input power for λ = 1245 nm in gain, I = 24 mA, and absorption, I = 0 mA. The reflection coefficient from the quantum dots shows a pronounced power dependence starting at power less than 10 mW for the absorption case and for the gain case the power dependence starting at lower power. The gain saturates sooner than the absorption.

Fig. 5.32(b) shows how the gain coefficient change as function of power for λ = 1255 nm for gain and absorption.

Fig. 5.33(a) shows how the gain coefficient change as function of power for λ = 1265 nm in presence of gain and absorption. Fig. 5.33(b) shows instead the value for λ = 1280 nm in gain and absorption.

It shows that in absorption the gain is constant for all the available power, so it shows that the QD doesn't show power dependence as in the previous figure.
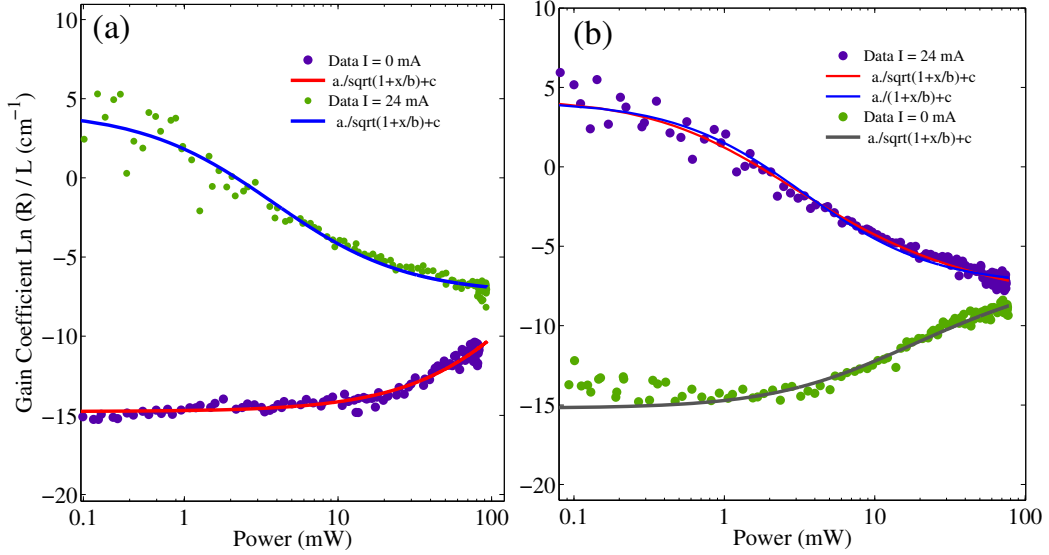
Figure 5.32: (a) Gain coefficient as function of input power at $\lambda = 1245$ nm, data and fit. (b) Gain coefficient as function of input power at $\lambda = 1255$ nm data and fit.

In gain there is still a small offset.
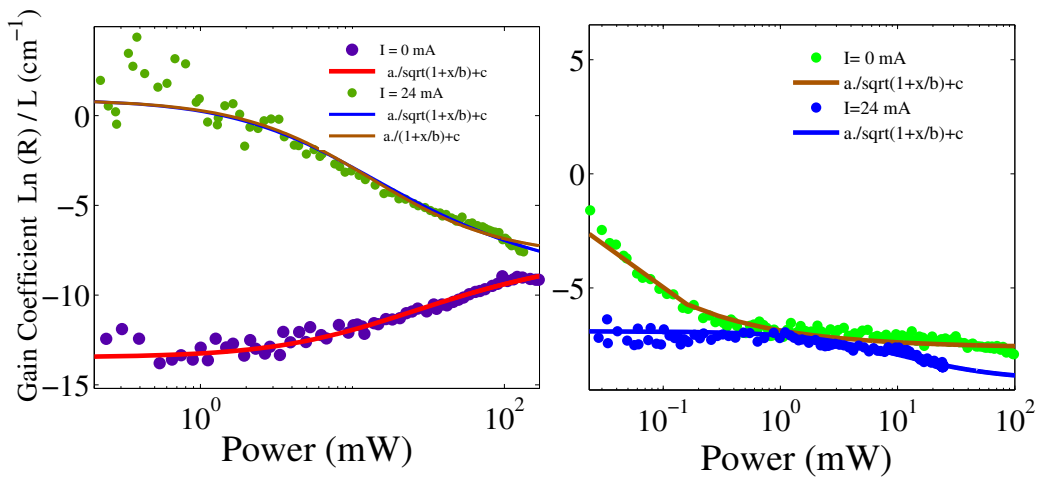
Figure 5.33: (a) Gain coefficient as function of input power at $\lambda = 1265$ nm, data and fit. (a) Gain coefficient as function of input power at $\lambda = 1280$ nm

The dependence of the gain coefficient on power with two models that describe

saturable absorption in the case of two-level systems with inhomogeneous, $\alpha_I = \alpha_I/\sqrt{(1 + P/P_{sat})}$ and homogeneous, $\alpha_I = \alpha_I/(1 + P/P_{sat})$, broadening [144]. The results shows that both model fit the data quite well but the first model proves to fit better especially at $\lambda = 1245$ nm and $\lambda = 1280$ nm.
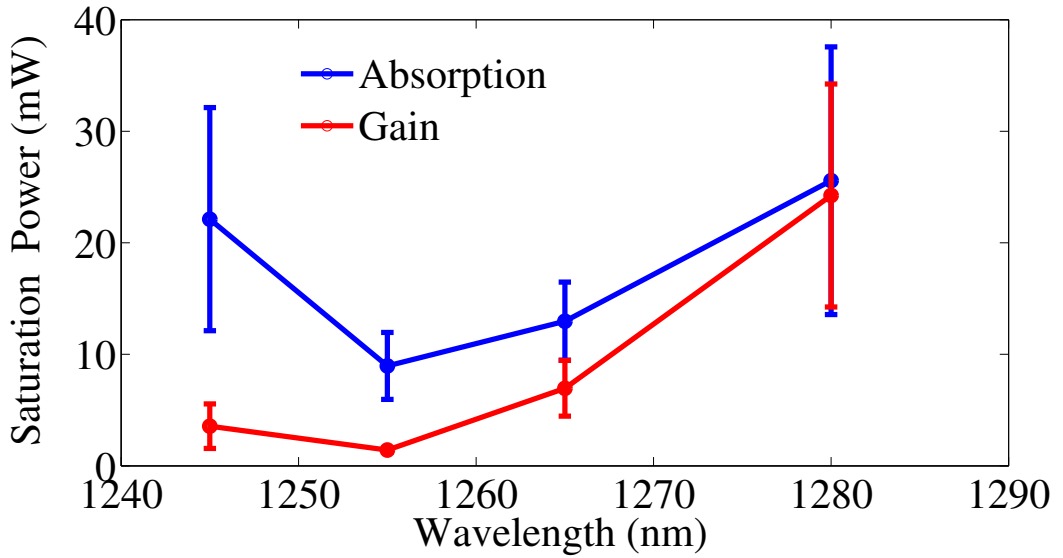
Figure 5.34: Saturation power as function of wavelength in absorption and gain cases.

Fig. 5.34 shows the results of the fit displayed in Fig. 5.32(a), Fig. 5.32(b), Fig. 5.33(a), Fig. 5.33(b).

Fig. 5.34 shows the saturation power as function of wavelength in absorption and gain. The minimum saturation power is reached at $\lambda = 1255$ nm and is $P_{sat} = 9$ mW in the absorption case and of $P_{sat} = 1.4$ mW in the gain case. For increasing wavelength the saturation of power increases up to $P_{sat} = 25$ mW in absorption and $P_{sat} = 21$ mW in the gain case. At lower wavelength also the saturation power increases up to $P_{sat} = 25$ mW for the absorption case.

Fig. 5.34 also shows that the value of power saturation relative to the gain are low compared to the absorption case due to the experimental finding that the gain is more easy to saturates than the absorption also present in section 5.2.3. This is not the case for the numerical simulation, chapter 3, where actually the value of saturation of gain and absorption are very comparable.

It is possible to give an indication of the saturation intensity to compare to results where pulsed lasers are involved. Assuming beam radius of $w_x = 3 \times 10^{-6}$ m in the slow direction and $w_y = 0.5 \times 10^{-6}$ m for the fast axis the intensity is given by:

$$I_{sat} = \frac{2P_{sat}c_{eff}}{w_x w_y} \tag{5.13}$$

where P$_{sat}$ are the saturation power reported in Fig. 5.34 and $c_{eff} = 0.37$ is the coupling efficiency. This lead to an intensity of around $I_{sat} = (0.44\text{-}7) \times 10^8$ W/m^2 depending on wavelength in agreement with results on pulsed beam [121; 205].

5.8 Nonlinear index shift in InGaAs QD

In this section, we analyze results from measurements of the frequency shift of the sample, discussed theoretically in chapter 3, and covered as well for InAlAs quantum dots in section 5.5.5.

5.8.1 Experimental setup

The experimental setup is shown in fig. 5.35. A lock in amplifier [206; 207] is set in to distinguish the pump laser from the probe beam. The pump laser is the same Cr^{4+}: fosferite used for the previous experiment.

The probe is a commercial semiconductor laser (Santec TSL-210V) that span in wavelength from $\lambda = 1260$ nm to $\lambda = 1360$ nm. The probe is chopped at frequency of 800 Hz by a chopper connected to the lock-in amplifier.

The probe beam is passing to an optical circulator (CO). The Optical circulator is a special fiber optic device that is capable of separating optical power traveling in opposite directions in one optical fiber. It is used to achieve bidirectional transmission over a single fiber. Then the fiber is connected to the other port of the fiber coupler.
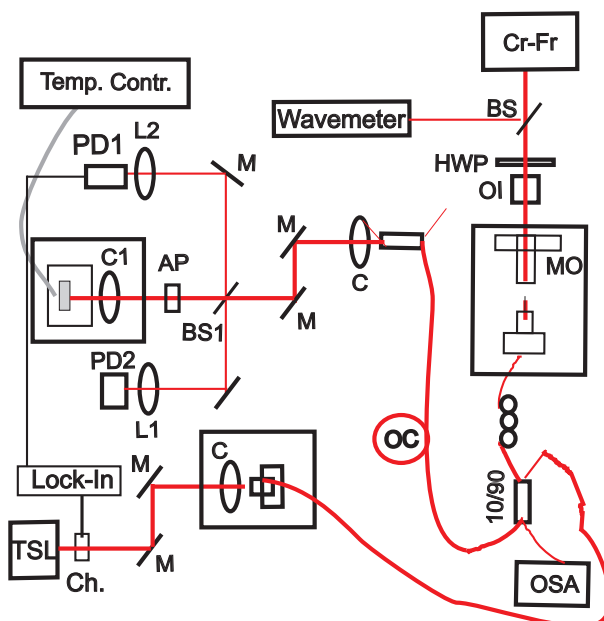
Figure 5.35: Experimental setup: Chromium forsterite (Cr^{4+}:Fr), beam splitter (BS, BS1), Half-Wave plate (HWP), Optical Isolator (OI), microscope objective (MO), Optical Spectrum Analyzer (OSA), mirror (M), Anamorphic prism pair (AP), aspherical collimator (C1) (f = 3 mm), aspherical collimator (C) (f = 11 mm) , L1 (f = 50 mm), L2 (f = 35 mm), Photodiode (PD1, PD2), Optical circulator (OC).

5.8.2 Measurement with probe

The measurements are been taken scanning the wavelength of the tunable source (TSL-210V) in steps of 0.0005 nm (resolution in wavelength of the laser) and recording the average (over 10) reading of the output photodiode. All the data are recorded through National Instrument Card (DAQ) controlled by a PC through Labview. The time between each measurement is 2s.

Fig. 5.36(a) shows the linear reflection spectrum from the QD diode of the probe laser. It has been taken at $\lambda = 1280$ nm at T = 15 °C with a power of 0.7 mW in absorption, I = 0 mA.

Fig. 5.36(a) shows the cavity modes in the reflected signal, not present in the input photodiode. These cavity modes are very pronounced and well defined compared to that one observed, in the transmission experiment, discussed in
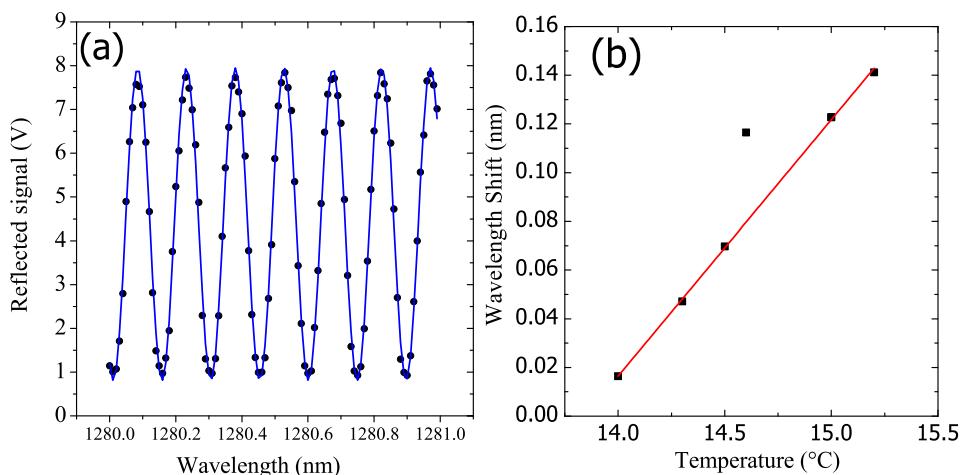
Figure 5.36: (a) Linear reflection spectrum, data points and fit (blue line) (b) Wavelength shift of cavity modes as function of temperature, probed with tunable laser (TSL-210V) in reflection, P = 0.7 mW, I = 0 mA.

section 5.5.5. They are large amplitude signal over a small background. The reflected signal is not calibrated.

The cavity modes are been fitted (blue curve, Fig. 5.36(a)) by a sinusoidal equation in the form $y = y_0 + A\sin(\pi(x - x_c)/w)$. From the coefficient of the fit is possible to infer the period and the free spectral range (FSR). The FSR is 0.148 nm assuming a group index of $n_g = 3.7$. The FSR corresponds to a length of L = 1.49 mm, matching the length of the QD diode (L = 1.5 mm). Fig. 5.36(b) shows how the cavity mode spacing shift in wavelength as function of temperature from T = 14 °C to T = 15.3 °C. From the linear fit it is possible to infer a shift of 0.105 nm/°C.

Fig. 5.37(a) shows the reflected signal as function of wavelength for different power level of the probe, starting at 0.002 mW up to 20 mW in absorption, I = 0 at T = 15 °C. The fact that the amplitude of the reflected signal is different is due to the different gain setting of the detector used, the data are not normalized.

Fig. 5.37(b) is the linear fit (red) and data points of the position of the minimum of the cavity mode as function of the input power. From the fit it is possible to infer a small average red-shift increasing the probe power of

145
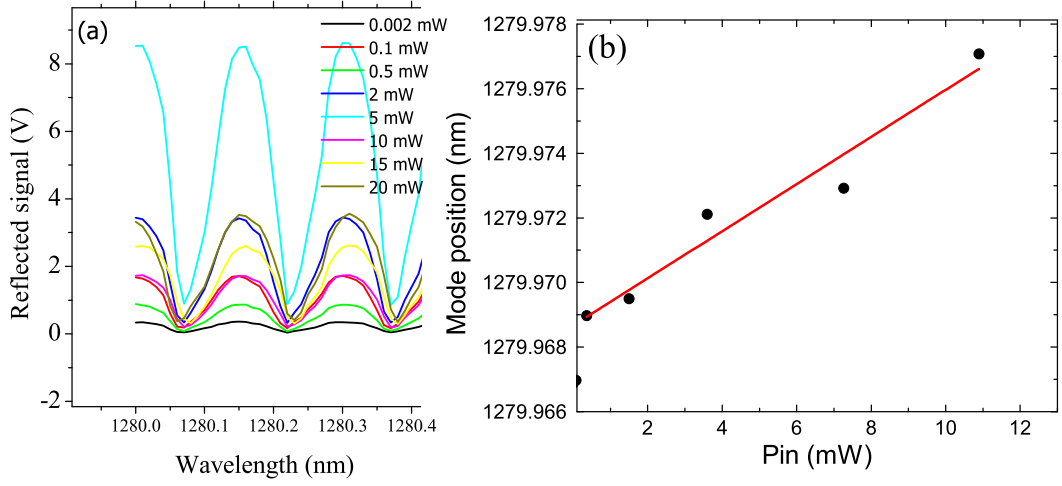
Figure 5.37: (a) Reflected signal as function of wavelength from $\lambda = 1280.06$ nm to $\lambda = 1280.4$ nm for different input power I = 0 mA. (b) Mode position as function of input power, I = 0 mA.
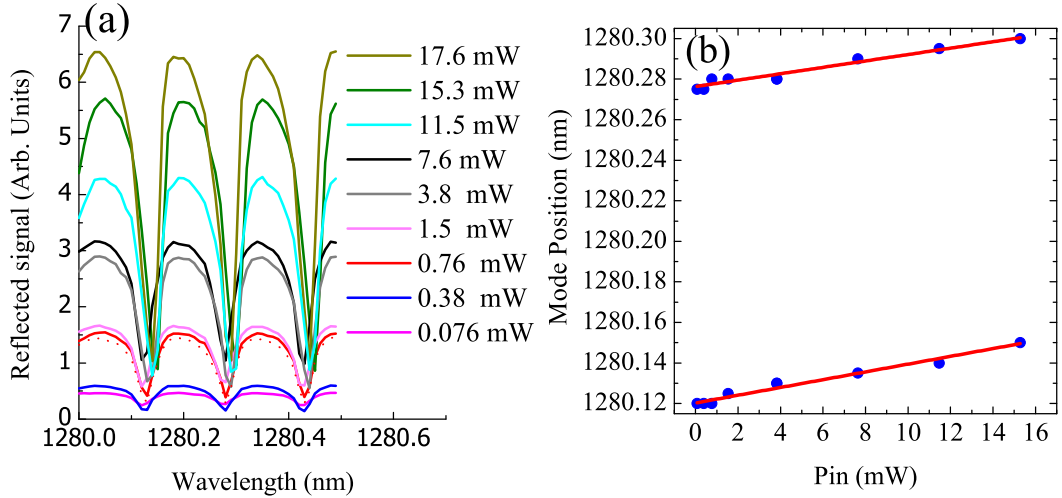
Figure 5.38: (a)Reflected signal as function of wavelength from $\lambda = 1280.06$ nm to $\lambda = 1280.5$ nm for different input power I = 24 mA. (b) Shift of cavity modes as function of wavelength from $\lambda = 1280.06$ nm to $\lambda = 1280.5$ nm for different input power I = 24 mA.

$\approx (7.3 \pm 1) \times 10^{-4}$ nm/mW.

Fig. 5.38(a) shows the shift of the cavity modes as function of wavelength for different power level starting at 0.076 mW up to 17.6 mW with gain, I = 24 mA.

Fig. 5.38(b) is the linear fit of the position of minimum of the ripple as func-

146

tion of the input power. From the fit it is possible to infer an average red-shift increasing the probe power in this case of $\approx (1.8 \pm 0.08) \times 10^{-3}$ nm/mW for fig. 5.38(b).

5.8.3 Pump-probe measurement

Measurement have been taken using the hight power pump beam as well, following the setup of Fig. 5.35. A weak probe beam is also present in the measurement.
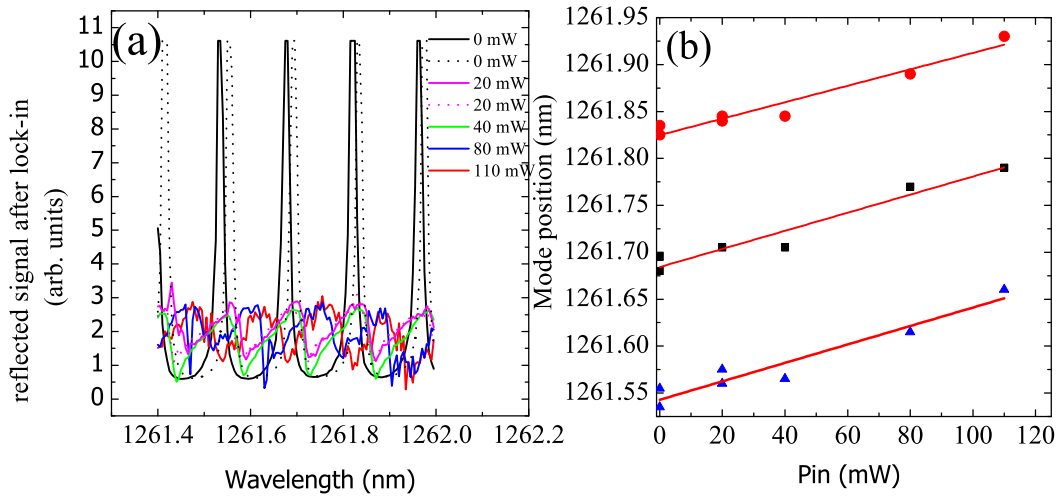
Figure 5.39: (a) Linear reflection spectrum for $\lambda = 1261$ nm at T = 15 °C, I = 24 mA (b) Shift of cavity modes as function of input power.

Fig. 5.39(a) shows the reflected signal as function of wavelength from $\lambda = 1261.4$ nm to $\lambda = 1262$ nm for different pump power starting at 0 mW of the pump and up to 110 mW in gain I = 24 mA. The dashed line correspond to the jitter of the cavity mode. These give an error on the measurement of $\sigma \approx 6 \times 10^{-3}$ nm.

Fig. 5.39(b) is the linear fit of the modes taken from Fig. 5.39(a). It is the data position of the minimum of the peak. From the linear fit it is possible to infer an average red-shift of $\approx (9.5 \pm 0.006) \times 10^{-4}$ nm/mW.

Fig. 5.40(a) shows the shift of these cavity modes as function of wavelength from $\lambda = 1271.6$ nm to $\lambda = 1272.2$ nm for different pump power starting at 0 mW and up to 130 mW with I = 24 mA.
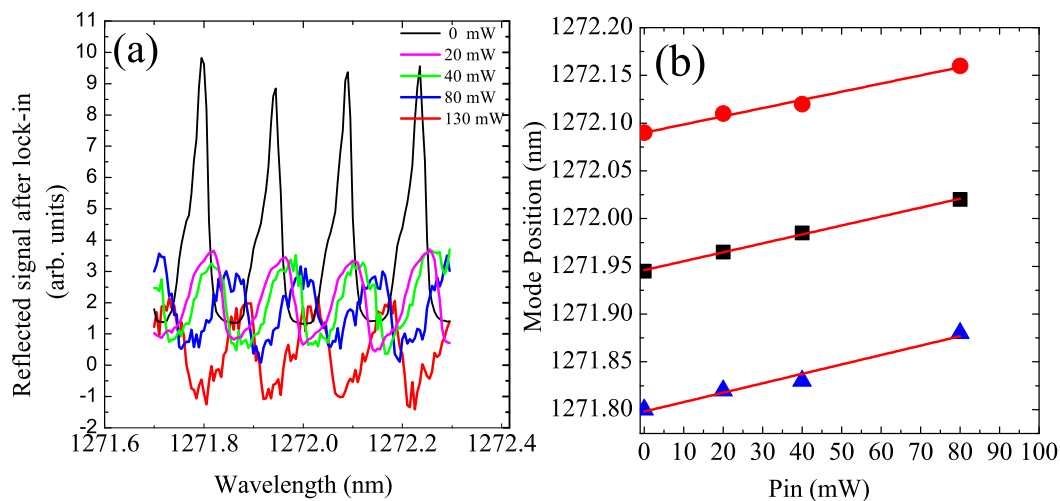
Figure 5.40: (a) Linear reflection spectrum for $\lambda = 1272$ nm (b) Shift of cavity modes as function of input power.

The shape of the cavity mode is different from Fig. 5.39(a) due to increasing finesse with wavelength, different threshold condition at different wavelength. Fig. 5.40(b) is the linear fit taken from Fig. 5.40(a). It is the data position of the minimum of the peak.

From the linear fit it is possible to infer an average red-shift in this case of $\approx$ $(9.4 \times 10^{-4} \pm 6 \times 10^{-7})$ nm/mW. The shift at $\lambda = 1261.6$ nm and $\lambda = 1271.6$ nm are the same.

Fig. 5.41 is a summary of the shift of the fringes shift as function of wavelength from $\lambda = 1262.12$ nm to $\lambda = 1282.12$ nm in the case where pump and probe is present and in the case where only probe is present without lock in in absorption and gain.

From $\lambda = 1262.12$ nm to $\lambda = 1282.12$ nm the fringe shift is constant at the value of 0.001 nm/mW. Instead when only the probe laser is on and no lock-in is present in the setup the fringe shift is of 0.002/0.0025 nm/mW in gain. In absorption, only with probe in there is a small fringe shift of 0.0007 nm/mW.

Is not possible to see a shift depending on detuning of the laser, the shift is constant for all the available wavelength.
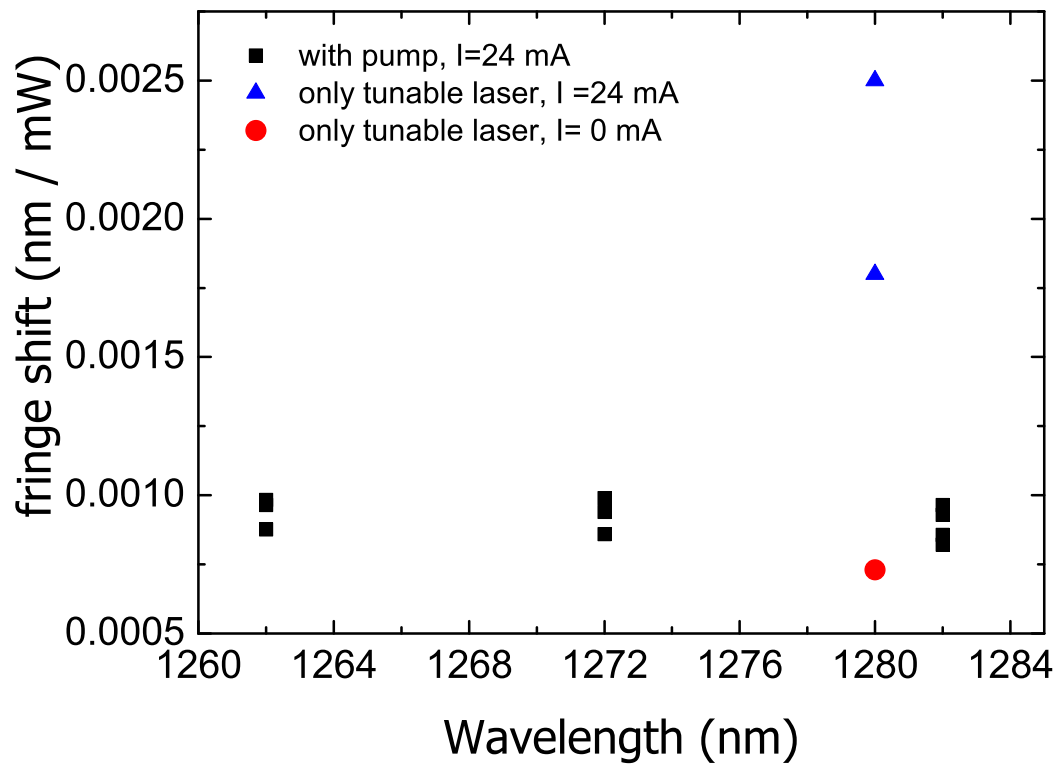
Figure 5.41: Shift of the fringes as function of wavelength from $\lambda = 1262$ nm to $\lambda = 1282$ nm

5.8.4   Discussion and comparison to other experiment

The origin of the shift observed is not so clear. The shift appear only for TE-polarized light like in [205]. The cavity mode shifts doesn't depend on detuning of the pump–probe beam, is the same for different wavelength.

Probably is thermal, possibly some background heating outside of the active zone. The shift is also quite substantial, larger than expected, nearly 2π. Normally a phase shift of 0.5 π rad in 1 mm-long waveguide is obtained at a 30 pJ/μ^2 input pump pulse energy density, and 11 meV detuning energy, and a 20 ps time delay [205].

The nonlinear phase shift (NLO) in [205] is mainly attributed to the absorption saturation induced by a resonant excitation in a ground-state transition of the QDs. A pump pulse whose wavelength is set to the QD-absorption peak causes an absorption change Δa (spectral hole burning) and a corresponding refractive index change Δn. A probe pulse with some detuning energy sees the changes, Δa and Δn. The refractive index change causes the NLO phase shift of interest here. As shown, the phase shift depends on the input pump energy density P_{in} but not on the detuning energy. The shift is observed only for TE-polarized light.

This measurement and the calculation under the two-level approximation also revealed that the phase shift is mainly attributed to the absorption saturation in the QDs for TE-polarized light.

.

Chapter 6

Conclusions

In this thesis, we have shown first results on how to improve the coherence of an as-grown broad-area laser diode based on quantum dots. The achieved bandwidth of 5-10 GHz at power levels of 10-140 mW [58] is sufficient for many applications such as investigating the nonlinear optics of QD though at higher current the spatial coherence is not optimal. The frequency resolution of the setup can be improved only marginally by using a grating with 1350-1400 lines/mm but a straightforward and significant improvement of performance is expected by anti-reflection coating of the facet on which the feedback is done.

So we concentrated on a small-area QD diode laser with anti-reflection coating in one facet and hight-reflective coating in the other. In Littrow and Littman configuration a bandwidth of 38 GHz has been achieved for all the wavelength accessible by the system (λ = 1195-1260 nm) and remarkably for all the current available (up to I = 1 A) differently from the broad area diode where at higher current the diode present multimode behavior. We use the small-area QD diode because is possible to have more power in single mode shape.

The established tunable source has been used to characterize optical and electrical properties of InAs/GaAs quantum dot and LT-GaAs super-lattice materials for Terahertz applications. The material was grown using a surfactant growth technique [104]. Therefore, one of the advantages of InAs/GaAs superlattice and QDs structures is the ability to use a 1.3 μm excitation wavelength and maintain a high resistivity of the material at the same time. The dependences on exciting wavelength, power and bias voltage were studied and the data obtained suggests

that they can be used as photoconductive materials that can be excited at the telecoms wavelengths of 1.3 μm for Terahertz or other optoelectronic applications. Fairly hight photocurrent has been found for the quantum dot, but also remarkably for the superlattice which doesn't display a PL. This is probably more attractive for THz applications due to the lower lifetime than the QD samples. To our knowledge these are the first results on photocurrent in low-dimensional InGaAs structure for THz [59].

Self-sustained pulsations of the output have been observed in an InAs quantum dot laser diode in the MHz range for the first time [61; 62]. The pulsations have in tendency a square-wave-like appearance and are present for a wide range of current and wavelength. The free-running laser and the laser with feedback show qualitatively the same behavior except in frequency-resolved optical spectra. Here the different shift of the envelope might be related to a change of phase-amplitude coupling across the gain maximum in qualitative agreement with the expectation for a general two level system. The time scale and the bifurcation scenario suggest that these are opto-thermal pulsations like the ones reported in quantum well amplifiers [63] but there is no obvious mechanism of a competition between resonance conditions. Bistability in the light-current characteristics is also observed for wavelengths smaller than the gain peak ($\lambda = 1225$ nm), but it is not present for wavelength above the gain peak and for the free running lasers [65].

The experiments performed support a new mechanism for opto-thermal pulsations based on waveguiding [60]. Due to the shallow etching, the mode is not strongly confined but the confinement and hence the modal gain - is enhanced by the refractive index increase in the ridge due to Joule heating. After switch-on, radiative cooling leads to a reduction in confinement and the laser switched down again. Then the process is started again by heating. At some point, the average heat load is high enough to sustain cw lasing. Supporting this, we established that devices with a slightly deeper etching and hence better confinement do not show this instability.

We calculate the nonlinear optical response of a sample of self-assembled QD to a cw driving field via numerical simulations [64].

It is found that a saturation model based on inhomogeneous broadening fits the numerical results but that the saturation power depends on detuning in contrast to a strongly inhomogeneously broadened system. This is interpreted to be due to that fact that QD are in the Voigt-parameter regime between homogeneous and inhomogeneous broadening.

Measuring self-lensing might be a convenient way to check out the absolute and relative strength of phase-amplitude coupling (the α-factor) for resonant and off-resonant operation. From the real part of the susceptibility, the strength of self-lensing is deduced. For conservative assumptions on QD density and carrier lifetimes, the minimum focal length is found to be 1.7 mm for an input beam with a radius of about 15 μm. This effect is probably too small to be experimentally detectable but increasing the focal power by a factor of two already changes these conclusions.

Around the gain peak, lensing is found to be negligible which makes this range promising for the operation of high power lasers with a low tendency to filamentation.

Following the numerical simulations we report studies on the interaction strength between laser and self assembled quantum dots, as a function of power in the form of the absorption and gain coefficient. Our analysis is concentrated on continuous wave (cw) beam interacting with quantum dot structures. Several setups have been arranged (Chapter 5) and relevant results are presented regarding saturation of absorption and gain [65]. The results presented for the gain measurement are in agreement with previous measurement [147; 149; 161; 194; 196] and theoretical results on gain saturation [64; 197]. Results on saturation of absorption of AlGaAs and InGaAs on cw beam are presented. To my knowledge this is the first evidence of saturation of absorption in room temperature samples and opens up new opportunity for nonlinear optics of QD samples.

No clear evidence for a nonlinear phase shift is found except in time-resolved spectra of a self pulsing laser. The nonlinear optical effects are reduced due to the inhomogeneous broadening of relatively low density of QD. Improvement in growth technique [161; 162] and submonolayer QD might be helpful to achieve a high nonlinearity. On the other hand the low α-factor is beneficial for applications.

List of publications related to this thesis

1. A. Tierno and T. Ackemann *Tunable, narrow-band light source in the 1.25 µm region based on broad-area quantum dot lasers with feedback.* Appl. Phys. B, **89**, 585-588 (2007).

2. A. Tierno, T. Ackemann, T. Maggipinto and M. Brambilla *Saturation and self-lensing in self-assembled quantum dots with constant-wave driving* Phys. Rev. B, **80**, 035314 (2009).

3. A. Tierno and T. Ackemann. *Opto-thermal pulsations via changes in waveguiding in a quantum dot lasers diode.* Appl. Phys. Lett., submitted, 2010.

4. A. Tierno, N. Radwell, and T. Ackemann. *Bistability, opto-thermal pulsations and time-resolved spectra of a quantum dot lasers diode.* IEEE Journal of Quantum Electronics, in preparation, 2010.

5. A. Tierno and T. Ackemann. *Bistability and opto-thermal-pulsations in a quantum-dot edge-emitting laser diode.* J. Phys. Conf., accepted for pubblication, 2010.

6. A. Tierno, N. Radwell, and T. Ackemann. *Time-resolved spectra of a self-pulsing quantum dot laser.* Proc. SPIE, **7720**, 78, (2010).

7. M. Alduraibi, M. Missous, P. Luke Sam, A. Tierno, S. Keatings and T. Ackemann. *Optical and electrical properties of stacked binary InAs-GaAs quantum dot structures prepared under Surfactant-mediated growth conditions,* J. Phys. Conf., accepted for pubblication, 2010.

References

[1] J. D. Kingsley T. J. Soltys R. N. Hall, G. E. Fenner and R. O. Carlson. *Coherent Light Emission From GaAs Junctions*. **9**(9), 1962. 1

[2] P. W. Foy Y. Hayashi, M. B. Panish and S. Sumski. *Junction lasers which operate continuously at room temperature*. Appl. Phys. Lett., **17**(3), 1970. 2

[3] R. Dingle, W. Wiegmann, and C. H. Henry. *Quantum states of confined carriers in very thin $Al_{(x)}Ga_{(1-x)}As$-$GaAs$-$Al_{(x)}Ga_{(1-x)}As$ heterostructures*. Phys. Rev. Lett, **33**(14), 1974. 2

[4] J. Stangl, V. Holý, and G. Bauer. *Structural properties of self-organized semiconductor nanostructures*. Rev. Mod. Phys., **76**(3):725–783, Sep 2004. 4

[5] P. Bhattacharya, D. Bimberg, and Y. Arakawa. *Special Issue on Optoelectronic Devices Based on Quantum Dots*. Proc. IEEE, **95**:1718–1722, 2007. 6

[6] R. Waburton. *Self-assembled semiconductor quantum dots*. Contemporary Physics, **43**(5):351–364, 2010. 6

[7] Y. Arakawa and A. Yariv. *Theory of gain, modulation response, and spectral linewidth in AlGaAs quantum well lasers*. IEEE J. Quantum Electron., **21**:1666–1674, 1985. 6

[8] Y. Arakawa and A. Sakaki. *Multidimensional quantum well laser and temperature dependence of its threshold current.* Appl. Phys. Lett., **40**:939, 1982. 6, 11, 17, 21

[9] Gokhan Ozgur, Abdullah Demir, and Dennis G. Deppe. *Threshold Temperature Dependence of a Quantum-Dot Laser Diode With and Without p-Doping.* IEEE J. of Quantum Electron., **45**(10):1265–1271, 2009. 6, 10

[10] D. J. Eaglesham and M. Cerullo. *Dislocation-free Stranski-Krastanow growth of Ge on Si(100).* Phys. Rev. Lett., **64**(16):1943–1946, Apr 1990. 7

[11] I. N. Stranski and L. Kr'stanov. *Theory of orientation separation of ionic crystals.* Sitzungsber. Akad. Wiss. Wien, Math.-Naturwiss. Kl., Abt. 2B, 146:797–810, 1938. 7

[12] D. M. Bruls, J. W. A. M. Vugs, P. M. Koenraad, H. W. M. Salemink, J. H. Wolter, M. Hopkinson, M. S. Skolnick, Fei Long, and S. P. A. Gill. *Determination of the shape and indium distribution of low-growth-rate InAs quantum dots by cross-sectional scanning tunneling microscopy.* Appl. Phys. Lett., **81**(9):1708–1710, 2002. 7

[13] J. A. Barker and E. P. O'Reilly. *Theoretical analysis of electron-hole alignment in InAs-GaAs quantum dots.* Phys. Rev. B, **61**(20):13840–13851, May 2000. 8

[14] P. W. Fry, I. E. Itskevich, D. J. Mowbray, M. S. Skolnick, J. J. Finley, J. A. Barker, E. P. O'Reilly, L. R. Wilson, I. A. Larkin, P. A. Maksym, M. Hopkinson, M. Al-Khafaji, J. P. R. David, A. G. Cullis, G. Hill, and J. C. Clark. *Inverted Electron-Hole Alignment in InAs-GaAs Self-Assembled Quantum Dots.* Phys. Rev. Lett., **84**(4):733–736, Jan 2000. 8

[15] B. Grandidier, Y. M. Niquet, B. Legrand, J. P. Nys, C. Priester, D. Stiévenard, J. M. Gérard, and V. Thierry-Mieg. *Imaging the Wave-Function Amplitudes in Cleaved Semiconductor Quantum Boxes.* Phys. Rev. Lett., **85**(5):1068–1071, Jul 2000. 8

[16] P. B. Joyce, T. J. Krzyzewski, G. R. Bell, B. A. Joyce, and T. S. Jones. *Composition of InAs quantum dots on GaAs(001): Direct evidence for (In,Ga)As alloying.* Phys. Rev. B, **58**(24):R15981–R15984, Dec 1998. 8

[17] R. Heitz, H. Born, F. Guffarth, O. Stier, A. Schliwa, A. Hoffmann, and D. Bimberg. *Existence of a phonon bottleneck for excitons in quantum dots.* Phys. Rev. B, **64**(24):241305, Nov 2001. 8

[18] Per Lunnemann and Jesper Mørk. *Reducing the impact of inhomogeneous broadening on quantum dot based electromagnetically induced transparency.* Appl. Phys. Lett., **94**(7):071108, 2009. 8

[19] P. Borri, W. Langbein, J. M. Hvam, F. Heinrichsdorff, M.-H. Mao, and D. Bimberg. *Ultrafast gain dynamics in InAs-InGaAs quantum-dot ampliers,.* Photonics Technology Letters IEEE, **12**:594–596, 2000. 9

[20] W. Ouerghui, A. Melliti, M.A. Maaref, and J. Bloch. *Dependence on temperature of homogeneous broadening of InGaAs/InAs/GaAs quantum dot fundamental transitions.* Physica E: Low-dimensional Systems and Nanostructures, **28**(4):519–524, 2005. 9

[21] P. Borri, W. Langbein, J. M. Hvam, F. Heinrichsdorff, M.-H. Mao, and D. Bimberg. *Spectral Hole-Burning and Carrier-Heating Dynamics in In-GaAs Quantum-Dot Amplifiers.* IEEE J. Sel. Top. Quantum Electron., **6**:544–551, 2000. 9

[22] A. V. Uskov, E.P. O'Reilly, M. Laemmlin, N. N. Ledentsov, and D. Bimberg. *On gain saturation in quantum dot semiconductor optical amplifiers.* Opt. Commun., **248**:211219, 2005. 9, 85

[23] C. H. Henry. *Theory of the linewidth of semiconductor lasers.* IEEE J. Quantum Electron., **18**:259–264, 1982. 9, 65, 74

[24] Sergey Melnik, Guillaume Huyet, and Alexander Uskov. *The linewidth enhancement factor α of quantum dot semiconductor lasers.* Opt. Express, **14**(7):2950–2955, 2006. 10

[25] S. Fathpour, S. Bhattacharya, P. Pradhan, and S. Ghosh. *Linewidth enhancement factor and near-field pattern in tunnel injection In Ga As self-assembled quantum dot lasers.* Electron. Lett, **39**:14431445, 2003. 10

[26] S. Schneider, P. Borri, W. Langbein, U. Woggon, R. L. Sellin, D. Ouyang, and D. Bimberg. *Linewidth Enhancement Factor in InGaAs Quantum-Dot Amplifiers.* IEEE J. Quantum Electron., **40**:1423–1429, 2004. 10, 66, 75

[27] M. Juhl Zhangcheng Xua, D. Birkedal and J. M. Hvam. *Submonolayer InGaAs/GaAs quantum-dot lasers with high modal gain and zero-linewidth enhancement factor.* Appl. Phys. Lett. , **85**:3259–3261, 2004. 10, 20, 28, 66, 75

[28] M. Brambilla, T. Maggipinto, I. M. Perrini, S. Barbay, and R. Kuszelewicz. *Modeling pattern formation and cavity solitons in quantum dot optical microresonators in absorbing and amplifying regimes.* Chaos, **17**:037119, 2007. 10, 19, 81, 82, 83, 87, 102

[29] N.N.; Grundmann M.; Bimberg D.; Ustinov V.M.; Ruvimov S.S.; Maximov M.V.; Kop'ev P.S.; Alferov Zh.I.; Richter U.; Werner P.; Gosele U.; Heydenreich J. Kirstaedter, N.; Ledentsov. *Low threshold, large T_o injection laser emission from (InGa)As quantum dots.* Electron. Lett., **30**:1416–1417, 1994. 10

[30] F. Heinrichsdorff, M.-H. Mao, N. Kirstaedter, A. Krost, D. Bimberg, A. O. Kosogov, and P. Werner. *Room-temperature continuous-wave lasing from stacked InAs/GaAs quantum dots grown by metalorganic chemical vapor deposition.* Applied Physics Letters, **71**(1):22–24, 1997. 10

[31] K. Kamath, P. Bhattacharya, T. Sosnowski, T. Norris, and J. Phillips. *Room-temperature operation of In[sub 0.4]Ga[sub 0.6]As/GaAs self-organised quantum dot lasers.* Electronics Letters, **32**(15):1374–1375, 1996. 10

[32] R. Mirin, A. Gossard, and J. Bowers. *Room temperature lasing from InGaAs quantum dots.* Electronics Letters, **32**(18):1732, 29 1996. 10

[33] M. Datta and Wasiczko Dilli, Z. *Quantum Dot Lasers*, volume **6**. Cambridge University Press, Cambridge, 1997. 11

[34] Levon V. Asryan and Robert A. Suris. *Upper limit for the modulation bandwidth of a quantum dot laser.* Appl. Phys. Lett., **96**(22):221112, 2010. 11

[35] M. Sugawara, N. Hatori, and et al Ishida. *Recent progress in self-assembled quantum-dot optical devices for optical telecommunication: temperature-insensitive 10Gbs-1 directly modulated lasers and 40Gbs-1 signal-regenerative amplifiers.* J. Phys. D: Appl. Phys., **38**:2126–2134, 2005. 11, 21

[36] A.E. Zhukov S.S. Mikhrin A.P. Vasilev Yu.M. Shernyakov M.V. Maximov D.A. Livshits V.M. Ustinov Zh.I. Alferov N. N.Ledentsov A.R. Kovsh, N.A. Maleev and D. Bimberg. *InAs/InGaAs/GaAs quantum dot lasers of 1.3 μm range with high (88%) differential efficiency.* Electron. Lett., **38**:1104–1105, 2002. 11, 20, 28, 85

[37] Weng Chow. Studies on the relative advantages of quantum-dot and quantum-well gain media in lasers and amplifiers. In *Conference on Lasers and Electro-Optics/International Quantum Electronics Conference*, page CMV1. Optical Society of America, 2009. 11

[38] U. Bockelmann and G. Bastard. *Phonon scattering and energy relaxation in two-, one-, and zero-dimensional electron gases.* Phys. Rev. B, **42**:8947–8951, 1990. 12

[39] Xin Qi Li, Hajime Nakayama, and Yasuhiko Arakawa. *Phonon bottleneck in quantum dots: Role of lifetime of the confined optical phonons.* Phys. Rev. B, **59**:5069–5073, 1999. 12

[40] Mitsuru Sugawara, Kohki Mukai, and Yoshiaki Nakata. *Effect of phonon bottleneck on quantum-dot laser performance.* App. Phys. Lett., **71**:2791, 1997. 12, 24, 26

[41] K. Yamaguchi M. Murayama T. Kitamura T. Kuroda A. Tackeuchi, R. Ohtsubo and T. Takagahara. *Spin relaxation dynamics in highly uniform InAs quantum dots.* Appl. Phys. Lett., **84**:3576, 2004. 13

[42] Zetian Mi and Pallab Bhattacharya. *Molecular-beam epitaxial growth and characteristics of highly uniform InAs/GaAs quantum dot layers.* J. Appl. Phys., **98**:023510, 2005. 13

[43] Huffaker D. L. Zou Z. Park G. Shchekin O. B. Deppe, D. G. *Spontaneous emission and threshold characteristics of 1.3µm InGaAs-GaAs quantum-dot GaAs-based lasers.* IEEE J. Quantum Electron., **35**:1238, 1999. 13

[44] R. Heitz A. Hoffmann C. Thomsen F. Heinrichsdorff A. R. Goi, H. Born and D. Bimberg. *Magnetoluminescence Study of Annealing Effects on the Electronic Structure of Self-organized InGaAs/GaAs Quantum Dots.* Jpn. J. Appl. Phys., **39**:3907, 200. 13

[45] H. Jiang and J. Singh. *Nonequilibrium distribution in quantum dots lasers and influence on laser spectral output.* J. Appl. Phys., **85**:7438, 1999. 13

[46] G. Park, O. B. Shchekin, S. Csutak, Jr. T. R. Nelson, C. Ell, H. M. Gibbs, G. Khitrova, A. Schülzgen, M. Kira, F. Jahnke, and S. W Koch. *Room-temperature continuous-wave operation of a single-layered 1.3 µm quantum dot laser.* Appl.Phys. Lett, **75**:3267, 1999. 14

[47] Sean C. Woodworth, Daniel T. Cassidy, and Michael J. Hamp. *Sensitive Absorption Spectroscopy by Use of an Asymmetric Multiple-Quantum-Well Diode Laser in an External Cavity.* Appl. Opt., **40**(36):6719–6724, 2001. 15

[48] N. Kuramoto and K. Fujii. *Volume determination of a silicon sphere using an improved interferometer with optical frequency tuning.* IEEE Trans. Instrum. Meas, **54**(36):868–871, 2002. 15

[49] S. R. Chinn, E. A. Swanson, and J. G. Fujimoto. *Optical coherence tomography using a frequency-tunable optical source.* Opt. Lett., **22**:340–342, 1997. 15

[50] H. Lim, J. F. de Boer, B. H. Park, E. C. Lee, R. Yelin, and S. H. Yun. *Optical frequency domain imaging with a rapidly swept laser in the 815-870 nm range.* Opt. Express, **14**(13):5937–5944, 2006. 15

[51] Mitsuru Sugawara Kohki Mukai, Nobuyuki Ohtsuka and Susumu Yamazaki. *Self-Formed $In_{0.5}Ga_{0.5}As$ Quantum Dots on GaAs Substrates Emitting at 1.3 μm.* Jpn. J. Appl. Phys., **33**:L1710–L1712, 1999. 16

[52] J.A. Lott, N.N. Ledentsov, V.M. Ustinov, N.A. Maleev, A.E. Zhukov, A.R. Kovsh, M.V. Maximov, B.V. Volovik, Zh.I. Alferov, and D. Bimberg. *InAs-InGaAs quantum dot VCSELs on GaAs substrates emitting at 1.3 μm.* Electronics Letters, **36**(16):1384 –1385, 3 2000. 17

[53] G.T. Liu T.C. Newell A. Stintz B. Fuchs K.J. Malloy P.M. Varangis, H. Li and L.F. Lester. *Low-threshold quantum dot lasers with 201nm tuning range.* Electron. Lett. , **36**:1544, 2000. 17, 28

[54] G. Bhm L. Chu, A. Zrenner and G. Abstreiter. *Normal-incident intersubband photocurrent spectroscopy on InAs/GaAs quantum dots.* Appl. Phys. Lett., **75**:3599, 1999. 17

[55] Zhiliang Yuan, Beata E. Kardynal, R. Mark Stevenson, Andrew J. Shields, Charlene J. Lobo, Ken Cooper, Neil S. Beattie, David A. Ritchie, and Michael Pepper. *Electrically Driven Single-Photon Source.* Science, **295**:5552, 2001. 17

[56] Ekert A. Bouwmeester, D. and A. Zeilinger. *The Physics of Quantum Information*, volume 9. Springer, Berlin, Heidelberg, New York, 1984. 98 DM. 17

[57] William A. Tisdale, Kenrick J. Williams, Brooke A. Timp, David J. Norris, Eray S. Aydil, and X.-Y. Zhu. *Hot-Electron Transfer from Semiconductor Nanocrystals.* Science, **328**(5985):1543–1547, 2010. 18

[58] A. Tierno and T. Ackemann. *Tunable, narrow-band light source in the 1.25 μm region based on broad-area quantum dot lasers with feedback.* Appl. Phys. B, **89**:585–588, 2007. 18, 39, 151

[59] Alduraibi, M., M Missous, P. Luke Sam, A. Tierno, S. Keatings, and T. Ackemann. *Optical and electrical properties of stacked binary InAs-GaAs quantum dot structures prepared under Surfactant-mediated growth conditions.* Journal of Phys.: Conf. series , accepted for pubblication, 2010. 18, 152

[60] A. Tierno and T. Ackemann. *Opto-thermal pulsations via changes in waveguiding in a quantum dot lasers diode.* Appl. Phys. Lett., in submission, 2010. 18, 19, 152

[61] A. Tierno, N. Radwell, and T. Ackemann. *Bistability, opto-thermal pulsations and time-resolved spectra of a quantum dot lasers diode.* IEEE Journal of Quantum Electronics, in submission, 2010. 18, 152

[62] A. Tierno, N. Radwell, and T. Ackemann. *Time-resolved spectra of a self-pulsing quantum dot laser.* Proc. of SPIE, **7720**(0277-786X):77202H–1, 2010. 18, 152

[63] S. Barland, O. Piro, M. Giudici, J. R. Tredicce, and S. Balle. *Experimental evidence of van der Pol -Fitzhugh -Nagumo dynamics in semiconductor optical amplifiers.* Phys. Rev. E, **68**:036209, 2003. 18, 48, 58, 59, 72, 152

[64] A. Tierno, T. Ackemann, T. Maggipinto, and M. Brambilla. *Saturation and self-lensing in self-assembled quantum dots with constant-wave driving.* Phys. Rev. B, **80**(3):035314, 2009. 19, 87, 119, 152, 153

[65] A. Tierno and T. Ackemann. *Bistability and opto-thermal-pulsations in a quantum-dot edge-emitting laser diode.* Journal of Phys.: Conf. series , accepted for pubblication, 2010. 19, 152, 153

[66] D. Bimberg. *Quantum dots for lasers, amplifiers and computing.* J. Phys. D: Appl Phys., **38**:2055–2058, 2005. 20

[67] D. J. Mowbray and M. S. Skolnick. *New physics and devices based on self-assembled semiconductor quantum dots.* J. Phys. D: Appl Phys., **38**:2059–2076, 2005. 20

[68] S. S. Mikhrin A. P. Vasil'ev E. S. Semenova N. A. Maleev V. M. Usti-
nov M. M. Kulagina E. V. Nikitina I. P. Soshnikov Yu. M. Shernyakov
D. A. Livshits N. V. Kryjapovskykaya D. S. Sizov M. V. Maximov A. F.
Tsatsul'nikov N. N. Ledentsov Bimberg D. A. E. Zhukov, A. R. Kovsh and
Zh. I. Alferov. *High external differential efficiency and high optical gain of
long–wavelength quantum dot laser.* Physica E, **17**:562–592, 2003. 20, 28,
85, 87

[69] T. J. Badcock D. J. Mowbray M. S. Skolnick K. M. Groom M. Gutiérrez
M. Hopkinson J. S. Ng J. P. R. David H. Y. Liu, I. R. Sellers and R. Bean-
land. *Improved performance of 1.3 µm multilayer InAs quantum-dot lasers
using a high-growth-temperature GaAs spacer layer.* Appl. Phys. Lett. ,
85:704–706, 2004. 20

[70] T. J. Badcock K. M. Groom I. R. Sellers M. Hopkinson R. A. Hogg D. J.
Robbins D. J. Mowbray H. Y. Liu, D. T. Childs and M. S. Skolnick. *High-
Performance Three-Layer 1.3-µm InAsGaAs Quantum-Dot Lasers With
Very Low Continuous-Wave Room-Temperature Threshold Currents.* IEEE
Photon. Tech. Lett., **17**:1139–1141, 2005. 20, 28

[71] A.R. Adams P.J.A. Thijs A.F. Phillips, S.J. Sweeney. *Theoretical and ex-
perimental analysis of InAs/InP quantum dash lasers.* IEEE Jour. Sel. Top.
Quantum Electron, **5**:401, 1999. 21

[72] O. B. Shchekin, D. G. Deppe, and D. Lu. *Spontaneous emission and thresh-
old characteristics of 1.3 µm InGaAs-GaAs quantum-dot GaAs-based lasers.*
Appl. Phys. Lett, **78**:3115, 2001. 21

[73] M. V. Maksimov Yu. M. Shernyakov E. S. Semenova A. P. Vasilev A. E.
Zhukov V. M. Ustinov I. I. Novikov, N. Yu. Gordeev and G. G. Zegrya.
*Temperature dependence of the effective coefficient of Auger recombination
in 1.3 µm InAs/GaAs QD lasers.* Semiconductors, **39**:477, 2005. 21

[74] I.P. Marko, A.R. Adams, S.J. Sweeney, D.J. Mowbray, M.S. Skolnick, H.Y.
Liu, and K.M. Groom. *Recombination and loss mechanisms in low-threshold*

InAs-GaAs 1.3 µm quantum-dot lasers. IEEE Jour. of Sel. Topics in Quantum Electronics , **11**(5):1041–1047, 2005. 21

[75] O. B. Shchekin and D. G. Deppe. *Low-Threshold High-To 1.3 µm In-As Quantum-Dot Lasers Due to P-type Modulation Doping of the Active Region.* IEEE photonics technology letters, **14**:1231, 2002. 21

[76] N. F. Masse, I. P. Marko, A. R. Adams, and S.J. Sweeney. *Temperature insensitive quantum dot lasers: are we really there yet?* J. Mater. Sci: Mater Electr, **20**:S272:S276, 2009. 21

[77] D. A. Livshits S. Mikhrin J. Weimert A. Kovsh, I. Krestnikov and A. Zhukov. *Quantum dot laser with 75 nm broad spectrum of emission.* Opt. Lett. , **32**:793–7, 2007. 28

[78] B. Dagens F. Lelarge B. Rousseau F. Poingt O. Legouezigou F. Pommereau A. Accard P. Gallion J. Renaudier, R. Brenot and G.-H. Duan. *45 GHz self-pulsation with narrow linewidth in quantum dot Fabry-Perot semiconductor lasers at 1.5 µm.* Electron. Lett., **41**:1007–1008, 2005. 28

[79] M. Lämmlin D. Bimberg M. G. Thompson K. T. Tan C. Marinelli R. V. Penty I. H. White V. M. Ustinov A. E. Zhukov Yu. M. Shernyakov A.F. Ioffe M. Kuntz, G. Fiol and A. R. Kovsh. *35 GHz mode-locking of 1.3 µm quantum dot lasers.* Appl. Phys. Lett., **85**:843–845, 2004. 28

[80] J.-M. Hopkins, S.A. Smith, C.W. Jeon, H.D. Sun, S. Calvez D. Burns, M.D. Dawson, T. Jouhti, and M. Pessa. *0.6 W CW GaInNAs vertical external-cavity surface emitting laser operating at 1.32 µm.* Electron. Lett., **40**:30–31, 2004. 28

[81] Masahiko Kondow, Takeshi Kitatani, Shinichi Nakatsuka, Michael C. Larson, Kouji Nakahara, Yoshiaki Yazawa, Makoto Okai, and Kazuhisa Uomi. *GaInNAs: A Novel Material for Long-Wavelength Semiconductor Lasers.* IEEE J. Sel. Top. Quantum Electron., **3**:719–730, 1997. 28

[82] A. Biebersdorf, C. Lingk, De Giorgi M., J. Feldmann, J. Sacher, M. Arzberger, C. Ulbrich, G. Bohm, M.-C. Amann, and G. Abstreiter. *Tunable single and dual mode operation of an external cavity quantum-dot injection laser.* J. Phys. D: Appl Phys., **36**:1–3, 2003. 28

[83] C. N. Allen, G. Ortner, C. Dion, P. J. Poole, P. Barrios, J. Lapointe, G. Pakulski, W. Render, S. Fafard, and S. Raymonde. *External-cavity quantum-dot laser tunable through 1.55 μm.* Appl. Phys. Lett., **88**:113109, 2006. 28

[84] G. Ortner, C. N. Allen, C. Dion, P. Barrios, D. Poitras, D. Dalacu, G. Pakulski, J. Lapointe, P. J. Poole, W. Render, and S. Raymonde. *External cavity InAs/InP quantum dot laser with a tuning range of 166 nm.* Appl. Phys. Lett., **88**:121119, 2006. 28

[85] A. Stintz G. T. Liu T. C. Newell K. J. Malloy P. Eliseev, H. Li and L. F. Lester. *Tunable Grating-Coupled Laser Oscillation and Spectral Hole Burning in an InAs Quantum-Dot Laser Diode.* IEEE J. Quantum Electron. , **36**:479–485, 2000. 28

[86] R. Wang T. C. Newell A. L. Gray H. Su, L. Zhang and L. F. Lester. *Linewidth Study of InAsInGaAs Quantum Dot Distributed Feedback Lasers.* IEEE Photon. Tech. Lett., **16**:2206–2208, 2004. 28

[87] R. Wang T. C. Newell A. L. Gray H. Su, L. Zhang and L. F. Lester. *Dynamic properties of quantum dot distributed feedback lasers: high speed, linewidth and chirp.* J. Phys. D: Appl Phys., **16**:2112–2118, 2005. 28

[88] I. Nelson B. Chann and T. G. Walker. *Frequency-narrowed external-cavity diode-laser-array bar.* Opt. Lett., **25**, 2000. 28, 29

[89] V. Raab, D. Skoczowsky, and R. Menzel. Tuning high-power laser diodes with as much as 0.38 W of power and $M^2 = 1.2$ over a range of 32 nm with 3-GHz bandwidth. *Opt. Lett.*, 27:1995–1997, 2002. 28, 29

[90] I. Fischer S. K. Mandre and W. Elsässer. *Control of the spatiotemporal emission of a broad-area semiconductor laser by spatially filtered feedback.* Opt. Lett. , **28**:1135–1137, 2003. 28

[91] C. J. Hawthorn, K. P. Weber G., and R. E. Scholtena. *Littrow configuration tunable external cavity diode laser with fixed direction output beam.* Rev. Sci. Instrum., **12**:4477, 2001. 28

[92] M. G. Littman and H. J. Metcalf. *Spectrally narrow pulsed dye laser without beam expander.* Appl. Opt., **17**:2224–2227, 1978. 29

[93] K. C. Harvey and C. J. Myatt. *External-cavity diode laser usimg a grazing-incidence diffraction grating.* Opt. Lett., **16**:910–912, 1991. 29

[94] D. Wandt, Tunnermann A Laschek, A., and H. Welling. *Continuously tunable external-cavity diode laser with a double-grating arrangement.* Opt. Lett., **22**:390–392, 1997. 29

[95] D. Wandt and Przyklenk Tunnermann A H. Welling. Laschek, A. *External cavity laser diode with 40 nm continuous tuning range around 825 nm.* Opt. Lett., **130**:81–84, 1996. 29

[96] A.Yu. Nevsky, U. Bressel, I. Ernsting, Ch. Eisele, M. Okhapkin, S. Schiller, A. Gubenko, D. Livshits, S. Mikhrin, I. Krestnikov, and A. Kovsh. *A narrow-line-width external cavity quantum dot laser for high-resolution spectroscopy in the near-infrared and yellow spectral ranges.* Appl. Phys. B, **92**:501, 2008. 35, 40

[97] A.E. Zhukov, A.R. Kovsh, V.M. Ustinov, N.N. Ledentsov A.Yu. Egorov, A.F. Tsatsulnikov, M.V. Maksimov, S.V. Zaitsev, Yu.M. Shernyakov, A.V. Lunev, and D. Bimberg P.S. Kopev, Zh.I. Alferov. *Photo- and electroluminescence in the 1.3-µmm wavelength range from quantum-dot structures grown on GaAs substrates .* Semiconductors, **33**:153, 1999. 35

[98] Ian S Osborne. *Applied Physics: Revealing the Invisible.* Science, **297**(5584):1097, 2002. 40

[99] Colin Baker, I. Gregory, M. Evans, W. Tribe, E. Linfield, and M. Missous. *All-optoelectronic terahertz system using low-temperature-grown In-GaAs photomixers.* Opt. Express, **13**(23):9639–9644, 2005. 41

[100] I. S. Gregory, W. R. Tribe, C. Baker, B. E. Cole, M. J. Evans, L. Spencer, M. Pepper, and M. Missous. *Continuous-wave terahertz system with a 60 dB dynamic range.* Applied Physics Letters, **86**(20), 2005. 41

[101] Shuji Matsuura, Masahiko Tani, and Kiyomi Sakai. *Generation of coherent terahertz radiation by photomixing in dipole photoconductive antennas.* Appl. Phys. Lett., **70**(5), 1997. 41

[102] K. A. McIntosh, E. R. Brown, K. B. Nichols, O. B. McMahon, W. F. DiNatale, and T. M. Lyszczarz. *Terahertz photomixing with diode lasers in low-temperature-grown GaAs.* Appl. Phys. Lett., **67**, 1995. 41

[103] Masahiko Tani, Kwang-Su Lee, and X.-C. Zhang. *Detection of terahertz radiation with low-temperature-grown GaAs-based photoconductive antenna using 1.55 μm probe.* App. Phys. Lett., **77**:1396–1399, 2000. 41

[104] Mitchell C. Chakraborty S. Missous M Alduraibi, M. *Interaction of low-temperature surfactant-grown InAs superlattice layers with arsenic precipitates.* Microelectronics Journal. , **40**:550–553, 2009. 41, 151

[105] T. Ackemann and S. Keating. *Characterization of LT-GaAs .* 2010. 45

[106] Haoling Liu, P. Smowton, H. Summers, G. Edwards, and W. Drexler. *Self-pulsing 1050 nm quantum dot edge emitting laser diodes.* Appl. Phys. Lett., **95**:101111, 2009. 47

[107] O. Qasaimeh, W.-D. Zhou, J. Phillips, S. Krishna, P. Bhattacharyaa, and M. Dutta. *Bistability and self-pulsation in quantum-dot lasers with intracavity quantum-dot saturable absorbers.* Appl.Phys. Lett., **74**:1654–1657, 1999. 47, 48, 59

[108] H. D. Summers, D. R. Matthews, P. M. Smowton, P. Rees, and M. Hopkinson. *Laser dynamics in self-pulsating quantum dot systems.* J. Appl. Phys., **95**:1036–1042, 2004. 47

[109] E. A. Viktorov, M. A. Cataluna, L. OFaolain, T. F. Krauss, W. Sibbett, E. U. Rafailov, and P. Mandela. *Dynamics of a two-state quantum dot laser with saturable absorber.* Appl. Phys. Lett., **90**:121113, 2007. 47

[110] A. G. Kuzmenkova, V. M. Ustinov, G. S. Sokolovskii, N. A. Maleev, S. A. Blokhin, A. G. Deryagin, S. V. Chumak, A. S. Shulenkov, S. S. Mikhrin, A. R. Kovsh, A. D. McRobbie, W. Sibbett, M. A. Cataluna, and E. U. Rafailov. *Self-sustained pulsation in the oxide-confined vertical-cavity surface-emitting lasers based on submonolayer InGaAs quantum dots.* Appl. Phys. Lett., **91**:121106, 2007. 47

[111] S. Mokkapati, H. H. Tan, C. Jagadish, and M. Buda. *Self-sustained output power pulsations in InGaAs quantum dot ridge-waveguide lasers.* Appl. Phys. Lett., **92**:021104, 2008. 47, 58, 59

[112] F. Marino, G. Catalán, P. Sánchez, S. Balle, and O. Piro. *Thermo-Optical Canard Orbits and Excitable Limit Cycles.* Phys. Rev. Lett., **92**:073901, 2004. 48, 58, 59

[113] Weiping Lu, Dejin Yu, and R. G. Harrison. *Excitibility in a nonlinear optical cavity.* Phys. Rev. A, **58**:R809–R811, 1998. 48

[114] Y. A. Rzhanov, H. Richardson, A. A. Hagberg, and J. V. Moloney. *Spatiotemporal oscillations in a semiconductor etalon.* Phys. Rev. A, **47**:1480–1491, 1993. 48

[115] P. Suret, D. Derozier, M. Lefranc, J. Zemmouri, and S. Bielawski. *Self-pulsing instabilities in an optical parametric oscillator: Experimental observation and modeling of the mechanism.* Phys. Rev. A, **61**:021805(R), 2000. 48

[116] M. Wegener and C. Klingshirn. *Self-oscillations of an induced absorber (CdS) in a hybrid ring resonator.* Phys. Rev. A, **35**:1740–1752, 1987. 48

[117] R. FitzHugh. *Impulses and physiological states in theoretical models of nerve membrane.* Biophys. J., **1**:445–466, 1961. 48

[118] J. S. Nagumo, S. Arimoto, and S. Yoshizawa. *An active pulse transmission line simulating nerve axon.* Proc. IRE, **50**:2061–2070, 1962. 48

[119] T. Ackemann, S. Barland, S. Balle, and J. R. Tredicce, 1999. Unpublished. 59

[120] Huang X., A. H. Li Stintz, and A. G. T. Liu L. F. Lester J. Cheng and Rice. *Bistable Operation of a Two-Section 1.3µm InAs Quantum Dot Laser-absorption Saturation and the Quantum Confined Stark Effect.* IEEE J. Quantum Electron., **37**:414, 2001. 59

[121] Richard P. Mirin Senior Member IEEE Mingming Feng, Steven T. Cundiff and Kevin L. Silverman. *Wavelength Bistability and Switching in Two-Section Quantum-Dot Diode Lasers.* IEEE J. of Quantum Electronics, **46**:951–958, 2010. 59, 143

[122] H. Kawaguchi. *Bistable laser diodes and their application: State of the art.* IEEE J. Select. Topics Quantum Electronics, **3**:1254–1270, 1997. 59

[123] M. Giudici, L. Giuggioli, C. Green, and J. R. Tredicce. *Dynamical behavior of semiconductor lasers with frequency selective optical feedback.* Chaos, Solitons & Fractals, **10**:811–818, 1999. 59

[124] A. Naumenko, N. A. Loiko, M. Sondermann, K. F. Jentsch, and T. Ackemann. *Abrupt turn-on and hysteresis in a VCSEL with frequency-selective optical feedback.* Opt. Commun., **259**:823–833, 2006. 59

[125] G. Huyet, S. Balle, M. Giudici, C. Green, G. Giacomelli, and J. R. Tredicce. *Low frequency fluctuations and multimode operation of a semiconductor laser with optical feedback.* Opt. Commun., **149**:341–347, 1998. 62

[126] S. Barland, J. R. Tredicce, M. Brambilla, L. A. Lugiato, S. Balle, M. Giudici, T. Maggipinto, L. Spinelli, G. Tissoni, T. Knödel, M. Miller, and R. Jäger. *Cavity solitons as pixels in semiconductors.* Nature, **419**:699–702, 2002. 63, 96

[127] M. Ahmed and M. Yamada. *Influence of Instantaneous Mode Competition on the Dynamics of Semiconductor Lasers.* IEEE J. Quantum Electron., **38**(6):682–693, 2002. 65

[128] L. Furfaro, F. Pedaci, M. Giudici, X. Hachair, J. Tredicce, and S. Balle. *Mode-switching in semiconductor lasers.* IEEE J. Quantum Electron., **40**:1365, 2004. 65

[129] A. M. Yacomotti, L. Furfaro, X. Hachair, F. Pedaci, M. Giudici, J. R. Tredicce, J. Javaloyes, S. Balle, E. A. Viktorov, and P. Mandel. *Dynamics of multimode semiconductor lasers.* Phys. Rev. A, **69**:053816, 2004. 65

[130] Minoru Yamada, Wataru Ishimori, Hironobu Sakaguchi, and Moustafa Ahmed. *Time-Dependent Measurement of the Mode-Competition Phenomena Among Longitudinal Modes in Long-Wavelength Lasers.* IEEE J. Quantum Electron., **39**:1548–1555, 2003. 65

[131] Y. Tanguy, J. Houlihan, G. Huyet, E. A. Viktorov, and P. Mandel. *Synchronization and Clustering in a Multimode Quantum Dot Laser.* Phys. Rev. Lett., **96**:053902, 2006. 65

[132] D. Bimberg and N. N. Ledentsov. *Quantum dots: lasers and amplifiers.* J. Phys.: Condens. Matter, **15**:R1063–R1076, 2003. 66, 74

[133] S. P. Hegarty, B. Corbett, J. G. McInerney, and G. Huyet. *Free-carrier effect on index change in 1.3 µm quantum-dot lasers.* Electron. Lett., **41**:416–418, 2005. 66, 74, 87

[134] Ch. Ribbat, R. L. Selin, I. Kaiander, F. Hopfer, N. N. Ledentsov, D. Bimberg, A. R. Kovsh, V. M. Ustinov, A. E. Zhukov, and M. V. Maximov. *Complete suppression of filamentation and superior beam quality in quantum-dot lasers.* Appl. Phys. Lett., **82**:952–954, 2003. 66, 75, 105

[135] P. M. Smowton, E. J. Pearce, H. C. Schneider, W. W. Chow, and M. Hopkinson. *Filamentation and linewidth enhancement factor in InGaAs quantum dot lasers.* Appl. Phys. Lett., **81**:3251–3253, 2002. 66, 75, 105

[136] H. C. Schneider, W. W. Chow, and S. W. Koch. *Anomalous carrier-induced dispersion in quantum-dot active media.* Phys. Rev. B, **66**:041310(R), 2006. 66

[137] John A. Buck. *Fundamental of optical fiber.* John Wiley and Sons, 1995. 66

[138] M. Brunstein, R. Braive, R. Hostein, A. Beveratos, I. Rober-Philip, I. Sagnes, T. J. Karle, A. M. Yacomotti, J. A. Levenson, V. Moreau, G. Tessier, and Y. De. *Thermo-optical dynamics in an optically pumped Photonic Crystal nano-cavity.* Opt. Exp., **17**, 2009. 73

[139] S. Adachi. Gaas, alas, and al(x)ga(1-x)as: Material parameters for use in research and device applications. *J. Appl. Phys.*, 58(3):R1–R29, 1985. 73

[140] T. Rössler, R. A. Indik, G. K. Harkness, and J. V. Moloney. *Modeling the interplay of thermal effects and transverse mode behavior in native-oxide confined vertical-cavity surface-emitting lasers.* Phys. Rev. A, **58**:3279–3292, 1998. 73

[141] M. Sheik-Bahae, A. A. Said, Tai-Huei Wei, D. J. Hagan, and E. W. Van Stryland. *Sensitive measurements of optical nonlinearities using a single beam.* IEEE J. Quantum Electron., **26**:760–769, 1990. 74, 93, 97

[142] T. Ackemann, T. Scholz, Ch. Vorgerd, J. Nalik, L. M. Hoffer, and G. L. Lippi. *Self-lensing in sodium vapor: Influence of saturation, atomic diffusion and radiation trapping.* Opt. Commun., **147**:411–428, 1998. 74, 93, 95, 97

[143] R. W. Boyd. *Nonlinear Optics.* Academic Press, Boston, 1992. 75, 106

[144] A. Yariv. *Quantum Electronics.* John Wiley & Sons, New York, 3rd edition, 1988. 75, 78, 91, 115, 126, 142

[145] A. E. Siegman. *Lasers.* University Science Books, Mill Valley, California, 1986. 78, 92, 106

[146] I. M. Perrini, S. Barbay, T. Maggipinto, M. Brambilla, and R. Kuszelewicz. *Model for optical pattern and cavity soliton formation in a microresonator with self-assembled semiconductor quantum dots.* Appl. Phys. B, **81**:905–912, 2005. 81, 83

[147] C. Meuer, K. Kim, M. Laemmlin, S. Liebich, A. Capua, G. Eisenstein, A. R. Kovsh, S. S. Mikhrin, I. L. Krestnikov, and D. Bimberg. *Static gain saturation in quantum dot semiconductor optical amplifiers.* Opt. Exp., **16**:8269–8279, 2008. 82, 85, 119, 153

[148] T. W. Berg, J. Mørk, and J. M. Hvam. *Gain dynamics and saturation in semiconductor quantum dot amplifiers.* New J. Phys., **6**:178, 2004. 82

[149] V. Cesari, W. Langbein, P. Borri, M. Rossetti, A. Fiore, S. Mikhrin, I. Krestnikov, and A. Kovsh. *Ultrafast gain dynamics in 1.3 μ m InAs/GaAs quantum-dot optical amplifiers: The effect of p doping.* Appl. Phys. Lett., **90**(20):201103, 2007. 82, 85, 87, 105, 119, 153

[150] Jin K. Kim, R. L. Naone, and L. A. Coldren. *Lateral Carrier Confinement in Miniature Lasers Using Quantum Dots.* IEEE J. Sel. Top. Quantum Electron., **6**:504–510, 2000. 83

[151] P. Borri, W. Langbein, J. Mørk, J. M. Hvam, F. Heinrichsdorff, M.-H. Mao, and D. Bimberg. Dephasing in inas/gaas quantum dots. *Phys. Rev. B*, 60:7784–7787, 2004. 83

[152] L. Spinelli, G. Tissoni, M. Brambilla, F. Prati, and L. A. Lugiato. *Spatial solitons in semiconductor microcavities.* Phys. Rev. A, **58**:2542–2559, 1998. 85

[153] W. T. Vetterling W. H. Press, S. A. Teukolsky and B. P. Flannery. *The Art of Scientific Computing.* Cambridge University Press, Cambridge, Second Edition. 87

[154] J.J. Olivero and R.L. Longbothum. *Empirical fits to the Voigt line width: A brief review.* Journal of Quantitative Spectroscopy and Radiative Transfer, **17**(2):233 – 236, 1977. 90

[155] J. H. Marburger. *Self-focusing: Theory.* Prog. Quant. Electr., **4**:35–110, 1975. 92

[156] Y. R. Shen. *Self-focusing: Experimental.* Prog. Quant. Electr., **4**:2–34, 1975. 92

[157] F. Salin, J. Squier, and M. Piché. *Mode locking of Ti:Al$_2$O$_3$ lasers and self-focusing: a gaussian approximation.* Opt. Lett., **16**:1674–1676, 1991. 92

[158] A. Le Floch, J. M. Lenormand, and R. Le Naour. *La Dynamique de états propes dans les résonateurs.* Rev. Cethedec, **32**:69, 1983. 92

[159] G. Labeyrie, T. Ackemann, B. Klappauf, M. Pesch, G. L. Lippi, and R. Kaiser. *Nonlinear beam shaping by a cloud of cold Rb atoms.* Eur. Phys. J. D, **22**:473–483, 2003. 93, 97

[160] Y. Tanguy, T. Ackemann, W. J. Firth, and R. Jäger. *Realization of a semiconductor-based cavity soliton laser.* Phys. Rev. Lett., **100**:013907, 2008. 96

[161] Takeru A., Takeyoshi S., and Kazuhiro K. *1.3 µm InAs Quantum-Dot Laser With High Dot Density and High Uniformity.* IEEE Photon. Tech. Lett., **18**:619–621, 2006. 99, 119, 153

[162] C. K. Chia, Y. W. Zhang, S. S. Wong, A. M. Yong, S. Y. Chow, S. J. Chua, and J. Guo. *Saturated dot density of InAs/GaAs self-assembled quantum dots grown at high growth rate.* Appl. Phys. Lett., **90**:161906, 2007. 99, 153

[163] B. Saleh and M. Teich. *Fundamentals of Photonics.* Wiley-Interscience, 1991. 100, 101

[164] Shunichi Muto Toshiro Futatsugi Yoshihiro Sugiyama, Yoshiaki Nakata and Naoki Yokoyama. *Characteristics of Spectral-Hole Burning of InAs Self-Assembled Quantum Dots.* IEEE J. Sel. Top. Quantum Electron., **4**:880–885, 1998. 100

[165] R. Heitz, T. Warming, F. Guffarth, C. Kapteyn, P. Brunkov, V. M. Usti-nov, and D. Bimberg. *Spectral hole burning in self-organized quantum dots.* Physica E, **21**(2-4):215–218, 2004. 100

[166] A. Capua, V. Mikhelashvili, G. Eisenstein, J. P. Reithmaier, A. Somers, A. Forchel, M. Calligaro, O. Parillaud, and M. Krakowski. *Direct obser-vation of the coherent spectral hole in the noise spectrum of a saturated InAs/InP quantum dash amplifier operating near 1550 nm.* Opt. Express, **16**(3):2141–2146, 2008. 101

[167] Martin J. Stevens R. P. Mirin Berry, J.J. and K. L. Silverman. *High-resolution spectral hole burning in InGaAs-GaAs quantum dots.* App.Phys.Lett., **88**:061114, 2006. 101

[168] V. Ya. Aleshkin, D. M. Gaponova, D. G. Revin, L. E. Vorobjev, S. N. Danilov, V. Yu. Panevin, N. K. Fedosov, D. A. Firsov, V. A. Shalygin, A. D. Andreev, A. E. Zhukov, N. N. Ledentsov, V. M. Ustinov, G. E. Cirlin, V. A. Egorov, F. Fossard, F. Julien, E. Towe, D. Pal, S. R. Schmidt, and A. Seilmeier. *Light absorption and emission in InAs/GaAs quantum dots and stepped quantum wells.* 10th Int. Symp. Nanostructures: Physics and Technology, **5**:QWSL.05p, 2002. 104

[169] M. Sugawara, N. Hatori, T. Akiyama, and H. Ishikawa. *Quantum dot semiconductor optical amplifiers for higth bit-rate signal processing over 40 Gbit/s.* Jpn. J. Appl.Phys., **5**:40, 2001. 104

[170] K. L. Silvermana, R. P. Mirin, S. T. Cundiff, and A. G. Norman. *Direct measurement of polarization resolved transition dipole moment in InGaAs-GaAs quantum dots.* Appl. Phys. Lett., **82**:4552, 2003. 105

[171] S. Sauvage, P. Boucaud, F. Glotin, R. Prazeres, J.-M. Ortega, A. Lematre, J.-M. Ge rard, and V. Thierry-Flieg. *Saturation of intraband absorption and electron relaxation time in n-doped InAs/GaAs self-assembled quantum dots.* Appl. Phys. Lett., **73**:3818, 1998. 105

[172] S. Schneider, P. Borri, W. Langbein, U. Woggon, J. Förstner, A. Knorr, R. L. Sellin, D. Ouyang, and D. Bimberg. *Self-induced transparency in InGaAs quantum-dot waveguides.* Appl. Phys. Lett., **83**(18):3668–3670, 2003. 105

[173] R. J. Lang, D. Mehuys, D. F. Welch, and L. Goldberg. *Spontaneous filamentation in broad-area diode laser amplifiers.* IEEE J. Quantum Electron., **30**:685–694, 1994. 105

[174] J. R. Marciante and G. P. Agrawal. *Spatio-temporal characteristics of filamentation in broad-area semiconductor lasers.* IEEE J. Quantum Electron., **33**:1174–1179, 1997. 105

[175] Ch. Ribbat, R. L. Sellin, I. Kaiander, F. Hopfer, N. N. Ledentsov, D. Bimberg, A. R. Kovsh, V. M. Ustinov, A. E. Zhukov, and M. V. Maximov. *Complete suppression of filamentation and superior beam quality in quantum-dot lasers.* Appl. Phys. Lett., 82(6):952–954, 2003. 105

[176] C. Sailliot, V. Voignier, and G. Huyet. *Filamentation in broad area quantum dot semiconductor lasers.* Optics Communications, **212**(4-6):353 – 357, 2002. 105

[177] E. Gehrig, O. Hess, C. Ribbat, R. L. Sellin, and D. Bimberg. *Dynamic filamentation and beam quality of quantum-dot lasers.* Appl. Phys. Lett., **84**(10):1650–1652, 2004. 105

[178] S. Colin, E. Contesse, P. Le Boudec, G. Stephan, and F. Sanchez. *Evidence of a saturable-absorption effect in heavily erbium-doped fibers.* Opt. Lett., **21**(24):1987–1989, 1996. 106

[179] M. Konstantaki, E. Koudoumas, S. Couris, Edmond Amouyal P. Lain, and, and Sydney Leach. *Substantial Non-linear Optical Response of New Polyads Based on Ru and Os Complexes of Modified Terpyridines.* J. Phys. Chem. B, **105**(12):2470–2479, 2001. 106

[180] N. K. M. Naga Srinivas, S. Venugopal Rao, and D. Narayana Rao. *Saturable and reverse saturable absorption of Rhodamine B in methanol and water.* J. Opt. Soc. Am. B, **20**(12):2470–2479, 2003. 106

[181] Michelle S. Malcuit, Robert W. Boyd, Lloyd W. Hillman, Jerzy Krasinski, and Jr. C. R. Stroud. *Saturation and inverse-saturation absorption line shapes in alexandrite.* J. Opt. Soc. Am. B, 1(1):73–75, 1984. 106

[182] Marek Samoc, Anna Samoc, Barry Luther-Davies, Helge Reisch, and Ullrich Scherf. *Saturable absorption in poly(indenofluorene): a picket-fence polymer.* Opt. Lett., 23(16):1295–1297, 1998. 107

[183] Jean-Francois Bisson, Dmitrii Kouznetsov, Ken-Ichi Ueda, Susanne T. Fredrich-Thornton, Klaus Petermann, and Guenter Huber. *Switching of emissivity and photoconductivity in highly doped Yb3+:Y2O3 and Lu2O3 ceramics.* Appl. Phys. Lett., 90(20):201901 –201901–3, may 2007. 107

[184] L. Dong, J. L. Archambault, L. Reekie, P. St. J. Russell, and D. N. Payne. *Photoinduced absorption change in germanosilicate preforms: evidence for the color-center model of photosensitivity.* Appl. Opt., 34(18):3436–3440, 1995. 107

[185] Joona Koponen, Mikko Soderlund, Hanna J. Hoffman, Dahv Kliner, and Jeffrey Koplow. *Photodarkening measurements in large mode area fibers.* volume 6453, page 64531E. SPIE, 2007. 107

[186] Thomas L. Paoli. *Saturable absorption effects in the self-pulsing (AlGa)As junction laser.* Appl. Phys. Lett., 34(10):652–655, 1979. 107

[187] J. S. Lawrence and D. M. Kane. *Nonlinear dynamics of a laser diode with optical feedback systems subject to modulation.* IEEE J. Quantum Electron., 38(2):185–192, 2002. 110

[188] F. Y. Lin and J. M. Liu. *Nonlinear dynamical characteristics of an optically injected semiconductor laser subject to optoelectronic feedback.* Opt. Commun., **221**:173, 2003. 110

[189] H. L. Stover and W. H. Steier. *Locking of laser oscillators by ligth injection.* Appl. Phys. Lett., 8:91, 1966. 110

[190] J. P. Toomey, D. M. Kane, S. Valling, , and A. M. Lindberg. *Automated correlation dimension analysis of optically injected solid state lasers.* Opt. Express, **17**:7592, 2009. 110

[191] P.G. Eliseev, H. Li, T. Liu, T.C. Newell, L.F. Lester, and K.J. Malloy. *Ground-state emission and gain in ultralow-threshold InAs-InGaAs quantum-dot lasers.* Selected Topics in Quantum Electronics, IEEE Journal of, 7(2):135 –142, 2001. 113

[192] K. C. Kim, K. Han, J. I. Lee, and T. G. K. *Gain-dependent linewidth enhancement factor in the quantum dot structures.* nanotechnology, **21**:134010, 2010. 113

[193] Z. Mi, S. Fathpour, and P. Bhattacharya. *Measurement of modal gain in 1.1μm p-doped tunnel injection InGaAs=GaAs quantum dot laser heterostructures.* Electr. Lett., 41:3374, 2005. 113, 119

[194] A. Salhi, L. Martiradonna, L. Fortunato, V. Tasco, G. Visimberga, R. Cingolani, A. Passaseo, and M. De Vittorio. *High-gain low-threshold InAs/InGaAs/GaAs quantum dot lasers emitting around 1300 nm.* Phys. Stat. Sol. (c), **3**:4027, 2006. 113, 119, 120, 153

[195] T. Ackemann. *Airy functions of Fabry-Perot resonators.* 2010. 116

[196] K. Kamath, J. Phillips, H. Jiang, J. Singh, and P. Bhattacharya. *Small-signal modulation and differential gain of single-mode self-organized $In_{0.4}Ga_{0.6}As/GaAs$ quantum dot lasers.* Appl. Phys. Lett., 70(22):2952–2953, 1997. 119, 153

[197] Jin-Long Xiao and Yong-Zhen Huang. *Numerical Analysis of Gain Saturation, Noise Figure, and Carrier Distribution for Quantum-Dot Semiconductor-Optical Amplifiers.* IEEE Journal of Quantum Electron, **44**:401, 2008. 119, 153

[198] B. W. Hakki and T. L. Paoli. *Gain spectra in GaAs doubleheterostructure injection lasers.* J. Appl. Phys., **46**:1299–1306, 1975. 119

[199] C.H. Henry, R.A. Logan, and F.R. Merritt. *Measurement of gain and absorption spectra in AlGaAs buried heterostructure lasers.* J. Appl. Phys., **51**:3042–3050, 1980. 119

[200] J. D. Thomson, H. D. Summers, P. J. Hulyer, P. M. Smowton, and P. Blood. *Determination of single-pass optical gain and internal loss us- ing a multi-section device.* Appl. Phys. Lett., **75**:2527–2529, 1999. 119

[201] J-M. Benoit, A. Lematre, G. Patriarche, K. Meunier, S. Barbay, and R. Kuszelewicz. *Report, including theory and experimental considerations on the operation of self-pulsing extended cavities in passive and active regimes.* Technical report, Laboratoire de Photonique et Nanostructures (LPN) - CNRS, 2006. 120

[202] A.A. Lagatsky, C.G. Leburn, C.T.A. Brown, W. Sibbett, S.A. Zolotovskaya, and E.U. Rafailov. *Ultrashort-pulse lasers passively mode locked by quantum-dot-based saturable absorbers.* Progress in Quantum Electronics, **34**(1):1–45, 2010. 136, 138

[203] Christopher G. Leburn. *Femtosecond Lasers for Data communications Applications.* Phd thesis, University of St. Andrews, 2007. 136, 138

[204] G. Minkin and I.Krestnikov. *test report for laser diode in TO-can package.* Technical report, 2004. Internal report. 138

[205] H. Nakamura, K. Kanamoto, Y. Nakamura, S. Ohkouchi, H. Ishikawa, and K. Asakawa. *Nonlinear optical phase shift in InAs quantum dots measured by a unique two-color pump/probe ellipsometric polarization analysis.* Journal of Applied Physics, **96**, 2004. 143, 150

[206] Pierre-Alain Probst and Alain Jaquier. *Multiple-channel digital lock-in amplifier with PPM resolution.* Review of Scientific Instruments, **65**(3):747–750, 1994. 143

[207] John H. Scofield. *Frequency-domain description of a lock-in amplifier.* American Journal of Physics, **62**(2):129–133, 1994. 143